

INFORMATION TO USERS

This reproduction was made from a copy of a document sent to us for microfilming. While the most advanced technology has been used to photograph and reproduce this document, the quality of the reproduction is heavily dependent upon the quality of the material submitted.

The following explanation of techniques is provided to help clarify markings or notations which may appear on this reproduction.

1. The sign or "target" for pages apparently lacking from the document photographed is "Missing Page(s)". If it was possible to obtain the missing page(s) or section, they are spliced into the film along with adjacent pages. This may have necessitated cutting through an image and duplicating adjacent pages to assure complete continuity.
2. When an image on the film is obliterated with a round black mark, it is an indication of either blurred copy because of movement during exposure, duplicate copy, or copyrighted materials that should not have been filmed. For blurred pages, a good image of the page can be found in the adjacent frame. If copyrighted materials were deleted, a target note will appear listing the pages in the adjacent frame.
3. When a map, drawing or chart, etc., is part of the material being photographed, a definite method of "sectioning" the material has been followed. It is customary to begin filming at the upper left hand corner of a large sheet and to continue from left to right in equal sections with small overlaps. If necessary, sectioning is continued again—beginning below the first row and continuing on until complete.
4. For illustrations that cannot be satisfactorily reproduced by xerographic means, photographic prints can be purchased at additional cost and inserted into your xerographic copy. These prints are available upon request from the Dissertations Customer Services Department.
5. Some pages in any document may have indistinct print. In all cases the best available copy has been filmed.

**University
Microfilms
International**
300 N. Zeeb Road
Ann Arbor, MI 48106

8505885

Yahya, Eddy

DENSITY OF GAP STATES IN HYDROGENATED AMORPHOUS SILICON

Iowa State University

Ph.D. 1984

**University
Microfilms
International** 300 N. Zeeb Road, Ann Arbor, MI 48106

**Density of gap states in hydrogenated
amorphous silicon**

by

Eddy Yahya

**A Dissertation Submitted to the
Graduate Faculty in Partial Fulfillment of the
Requirements for the Degree of
DOCTOR OF PHILOSOPHY**

**Department: Physics
Major: Solid State Physics**

Approved:

Signature was redacted for privacy.

~~In Charge of Major Work~~

Signature was redacted for privacy.

~~For the Major Department~~

Signature was redacted for privacy.

~~For the Graduate College~~

**Iowa State University
Ames, Iowa**

1984

TABLE OF CONTENTS

	Page
DEDICATION	xi
1. INTRODUCTION	1
2. SAMPLE PREPARATION	10
2.1. Deposition System	10
2.2. Sample Fabrication	14
3. EXPERIMENTAL PROCEDURE	23
3.1. Thickness Measurements	23
3.2. Optical Density Measurements	23
3.3. Infrared Measurements	28
3.4. Electrical Measurements	36
3.5. Schottky Diodes	40
3.6. Space Charge Limited Current Measurements	41
4. RESULTS AND DISCUSSION	48
4.1. Vibrational Spectra of a-Si:H	48
4.2. Optical Properties	56
4.3. Photoconductivity	68
4.4. Activation Energy	73
4.5. Schottky Diode	77
4.6. Space Charge Limited Current Measurements	84
5. SUMMARY AND CONCLUSION	99
6. REFERENCES	104
7. ACKNOWLEDGEMENTS	108
8. APPENDIX: CALCULATION OF THE DENSITY OF STATES FROM THE I-V CHARACTERISTICS OF SCHOTTKY DIODES	109

LIST OF FIGURES

	Page
Figure 1. Comparison of density of states distributions obtained from several methods, Field Effect (FE), Capacitance-Voltage (C-V), Space Charge Limited Current (B and DB), and Deep Level Transient Spectroscopy (DLTS). FE data from Madan and Le Comber [4], CV from Döhler and Hirose [17] B from Bhattacharya et al. [22], DB from den Boer [21], and DLTS results from Lang et al. [16]	9
Figure 2. Schematic diagram of the r.f. sputtering system	11
Figure 3. The Schottky diodes geometry layout. From the top to the bottom the layers are Au, a-Si:H, n ⁺ type a-Si:H, Mo, and the glass substrate (Corning 7059)	19
Figure 4. I-V characteristics of sample diodes (S88) at room temperature. — for Mo as a back contact --- for stainless steel as a back contact	21
Figure 5. Aluminium masking geometry with three individual aluminium patches separated by two gaps of 125 μm and 300 μm	22

Figure 6.	Optical system. Cary Model 14 spectrometer used in this laboratory	25
Figure 7.	Optical density versus wave length for samples (from left to right) S91, S83, S85, S87, and S107	26
Figure 8.	The schematic diagram of the optical system of the FTIR spectrometer for mid-IR	30
Figure 9.	Typical infrared transmission spectrum of a-Si:H represented by sample S58	31
Figure 10.	Typical infrared absorption spectrum of a-Si:H represented by sample S58	32
Figure 11.	Electric circuit used to measure I-V characteristics of the samples	37
Figure 12.	Energy band diagram of a Schottky diode. -.-.- the equilibrium Fermi level (E_{F0}) ----- the quasi-Fermi level (E_F)	42
Figure 13.	Ln V vs Ln J plot for sample S81. ○ is for the data — is the polynomial function degree 8	46

- Figure 14.** Schematic illustration of the vibration spectron of silicon-hydrogen bonds. From top to the bottom, stretching, bending, and wagging, and rocking models of Si:H, Si:H₂, and Si:H₃. SYM or ASYM indicate symmetric and asymmetric modes. The solid circles represent S_i atoms and the hollow circle represent H atoms (After Brodsky et al., [10]) 49
- Figure 15.** Infrared vibrational spectra of samples deposited with different atomic percentage of hydrogen content (indicated in the parentheses) 50
- Figure 16.** Schematic diagram of the clustered and distribution forms of Si:H bonds. The Si atoms are denoted by solid circles, and H atoms by hollow circles (after Shanks et al. [1]) 52
- Figure 17.** The Si:H stretching vibrations for a number of a-Si:H films. Indicated next to the samples spectra are the hydrogen content in the films 54

- Figure 18. The Si:H stretching modes for samples produced under negative bias conditions (deposition temperature = 275°C, r.f. power = 200 watts, and $P_{Ar} = 15$ mt). Indicated next to the sample number is the hydrogen content in the films (after Moustakas [35]) 55
- Figure 19. The absorption edge of an amorphous semiconductor which has three region the power laws (A), the exponential (B), and the weak absorption tail (C).
—●— for crystal Si 57
- Figure 20. Optical absorption coefficient versus photon energy for a number of a-Si:H films with different hydrogen content. Indicated with the arrows are the band gaps (E_g^{opt}) of the samples 58
- Figure 21. $\sqrt{h\nu\alpha}$ versus $h\nu$ for thick samples (from 2.50 to 3.30 μm). Linear portions of the plots shift to higher energy as the hydrogen content in the films increase 61
- Figure 22. $\sqrt{h\nu\alpha}$ versus $h\nu$ for samples with thickness from 0.58 to 1.95 μm . The optical band gap increases with increasing hydrogen content 62
- Figure 23. The dependence of the constant B on hydrogen concentration for a-Si:H films 64

- Figure 24.** Hydrogen concentration dependence of the minimum optical density. The minimum optical density is almost constant for hydrogen concentration greater than 10 at. % 66
- Figure 25.** The optical gap E_g^{opt} versus hydrogen content of a-Si:H samples
+ data from Matsuda et al. [39];
□ from this research;
o results from Zhao and Hunklinger [40] 67
- Figure 26.** Spectral dependence of photo-response in a-Si:H samples with different hydrogen content. The ordinate represents the number of electrons flowing around the circuit per photon entering the films. The 7.7% at. H sample had been annealed at 250°C for 1 hour 70
- Figure 27.** Photo current i_p generated by volume absorbed light as a function of light intensity for a-Si:H samples with different concentration of hydrogen.
x was annealed at 250°C for 1 hour 72
- Figure 28.** Temperature dependence of the conductivity for samples with hydrogen content vary from 7.8 at. % to 20.3 at. % 74

- Figure 29.** Variation of the conduction band edge (E_c), the Fermi level (E_f), and the valence band edge (E_v) with hydrogen concentration. The conduction band edge is used as a reference (Energy = 0). The position of the valence band edge relative to the conduction band edge is obtained from Figure 25 76
- Figure 30.** Current-voltage characteristics of Au/a-Si:H Schottky barriers with different hydrogen concentration
 ___ for forward bias
 --- for reverse bias 80
- Figure 31.** Schottky barrier height dependence on the hydrogen concentration 82
- Figure 32.** Auger depth profile of Au/a-Si:H Schottky diode with 0.75 keV Ar⁺ ion beam 83
- Figure 33.** Auger depth profile of Au/a-Si:H Schottky diode with 0.75 keV Ar⁺ ion beam. The diode has been in the open air for 3 months 85
- Figure 34.** Log J - log V characteristics for samples which were fabricated under nominally the same parameters 87
- Figure 35.** Density of states distribution for samples with hydrogen concentration 12.3 at. % 89

- Figure 36. The density of states distribution for sample S 58
 ___ for DOS with the calculated $\frac{d^3 \ln V}{d \ln J^3}$
 --- for DOS with $c_{\text{new}} = 2 \times \frac{d^3 \ln V}{d \ln J^3}$ 91
- Figure 37. Log J - log V characteristics for samples with hydrogen content vary from 5.6 at. % to 19.1 at. % 92
- Figure 38. Experimentally determined density of states for samples with hydrogen contents between 5.6 to 19.1 at. % obtained from SCLC 94
- Figure 39. Density of gap states as a function of hydrogen concentration. DOS drops exponentially for C_H less than 10 at. % 95
- Figure 40. Density of gap states as a function of optical band gap 98

LIST OF TABLES

	Page
Table 1. Deposition parameters for various a-Si:H films used in this research	18
Table 2. The empirically determined value of the prefactor A	35
Table 3. Properties of 2 series of samples shown in Figures 21 and 22	63

xi

DEDICATION

To Dian, with love.

1. INTRODUCTION

Amorphous silicon (a-Si) films have attracted much interest in the last decade. This is because the a-Si films are prototypical of all the tetrahedrally-coordinated amorphous semiconductors, and thus understanding their electronic properties could open up a whole family of new materials for future application. As a result of the demonstrated photovoltaic solar conversion capabilities when hydrogen is incorporated into the semiconductor (yielding hydrogenated amorphous silicon a-Si:H), it is a promising material for low-cost solar cells. Amorphous silicon has a high absorption coefficient in the visible solar spectrum which means that a thin film less than 2 μm is sufficient for an efficient solar cell, and hence, is a viable candidate to replace crystalline silicon (c-Si). Nominally, pure a-Si is permeated with dangling bonds within the bulk of the material, and these dangling bonds create localized states throughout the energy gap giving rise to conduction by hopping and acting as recombination centers, with the result that photoconductivity or photoluminescence becomes uninterestingly small and limits the electronic applications of the material. Incorporating hydrogen in the material, however, passivates the dangling bonds, thereby creating the interesting properties of the amorphous semiconductor. Approximately 10^{21}cm^{-3} hydrogen atoms are needed to eliminate enough gap states to display

significant photoconductivity [1,2] (which is an important sign of a good quality material for solar cells), despite the fact that electron spin resonance (ESR) only reveals approximately 10^{20} unpaired spins per cubic centimeter in pure a-Si. Thus the presence of a large number of broken bonds not detected by ESR are inferred. Brodsky and Kaplan [3] proposed that there are indeed 10^{21} dangling bonds per cubic centimeter in the material, however, a large proportion of these dangling bonds are able to pair across the microvoids in a spin-paired fashion, and eliminating the spin signal. Therefore, ESR is observed only for unpaired states or for large defects for which some of the dangling bonds are too distant to pair effectively. This proposal was supported by ESR data showing that a large number of spins could be created by photo-excitation [4].

Most of the research effort has been devoted to structures obtained by deposition of a-Si:H from glow discharge of silane (SiH_4) [5]. The r.f. sputtered material was believed to exhibit inferior electronic properties when compared to films produced by glow-discharge [6]. This belief arose from earlier less extensive examinations of the preparation of a-Si by sputtering which always yielded materials with a resistivity of a few hundred ohm-cm, a barely detectable photoconductive effect, and a poorly defined optical band gap in the vicinity of 1 eV [7]. However, studies in this laboratory have shown that r.f. sputtered a-Si:H films can be made to have photo-

electronic properties comparable to and gap states densities smaller than those of glow discharge material. This discovery was supported also by Moustakas and Friedman [8] and Pawlewicz who reported that the electrical and optical properties of sputtered a-Si films can be varied systematically over wide ranges, and that properties similar to those obtained by the glow-discharge process can be realized [7]. All of the poor photoelectronic properties of the sputtered material produced in the early work were attributed to a high density of localized states produced by dangling bonds. The improvement of the deposition conditions of sputtered material by adjustment of the deposition conditions of sputtered material, or of the deposition parameters such as partial pressures of argon and hydrogen gases, substrate-target spacing, and substrate temperature have changed these early findings. The deliberate incorporation of hydrogen into tetrahedrally coordinated amorphous semiconductors during their production by sputtering has been shown to lead to dramatic differences in properties from those of the unhydrogenated materials [9].

In 1977, Brodsky et al. [10] used infrared and Raman spectroscopy in an attempt to learn more about the nature of the bonding between the silicon and hydrogen atoms in a-Si:H. Several peaks in the IR absorption spectra were attributed to vibrational modes of the silicon-hydrogen bonds. According to them, the 2000 cm^{-1} peak was due to stretching modes for a single hydrogen atom bonded to an otherwise normally

coordinated silicon atom (SiH) while the 2085 cm^{-1} peak was absorption due to the symmetric and antisymmetric stretching modes of two hydrogen atoms bonded to a silicon atom (SiH_2) in the amorphous silicon network. Knights et al. [11], on the other hand, ascribed the 2085 peak to the stretching modes for SiH, and that the difference between the two peaks was supposedly because the monohydride configuration could exist in two essentially different environments (void-surfaces and bulk-site configurations). In 1980, Paul argued in [12] support of Knights' interpretation, even though he did not agree about the specific void-surface and the bulk-site configuration.

The work on a-Si has demonstrated the critical dependence of electronic properties on the density and distribution of localized states in the band gap. A measurement of the density of states, $N(E)$, defined as the number of states per unit volume per unit energy interval, is therefore of considerable importance [13]. The energy distribution of the density of states in high quality amorphous silicon hydride has been probed by various techniques. The minimum value of the DOS within the gap has been found to range from less than 10^{15} to $10^{17} \text{ cm}^{-3} \text{ eV}^{-1}$ when measured by different methods and there has been some controversy as to the relative accuracy of the different techniques. The situation is further complicated because of the fact that the quality of the material depends critically on the deposition conditions and unless one characterizes the same film using different techniques, it is

not possible to ascertain whether the scatter in the measured values of gap state densities arises from differing deposition conditions or is due to the uncertainty in the measuring methods.

Madan and Le Comber [14] in 1977 using the field-effect technique for the study of $N(E)$ in a-Si, reported that the DOS around the Fermi level for a series of glow discharge produced a-Si specimens was of the order of $10^{17} \text{ cm}^{-3} \text{ eV}^{-1}$ and the DOS distributions showed 2 peaks at 1.2 and 0.4 eV below the conduction band edge. These results are in a good agreement with the DOS distribution model suggested by Spear et al. [15]. The calculation of $N(E)$ from the experimental data rests on the basic assumption that the measurements are representative of a homogeneous bulk property of the material and are not dominated by interface states at the semiconductor surface [13]. This method has recently been challenged by the results of deep level transient spectroscopy (DLTS) on a-Si, a method which was introduced by Lang in 1974 for studying ZnO and O centers in GaP p-n junction. The results reported by Lang et al. [16] show a DOS around 0.6 eV below the bottom of the conduction band of the order of 10^{15} with a basically different distribution of states. The latter group argued that the differences are mainly due to the fact that the DLTS results are representative of the "true" volume density of states, whereas the field-effect measurements are affected by states in the surface region which are not present in the bulk of the

material; but doping the material for DLTS measurement create other density states in the band gap and shift the Fermi level.

Other alternatives for determining the DOS of a-Si are the Capacitance-Voltage (C-V) and Space Charge Limited Currents methods (SCLC). In 1977, the C-V method to determine the DOS of a-Si:H was introduced by Döhler and Hirose [17]. They found that the $N(E)$ was a flat $8 \times 10^{16} \text{ cm}^{-3} \text{ eV}$ from 0.80 to 0.55 eV below E_c . In 1980, Viktorovitch and D. Jousse [18] used low frequency C-V measurements to determine the DOS in a-Si:H with Schottky diode structure devices. They reported, (1) the density of states around midgap was about $10^{16} \text{ cm}^{-3} \text{ eV}^{-1}$ for sputtered a-Si:H (optical gap = 1.9 eV, $C_H = 15 \%$ at.), (2) a peak in the density of states emerged at 0.4 eV above midgap, which was attributed to weak Si-Si bonds, and (3) a large conduction band-tail extending 0.45 eV below the conduction band was due to Si-H anti-bonding states. This was not surprising for such a wide gap material. They added that in an appropriate range of frequency and temperature, C-V measurements are sensitive only to bulk gap states located near the edge of the depletion region of the Schottky diodes. However, according to Weisfield [19] the interface states can also affect the Schottky diode measurements. Using the same samples, he employs the C-V and SCLC methods to determine the DOS of a-Si:H Schottky diodes structure. The results reported showed that for samples with high densities of states ($\geq 10^{17}$

$\text{cm}^{-3} \text{eV}^{-1}$) the two techniques gave good agreement but a discrepancy started to appear for samples with DOS less than $10^{16} \text{cm}^{-3} \text{eV}^{-1}$. The C-V method showed saturation of the DOS at about $10^{16} \text{cm}^{-3} \text{eV}^{-1}$ for samples which have a wide variety of photo-electronic properties. It is speculated that surface states start to contribute to the results of C-V measurement. The SCLC showed state densities which dropped another order of magnitude for the best samples. The SCLC measurement was introduced for the first time by Rose [20] in 1955, in studying the electronic density of states continuously distributed in the gap of insulator thin film materials. In this experiment a voltage applied across a thin diode cause an electrode (the cathode) to inject a nonequilibrium density of electronic charge, which populates the empty gap states above the Fermi level in the vicinity of the cathode. When the applied voltage is large enough, this extra charge extends across the entire sample thickness, and the current collected by the counter electrode (the anode) becomes space-charge limited. Almost all the charge is trapped, but an exponentially small fraction is thermally promoted to the conduction band edge E_c , increasing the current measured. It is this bulk enhancement mechanism which is analyzed to provide information about the DOS above the equilibrium Fermi level [19].

Recently, den Boer [21], Mackenzie et al. [13], and Bhattacharya et al. [22] using SCLC, have studied the DOS of a-Si:H glow discharge samples with $n^+/i/n^+$ structures. Their

results for the state density distribution $N(E)$, and those determined by field effect which shows a peak at 0.4 eV below E_c [14], deep level transient spectroscopy (DLTS) which gives the density states of the order of $10^{15} \text{ cm}^{-3} \text{ eV}^{-1}$ at about 0.6 eV [16], and capacitance voltage measurement which shows flat structure of DOS [17] are compared in Figure 1.

The work reported in this thesis is concerned with producing high quality amorphous silicon hydride with r.f. sputter deposition. The system used in the sputtering and the sample fabrication are described in Chapter II, while Chapter III discusses the technique used for characterization of the samples. The SCLC method is employed in the determination of the states density distribution of the a-Si:H film using Au/a-Si:H Schottky diodes structure. Chapter IV presents a discussion of the results. All of these are summarized and concluded in Chapter V.

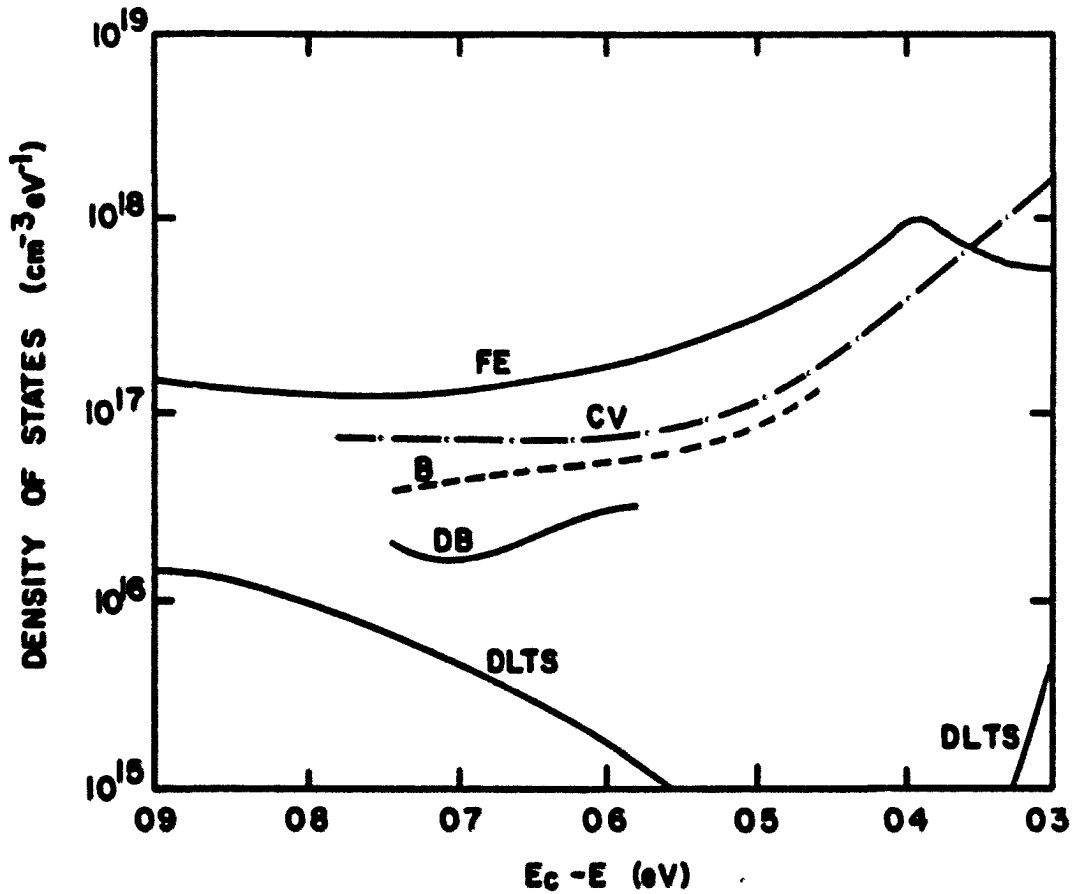


Figure 1. Comparison of density of states distributions obtained from several methods, Field Effect (FE), Capacitance-Voltage (C-V), Space Charge Limited Current (B and DB), and Deep Level Transient Spectroscopy (DLTS). FE data from Madan and Le Comber [14], CV from Döhler and Hirose [17], B from Bhattacharya et al. [22], DB from den Boer [21], and DLTS results from Lang et al. [16]

2. SAMPLE PREPARATION

2.1. Deposition System

All of the samples reported in this thesis were prepared by reactive r.f. diode sputtering. Briefly stated, this is a thin film deposition technique, in which material is ejected from a target by ion bombardment and deposited on a substrate to form a thin film. A variety of bombarding ions can be used, but the ions should not react chemically with the target or the growing film. Therefore argon, a noble gas, is used in this sputter deposition because it is also easily available and relatively inexpensive.

The basic principle of operation is as follows. An r.f. generator creates an electric field between the target and the substrate holder. This field accelerates electrons, produced primarily by Penning ionization process, which in turn collide with introduced gas atoms, and the ionization yields ions and more electrons, forming a plasma. The plasma consists of positive ions and electrons in a sea of neutral atoms [23]. Since the surface of the deposited film is in constant contact with the plasma, the structure and physical properties of the film depend on the nature of the plasma and its complex reactions with the growing layer [5].

A schematic diagram for the sputtering equipment and related apparatus used in this research are shown in Figure 2. The main features of the system are a matching network, three

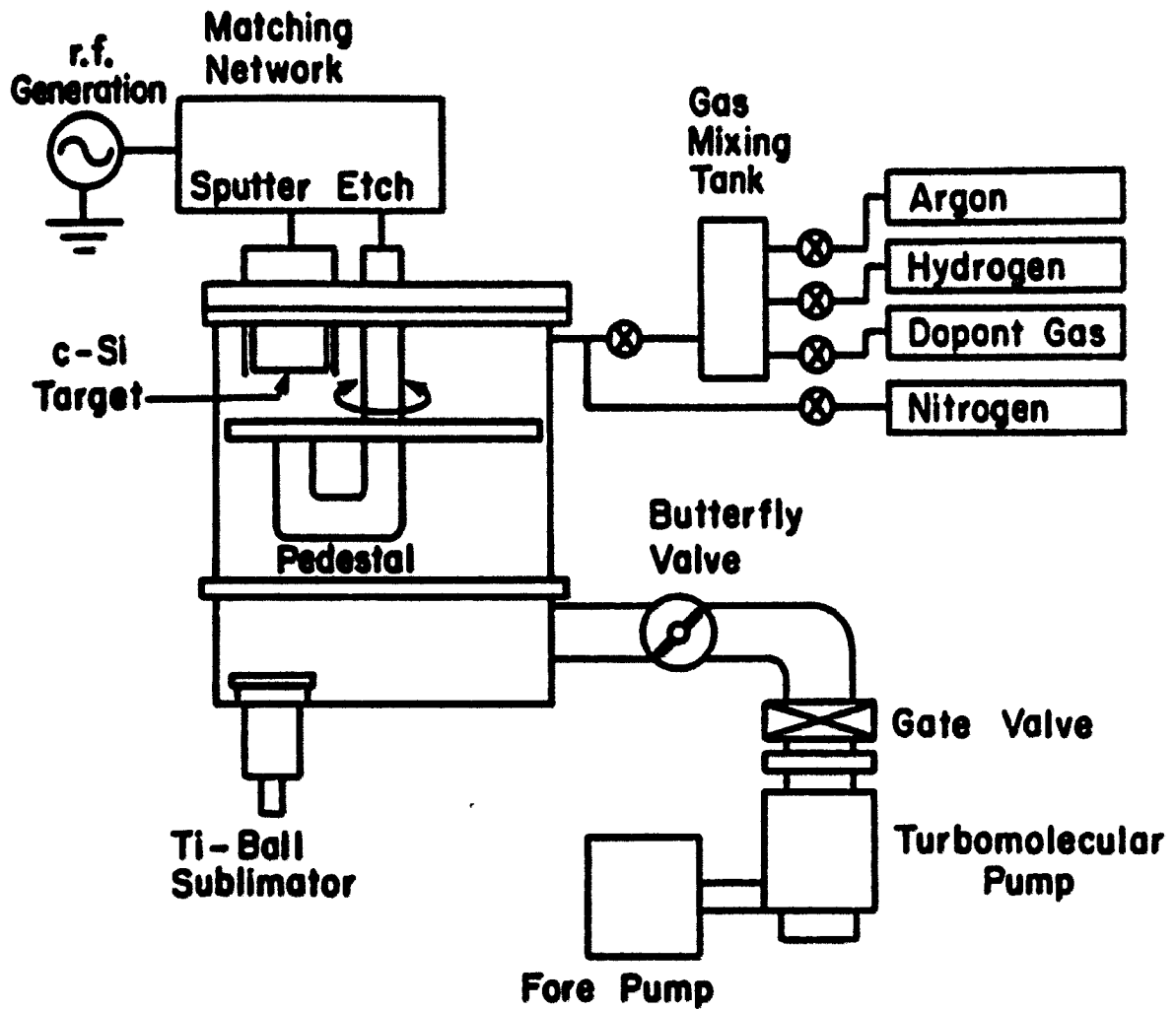


Figure 2. Schematic diagram of the r.f. sputtering system

fixed targets in the upper part of the chamber, and a movable J-shaped pedestal. The power supply and the matching network were built by Ion Equipment Corporation, while the base plate and the pumping systems were designed and assembled by Ames Lab personnel. An r.f. generator which can be connected independently to either of the three targets or to the pedestal operates at 13.56 MHz and supplies the power to the target during sputtering and to the pedestal during sputter etching. The targets and the pedestal are automatically grounded when the r.f. power is not applied to them. The generator is able to deliver power up to 600 watts, which creates a maximum d.c. bias voltage of 2 kV. The three targets are arranged in a circle with the same distance between each. The first target, a 15 cm stainless steel plate, is used as a mount for sputter etching or back sputtering the substrate. The second and the third targets are 15 cm cast polycrystalline silicon discs of 99.999% purity which were bonded to stainless steel plates, and these could be screwed into the target holders. All of the targets and the pedestal are water cooled. If the water cooling system fails during sputtering, a safety interlock turns the r.f. power off and prevents damage to the target from overheating. The pedestal, which acts as a substrate holder, can be moved in a vertical direction or rotated around its axis. The vertical movement allows variation of the distance between the target and the substrate, while the rotation around its axis makes it possible to sputter different materials in

succession without breaking the vacuum. In this research, the distance between the target and the substrate holder was fixed at 2.5 cm. The sputtering assembly is housed in a glass cylinder with Viton seals. The glass stands on a stainless steel belljar which is connected to a titanium sublimation source at the bottom and a Leybold-Heraeus turbomolecular pump (model TMP 450) at one side. The turbo-pump is backed by a Alcatel model #2063 forepump. The pumping speed can be manually throttled with a butterfly valve which is mounted immediately after the outlet of the sputtering chamber, and a gate valve which is situated above the inlet of the turbo-pump.

The chamber is routinely pumped down to a base pressure of about 3×10^{-7} torr before each sputtering run. The vacuum is achieved by baking with General Electric Infrared heat lamps during overnight pumpdown. Once the chamber pressure is in the range of 10^{-7} torr, the Ti-ball source is heated to evaporate a thin film of Ti on the walls. The Ti absorbs much of the rest of the active gases such as N_2 , O_2 , H_2 , CO, CO_2 , and water vapor, and brings the vacuum pressure to below 3×10^{-7} torr in about an hour. The pressure in the chamber is monitored with three different pressure gauges. The first is a Veeco RGLL-6 Ionization Gauge control with a Tech Supply type 342 ion gauge circuit which is mounted just after the butterfly valve, and works for pressures from 1×10^{-4} to 1×10^{-11} torr. The second is a Granville-Phillips type 224 Gauge Controller with a Schultz-Phillips ion gauge which is mounted in the chamber to

measure a pressure from 1×10^{-1} to 1×10^{-6} torr. This gauge is used to measure the partial or the total pressure of the gases used in the sputtering. The third is a Veeco TG-6 Thermocouple Gauge control with two vacuum gauge tubes (type DV-1M). One monitors the pressure in the chamber, and the other the foreline pressure between the turbo-pump and forepump.

Besides ultrahigh purity gases - 99.9995 % pure argon and 99.999 % pure hydrogen - which are used in the sputtering, high purity phosphine is also used as a doping element. The gases are combined in a small mixing tank before being introduced into the sputtering chamber. The flow rate and the partial pressure for each individual gas are controlled by a Nupro needle valve with a micrometer metering scale, while the flow rate in each gas line is monitored with a Hastin Mass Flow meter.

2.2. Sample Fabrication

Depending on the type of measurement to be done, several types of samples were made on different substrates. For Space Charge Limited Current (SCLC) measurements, a Schottky diode sample was fabricated as discussed below.

A molybdenum layer about 1000 Å thick was deposited on a borosilicate glass (Corning 7059) substrate (to be referred to in the rest of the text as a glass substrate) by evaporation using a thermionic e-gun Electron Beam Evaporation Source. The

evaporation was started when the vacuum of the evaporator had reached about 2×10^{-7} torr. The vacuum was achieved by pumping the chamber with a Leybold Heraeus turbo-pump (TMP 450) which was backed by a Welch model # 1397 forepump. The pressure during the evaporation was not higher than 4×10^{-6} torr and the deposition rate of the Mo was about 3 Å/second measured in situ with a quartz crystal thickness monitor. Thirty minutes after deposition, the sample was cool enough to be moved to the sputtering chamber. By pumping down overnight, the chamber would be ready for sputtering on the following day. Before the deposition of the n^+ layer (a heavily doped a-Si:H with P), the substrate was sputter etched with argon to clean oxide from the surface. To start sputtering, the r.f. generator was turned on, the argon pressure was increased in the mixing tank, the butterfly valve was then closed, and the gas was introduced into the chamber. This would raise the pressure enough to initiate a plasma. When the plasma appeared, the butterfly valve was opened immediately. The argon flow rate was 30 sccm (standard centimeter cubic per minute) and the gas pressure was 12 mtorr. The pumping speed was high to clear the impurities from the chamber. The r.f. generator delivered 300 watts transmitted power to the substrate holder, while reflected power was less than 2.5 watts. Usually, the sputter etching was done for 90 seconds, except when the substrate was an electropolish stainless steel. In this case, the stainless steel substrate was sputter etched

for 5 minutes. The sputter etching was terminated by closing the argon valve and turning off the r.f. generator. The substrate was kept under the stainless steel target which worked also as a shelter before the next sputtering. One-by-one, phosphine, hydrogen, and argon gases were introduced into the chamber, as their partial pressures and flow rates were adjusted. The pumping speed was reduced to about 12 sccm argon by adjusting the gate valve. Then, the total pressure was measured. After that, the plasma was started, and the r.f. generator was adjusted to 600 watts transmitted power with reflected power less than 2.5 watts. Once the plasma was stable, the pedestal was rotated to put the substrate under the Si target for deposition of the n^+ layer. It took 90 seconds for a 300 Å thick deposit before the sputtering was stopped. For the intrinsic a-Si:H layer deposition, the chamber was pumped down to a pressure less than 1×10^{-6} torr. Then, the third target (polycrystalline Si) was sputtered clean for about 2 minutes before putting the substrate underneath it. The presputtering was necessary to remove impurities from the target surface deposited when it was in the open air. During the deposition of the a-Si:H, the partial pressure of H_2 and Ar were controlled carefully by the leak valves and monitored by the flow meters. The r.f. power applied to the target was 600 watts while the reflected r.f. power was less than 2.5 watts. The substrate holder temperature was no more than 200° C, measured by a thermocouple immediately after the r.f. power was

turned off. The sputtering parameters used for deposition of the selected samples are listed in Table 1, with the growth rates of the films varying between 2.5 and 4 Å/second. After sputtering, the sample was allowed to cool down for 20 minutes before the chamber was opened. Then, the sample was covered by a mask and put immediately into the evaporator for gold plating. The masks used were 2 stainless steel plates with 2 different sized holes. One had 9 holes, each 1.6 mm in diameter, providing room for about 9 diodes on the substrate, and the other had holes 0.9 mm in diameter. The evaporator was pumped down by an oil diffusion pump with a liquid-nitrogen cold trap in front, backed with a Welch model #1387 forepump. The gold was evaporated by resistively heating a tungsten boat after the base pressure had achieved a typical pressure value of 2×10^{-6} torr. The filament and the gold were allowed to outgas before the shutter was removed to expose the sample to the evaporant. The thickness of the condensed gold was measured in situ by a quartz crystal thickness monitor and 60 Å thick gold was obtained in one minute evaporation. During the evaporation, the vacuum pressure was no more than 6×10^{-6} torr. Beside the sample, a plain glass was put in the evaporator for transmittance measurements of the gold layer. Thus, the structure of the Schottky diode was constructed of layers of metal (Au), a-Si:H, n^+ type a-Si:H (heavily doped with phosphorus), molybdenum, and the glass substrate, as shown in Figure 3. In addition to the glass substrate with Mo layer,

Table 1. Deposition parameters for various a-Si:H films used in this research.

Sample	Base pressure (x 10 ⁻³ torr)	Hydrogen partial pressure (x 10 ⁻³ torr)	Argon partial pressure (x 10 ⁻³ torr)	Total pressure (x 10 ⁻³ torr)	Deposition time (minutes)
S59	3.2	.23	12	14	54
S78	2.4	.30	11	13	106
S81	1.3	.33	9.8	11	143
S83	2.2	.42	10.5	12	152
S85	2.6	.10	12	12	127
S87	2.5	.06	11	11	131
S89	1.8	.16	9	9.8	140
S91	2.6	1.80	6	10.9	160

For n⁺ type layer of all samples is

Phosphine partial pressure (x 10 ⁻³ torr)	Hydrogen partial pressure (x 10 ⁻³ torr)	Argon partial pressure (x 10 ⁻³ torr)	Deposition time (minutes)
.9	.32	10	1.5

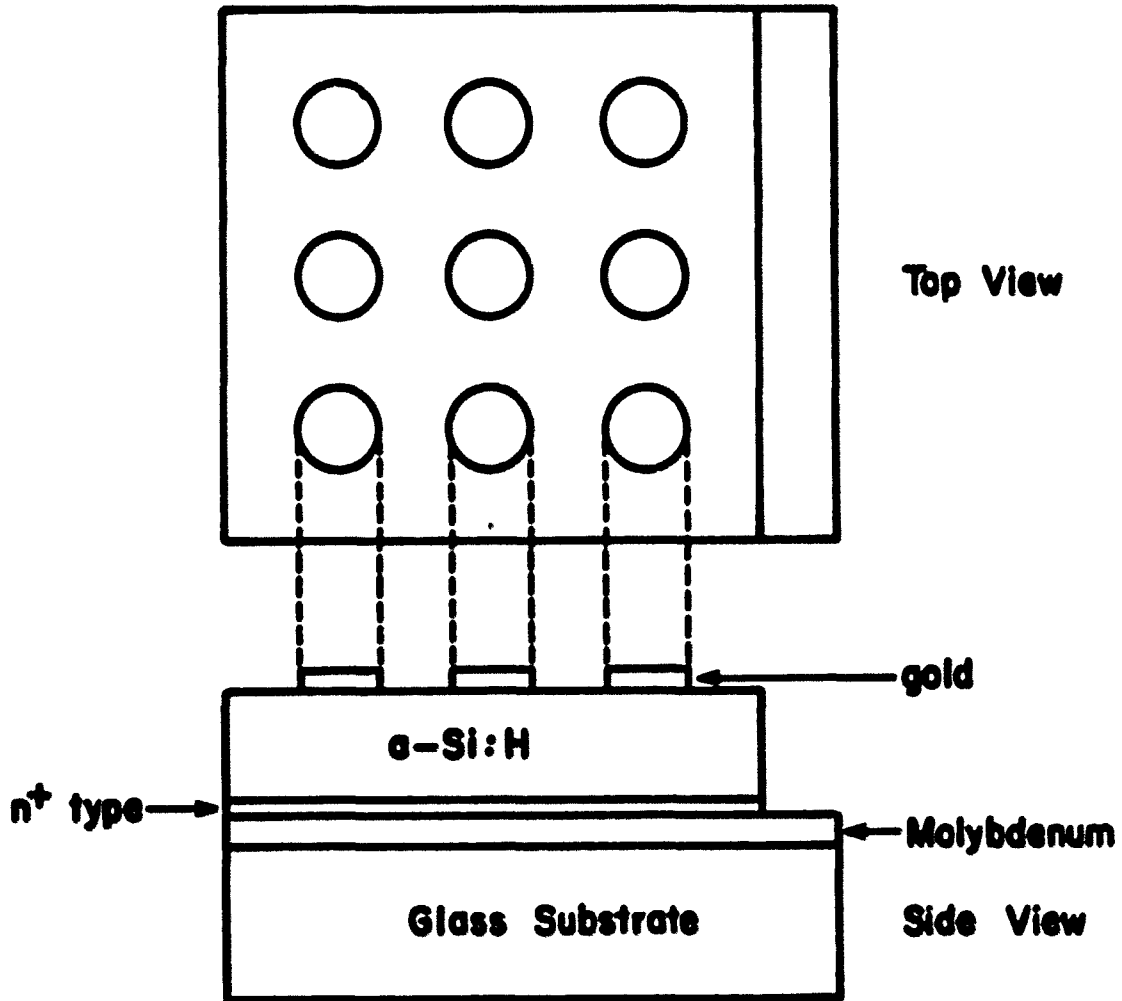


Figure 3. The Schottky diodes geometry layout.

From the top to the bottom the layers are Au, a-Si:H, n⁺ type a-Si:H, Mo, and the glass substrate (Corning 7059)

a stainless steel substrate was also tried for the Schottky diodes. From the I-V characteristics shown in Figure 4, a diode with a Molybdenum layer as a back contact displays a sharper breakdown point at the forward bias voltage and a much smaller current at the reverse bias voltage compared to its counterpart which has a stainless steel substrate as its back contact. This can be attributed to the better ohmic contact of Mo layer. The difference may be caused by roughness and the oxidation of the stainless steel surface. For the electrical measurements, the sample was coated with 250 Å aluminum contacts. Prior to the aluminum evaporation, the film was masked with two different width wires which created three individual aluminum patches separated by two gaps 125 μm and 300 μm wide as shown in Figure 5.

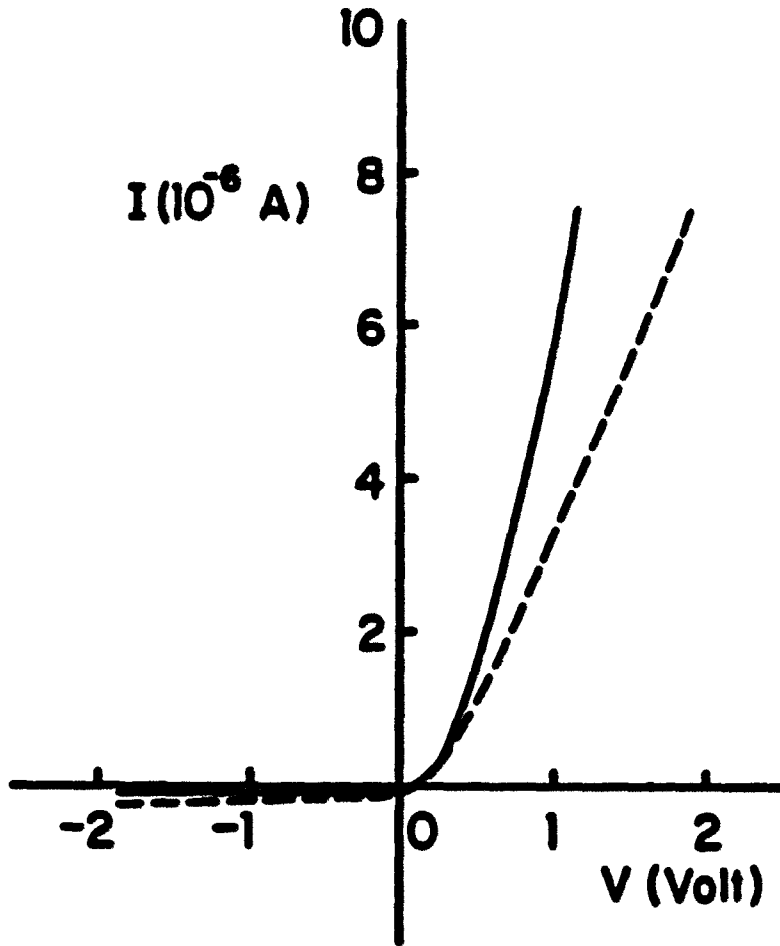


Figure 4. I-V characteristics of sample diodes (S88)
at room temperature

— for Mo as a back contact

--- for stainless steel as a back contact

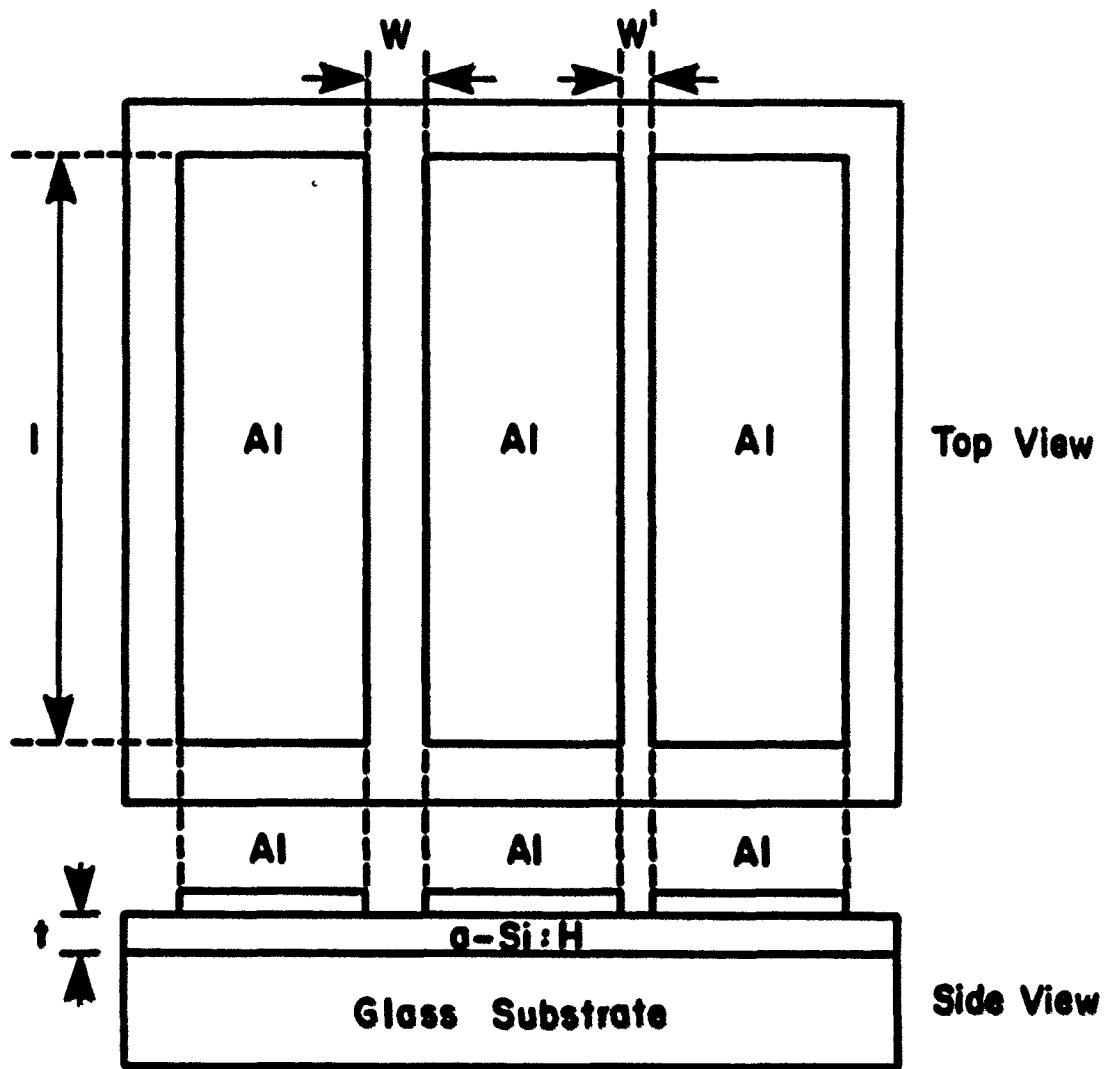


Figure 5. Aluminium masking geometry with three individual aluminium patches separated by two gaps of $125 \mu\text{m}$ and $300 \mu\text{m}$

3. EXPERIMENTAL PROCEDURE

3.1. Thickness Measurements

The film thickness were measured using a Sloan Dektak Surface Profile Measuring Instrument. Samples were prepared on a glass substrate which was partially masked during the deposition of the a-Si:H film. Each sample was placed on a stage which can be adjusted manually to level the surface of the sample. Above the stage, a sensing head containing a diamond stylus traces the sample surface when the stage is moved horizontally. At the edge of the sample substrate where the stylus crosses from the blank substrate onto the sample film, a "step" which corresponds to the thickness of the film is indicated on a strip chart recorder. The measurement error is approximately 3% for 2 μm thick film.

The film thickness can also be determined from infrared transmission data, using an IR spectrometer. This technique which exploits the dependence of the wavelength of the interference fringes on the thickness of the sample is discussed further in Section 3.3. The two methods agreed to within about $\pm 5\%$ for approximate film thickness of 2 μm . The average value from these two methods was taken as the thickness of the sample.

3.2. Optical Density Measurements

The schematic diagram of the optical system of a Cary model 14 dual beam spectrometer which was used to measure the

optical band gap of the samples is shown in Figure 6. By placing a blank glass substrate in the reference beam (Ref. in figure) and the sample (a glass substrate coated with a-Si:H film) in the sample beam (Sam. in figure), the spectrometer eliminates the effects of the sample substrate using a differential measuring technique. The output spectra versus the wavelength of the visible light for several samples are shown in Figure 7. Oscillations in the region of energy below the optical gap energy are due to interference fringes. These scans were taken from the near-IR region 10,000 Å to about 5000 Å, with the optical density ranging approximately between 0.15 and 2.00, respectively.

The absorption coefficient, α , defined as the relative rate of change in light intensity I ($h\nu$) along its propagation path x can be written as [24]

$$\alpha = \frac{1}{I(h\nu)} \frac{d[I(h\nu)]}{dx} \quad . \quad (1)$$

This parameter can be obtained from the data in the following way. Assuming that the light is at normal incidence and the transmittance is interference free, the transmission coefficient then can be represented as [10]

$$T = \frac{e^{-\alpha t} (1-R)^2}{1-R^2 e^{-2\alpha t}} \quad , \quad (2)$$

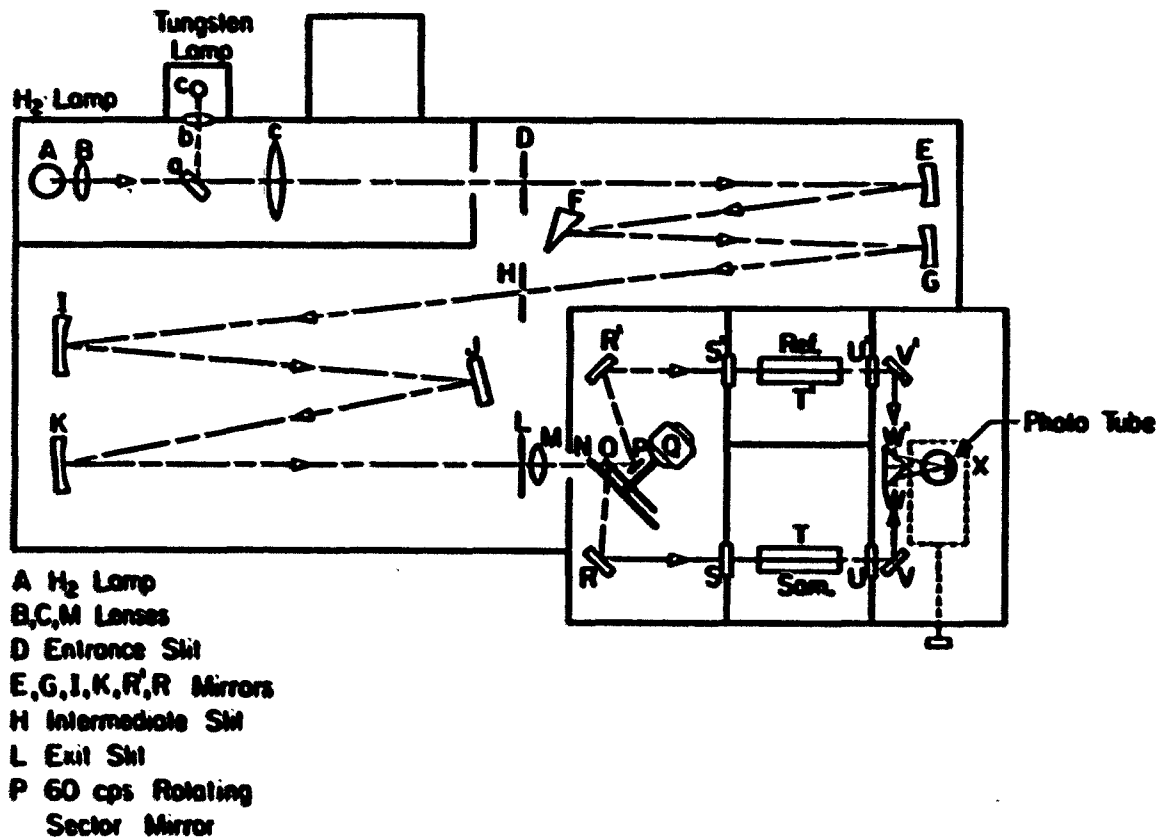


Figure 6. Optical system. Cary Model 14 spectrometer used in this laboratory

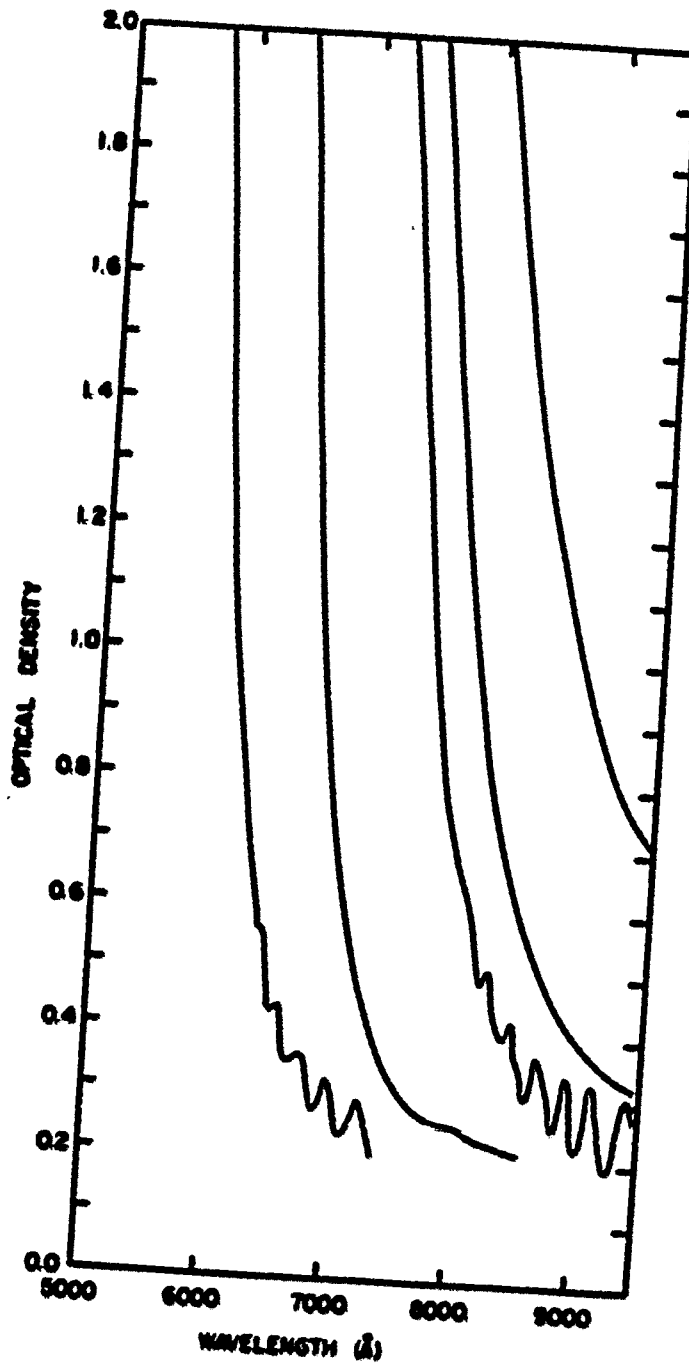


Figure 7. Optical density versus wave length for samples (from left to right) S91, S83, S85, S87, and S107

where t is the thickness of the film, and the reflectance R is given by [25];

$$R = \frac{(n_2 - n_1)^2 + n_2 k_2}{(n_2 + n_1)^2 + n_2 k_2} \quad (3)$$

where n and k are the real and imaginary parts of the index of refraction. The subscripts 1 and 2 refer to the media in front of and behind the interface, respectively. The initial medium is considered non-absorbing, so $k_1 = 0$. In the transparent range, as long as the optical density is less than 2, k_2 also is nearly zero. Equation (3) then reduces to

$$R = \frac{(n_2 - n_1)^2}{(n_2 + n_1)^2} \quad (4)$$

For $n_1 = 1$ (vacuum) and $n_2 \sim 3.7$ [26] (a-Si:H), Equation (2) yields the relationship between the optical absorption and transmission coefficient:

$$\alpha = -\frac{1}{t} \ln \left(\frac{-(1-R)^2 + \sqrt{(1-R)^4 + 4T^2 R^2}}{2TR^2} \right) \quad (5)$$

or

$$\alpha = -\frac{1}{t} \ln \left(\frac{-0.45 + \sqrt{0.20 + 0.44 T^2}}{0.22 T} \right) \quad (6)$$

The transmitted intensity, I , for the optical density, A , is given by Lambert's law,

$$I = I_0 e^{-\alpha t} \quad (7a)$$

and
$$A = \log_{10} \left(\frac{I_0}{I} \right) \quad (7b)$$

where I and I_0 are the incident and transmitted intensities of the photons. Hence, the transmission coefficient, T , can be written as

$$T = \frac{I}{I_0} = \log_{10}^{-1} (-A) \quad (8)$$

Thus, once the transmission coefficient is determined from the optical density, the absorption coefficient, α , can be calculated using Equation (6). In this formula, the small dependence of the real part of the index of refraction on the wavelength over the region of interest produces an error in of less than 5% [2].

3.3. Infrared Measurements

A single beam Fourier Transform Infrared (FTIR) spectrometer IBM Model IR98, with a silicon carbide rod (glow-bar) as a source of the mid-infrared ($6000-100 \text{ cm}^{-1}$) radiation, was used for all of the infrared measurements. The inter-ferometer unit contains two reference sources: (1) a white light (a small tungsten bulb lamp) whose interferogram centerburst (the region of maximum intensity) generates an electronic signal to mark time $\tau = 0$, and (2) a He-Ne laser whose interferogram, a unique cosine wave, electronically

generates discrete counting pulses. These pulses represented the smallest x-axis units available to the computer for sampling the data. The schematic diagram of the optical system of the FTIR spectrometer is shown in Figure 8. The Fourier-Transform Infrared (FTIR) spectroscopy technique allows all the frequencies of infrared energy to be measured simultaneously with the help of a Fourier transform operation to convert the interferograms into a spectrum. Two such interferograms, one for the sample and one for the reference, are recorded, transformed, and the ratio taken to produce the transmission or absorption spectrum [27].

The infrared measurements were made on films that were deposited on single crystal Si(c-Si) substrates. An uncoated matched c-Si substrate used as a reference and the sample were placed in the back channel (BK) of the spectrometer and scanned in succession. Then, the results were calculated by the computer using the reference to provide a basis for 100% transmission (or zero absorption). The infrared transmission and absorption were measured for each sample between the limits of 400 cm^{-1} and 4000 cm^{-1} . Typical results of the transmission and the absorption data as functions of the wavenumbers are shown in Figures 9 and 10 for sample S58.

The thickness of each sample was evaluated using the interference fringes of the transmission spectrum which result from internal reflections inside the film due to the difference in the index of refraction between the film and the

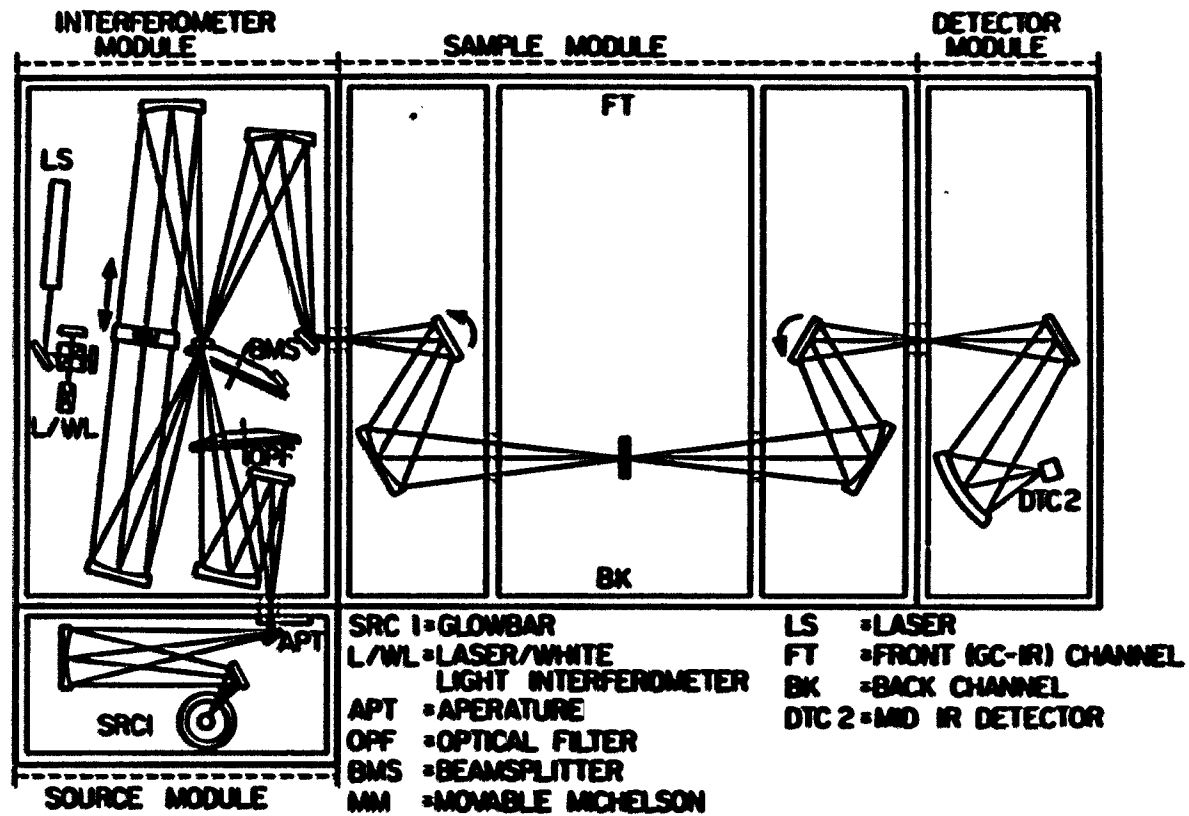


Figure 8. The schematic diagram of the optical system of the FTIR spectrometer for mid-IR

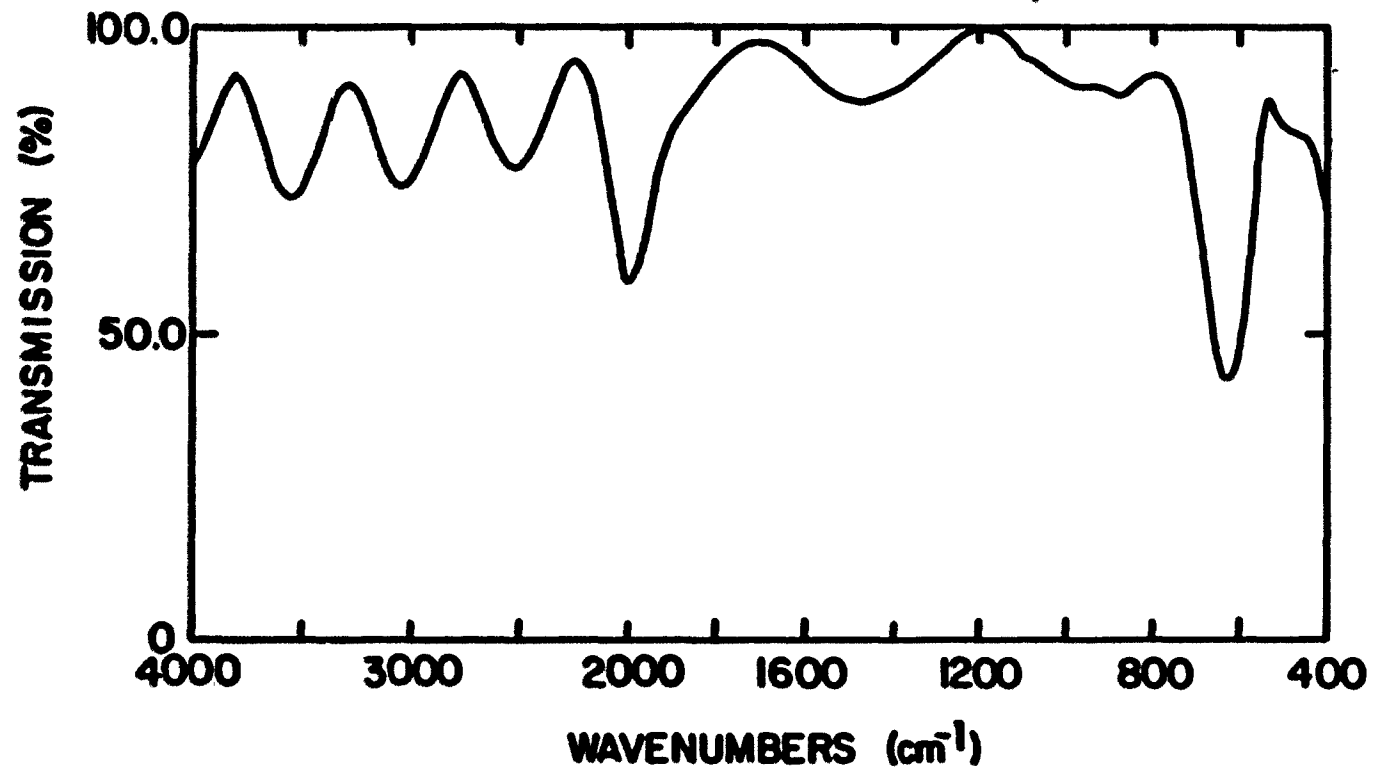


Figure 9. Typical infrared transmission spectrum of a-Si:H represented by sample S58

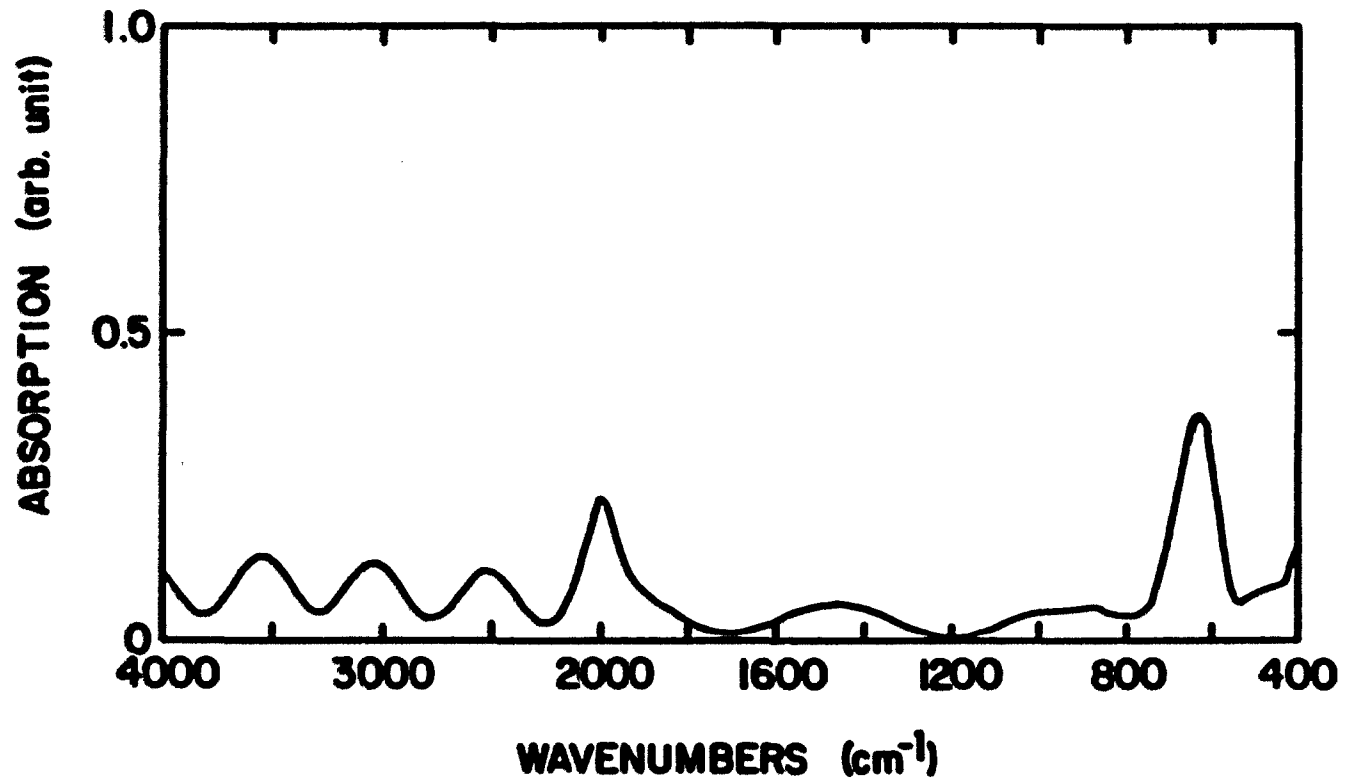


Figure 10. Typical infrared absorption spectrum of a-Si:H represented by sample S58

c-Si substrate. The interference is sinusoidal in the whole range 100% transmission with the wavelength of oscillation given by [28]:

$$\lambda = \frac{1}{2n(\lambda)t} \quad (9)$$

or

$$t = \frac{1}{2\lambda n(\lambda)} \quad (10)$$

where t is the film thickness. The index of refraction, n , is wavelength dependent. But in this wavelength range, an estimate of $n = 3.4$ is a reasonable value for a-Si. The absorption gives a good approximation of the film thickness which can be compared with the results of the other methods described in Section 3.1.

The intensity of the peak in the infrared measurements also supply information about the hydrogen-silicon bonding, hence, the hydrogen concentration in the film. The presence of sharp absorption peaks in Figure 9 reveals a variety of vibrational modes associated with Si-H bonds: stretching (2000 cm^{-1}), bending (879 cm^{-1}), and wagging/rocking (640 cm^{-1}) as reported in Refs. [28] and [9]. The number of hydrogen bonds, N_H , contributing to a given band, can be obtained as follows [10]:

$$N_H = \frac{cn\omega t}{2\pi^2} \frac{m^*}{e_s^*} \int \frac{\alpha(\omega)}{\omega} d\omega \quad (11)$$

where c is the speed of light, ω_t the frequency of the band, m^* the reduced mass and e_s^* , the effective charge for Si-H bond. Equation (11) can be simplified as

$$N_H = A^* I^* \quad (12)$$

where

$$A^* = \frac{cn\omega_t}{2\pi^2} \frac{m^*}{e_s^{*2}}$$

is the prefactor in front of the integral, and I^* is the integral of absorption over the frequency for a given peak. Using a nuclear reaction technique, Shanks et al. [1] have determined empirically the value of the prefactor A^* for all vibrational modes as listed in Table 2.

The absolute hydrogen concentration was calculated from the integrated strength of the wagging-rocking-rolling bands at 640 cm^{-1} [29] with the computer, using a straight line as a base line with the upper and lower integration limit at 800 and 540 cm^{-1} . Since the FTIR IBM IR98 uses the definition for the absorbance as $A_b = \log_{10} \frac{I}{I_0}$, where I and I_0 are the transmitted and incoming intensities of the light, a constant 2.303 ($= \ln 10$) must be used to multiply the result of the integration to give a correct value of I , and hence, the value of the hydrogen concentration. The hydrogen concentration N_H is then normalized to at. % by dividing it by $5.12 \times 10^{22} \text{ atom/cm}^3$ which is the commonly used standard value

Table 2. The empirically determined value of the prefactor A

Wave number	640	840-890	2000	2090	2100 (cm ⁻¹)
Node	Wag	Bend	Stretch	Stretch	Stretch
Bonding	Si:H Si:H ₂	Si:H	Si:H (isolated)	Si:H (cluster)	Si:H ₂
Prefactor A	1.6 x 10 ¹⁹	2 x 10 ²⁰	2.2 x 10 ¹⁹	1.7 x 10 ²⁰	9.1 x 10 ¹⁹ (cm ⁻²)

for atomic density of a-Si.

3.4. Electrical Measurements

To determine the electrical conductivity and activation energy of a-Si:H films, I-V measurements were performed for coplanar configuration samples (Figure 5). The schematic diagram of the electrical circuit used in this measurement is shown in Figure 11, where a HP Harrison 6299B DC power supply (0-320V, 0-0.1A) is connected in series with a standard resistor (100 K Ω) and with the measured sample, while the voltages across the power supply, V_s , and the standard resistor, V_R , were measured with two high input impedance HP 3465A and B digital multimeters. During the measurements, the sample was placed on a light-tight black box, mounted on a thermo-chuck which has controllable temperature from ambient to 400° C, to allow measurements as a function of temperature. The electrical contact to the sample was made by two micro-manipulator probes, and the applied d.c. voltage was varied from 50 to about 200 volts.

If the thickness of the sample, the gap width, and the aluminum length are t , w , and l , respectively, the resistivity of the film, ρ , is then given by

$$\rho = R \frac{t l}{w} \quad (13)$$

and the conductivity, σ , is

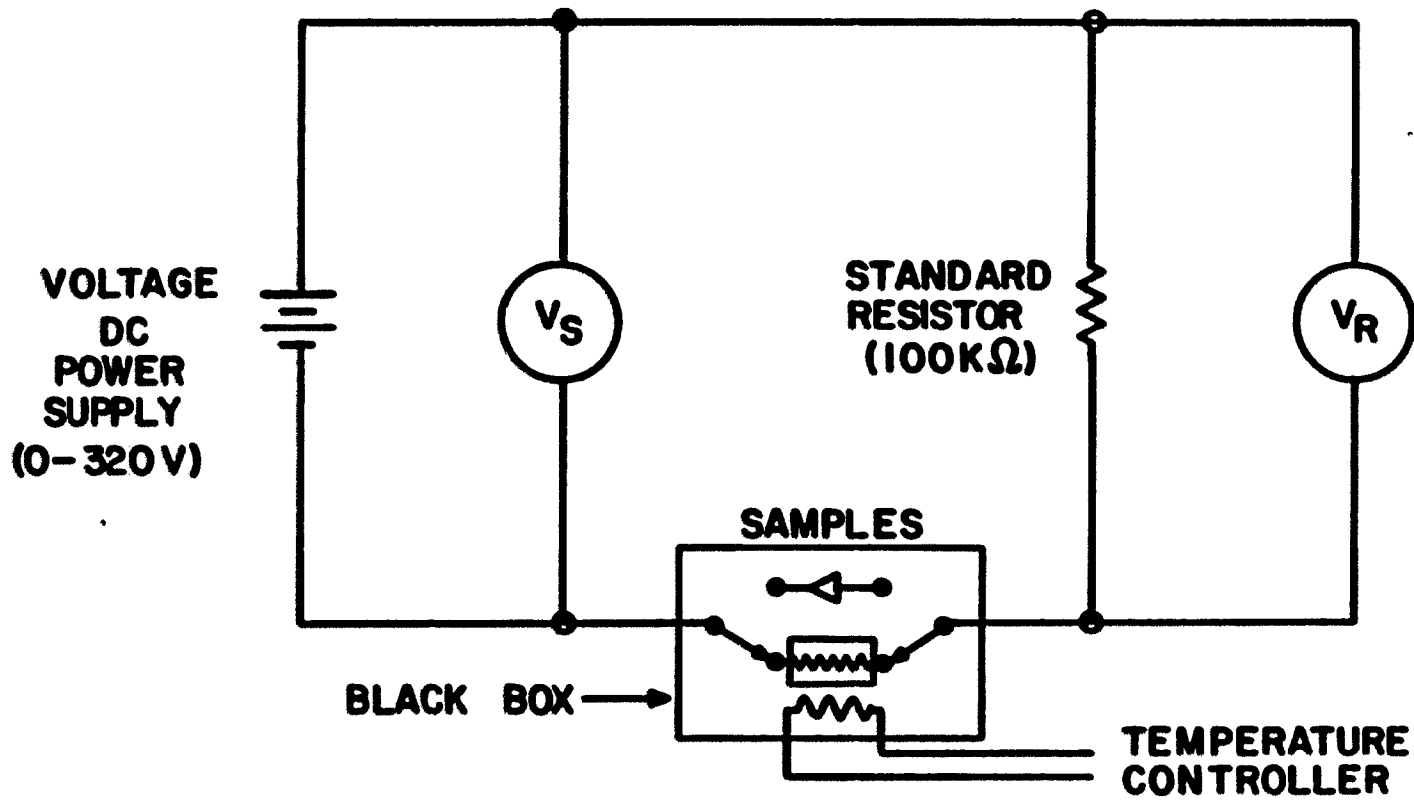


Figure 11. Electric circuit used to measure I-V characteristics of the samples

$$\sigma = \frac{1}{\rho} = \frac{W}{Rt\ell} . \quad (14)$$

where R is the resistance across the gap between the electrodes, determined from the slope of the I-V plot for the sample.

Thermal activation energy was determined from the dependence of the dark conductivity on temperature. For any material, the electrical conductivity can be given by [30]

$$\sigma = \sum_i n_i q \mu_i , \quad (15)$$

where n_i is the carrier density, q the electronic charge, μ_i the mobility, and the summation is over the various possible conduction channels. In amorphous semiconductors, there are three possible mechanisms of conduction [30-32]. First is conduction by hopping in localized states at the Fermi energy. Secondly, there is hopping at band tails. Finally, there is conduction in the extended states above the mobility edge. For a sufficiently low density of states at E_F ($N(E_F) \leq 10^{18} \text{ eV}^{-1} \text{ cm}^{-3}$) and at temperature equal to or above room temperature, the hopping component can be neglected [30]. Thus, the conductivity can be expressed in the form [31]

$$\sigma = q \int N(E) \mu(E) kT \frac{\partial f(E)}{\partial E} dE , \quad (16)$$

where $N(E)$ and $f(E)$ are the density of states and the Fermi Diract distribution function, respectively, k the Boltzmann

constant, and T the absolute temperature. For undoped a-Si:H, the Fermi level E_F is expected to be near the middle of the band gap. Therefore, $f(E)$ becomes a Boltzmann distribution function, i.e.,

$$f(E) = \exp[-(E-E_F)/kT] . \quad (17)$$

If the density of states and the mobility are constants, and equal to $N(E_C)$ and μ_C , respectively, Equation (16) becomes

$$\sigma = q N(E_C) kT \mu_C \exp[-(E_C-E_F)/kT] , \quad (18)$$

where $N(E_C)$ is the density of states at the bottom of the conduction band, and μ_C is the average mobility. Letting

$$\sigma_0 = q N(E_C) kT \mu_C , \quad (19)$$

and

$$E_a = E_C - E_F , \quad (20)$$

Equation (18), then becomes

$$\sigma = \sigma_0 \exp[- E_a/kT] . \quad (21)$$

Assuming that the prefactor σ_0 has a small dependence on temperature, $\ln \sigma$ will be linearly dependent on $1/T$, and the activation energy E_a can be determined from the slope of the graph of $\ln \sigma$ vs $1000/T$.

3.5. Schottky Diodes

The determination of the Schottky barrier heights was done on Schottky diodes formed by evaporating gold on undoped a-Si:H films which has been discussed in detail in Section 2.2. The forward current densities at low voltages can be written in the general diode equation form:

$$J = J_s [\exp (qV/\eta kT) - 1] , \quad (22)$$

where J_s is the saturation current density, V the applied voltage, and η the diode's quality factor which is defined as

$$\eta = \frac{q}{kT} \frac{\partial V}{\partial \ln J} .$$

Assuming that the diodes obey the thermionic emission-diffusion theory, the saturation current density is given by [33]

$$J_s = A^{**} T^2 \exp \left(- \frac{q \phi_B}{kT} \right) , \quad (23)$$

where A^{**} is the effective Richardson constant for thermionic emission-diffusion, and ϕ_B is the barrier height. The saturation current density, J_s , is determined from extrapolating the current density at zero voltage on a plot of \ln current density vs forward bias voltage. The barrier height, ϕ_B , can be obtained from the equation

$$\phi_B = \frac{kT}{q} \ln \left[\frac{A^{**} T^2}{J_s} \right] . \quad (24)$$

At room temperature, the value of ϕ_B is not very sensitive to the choice of A^{**} because A^{**} appears in the argument of the logarithm.

3.6. Space Charge Limited Current Measurements

The Space Charge Limited Current (SCLC) measurements were made on the Schottky diodes (Figure 3) using an electric circuit as shown in Figure 11. For a given applied voltage, majority carriers (electrons) are injected at the molybdenum/ n^+ contact ($x=0$) and collected at gold counter electrode ($x=t$) by the forward bias (Figure 12). Most of the charge, Q , is forced into the semiconductor, condenses in the trap states between the equilibrium Fermi level (E_{F0}) and the quasi-Fermi level (E_F). So the shift in the Fermi level will be proportional to the space charge Q which is, in turn, proportional to the applied voltage V . The quasi Fermi level position in the band gap is shown in Figure 12. The Fermi level bends down at the metal/semiconductor interface ($x=t$) and bends up to infinity at the semiconductor/ n^+ contact ($x=0$). The free carrier density is, then, given by [20]

$$n(x) = n_c \exp [-(E_c - E_{F0})/kT] \cdot \exp (\Delta E/kT) \quad (25)$$

where n_c is the number of states in the bottom kT slice of the conduction band, E_c , and $\Delta E/kT$ is the shift in the quasi-Fermi energy measured in unit of kT above the equilibrium Fermi level, E_{F0} . Using $n_{c0} = n_c \exp. [-(E_c - E_{F0})/kT]$, the

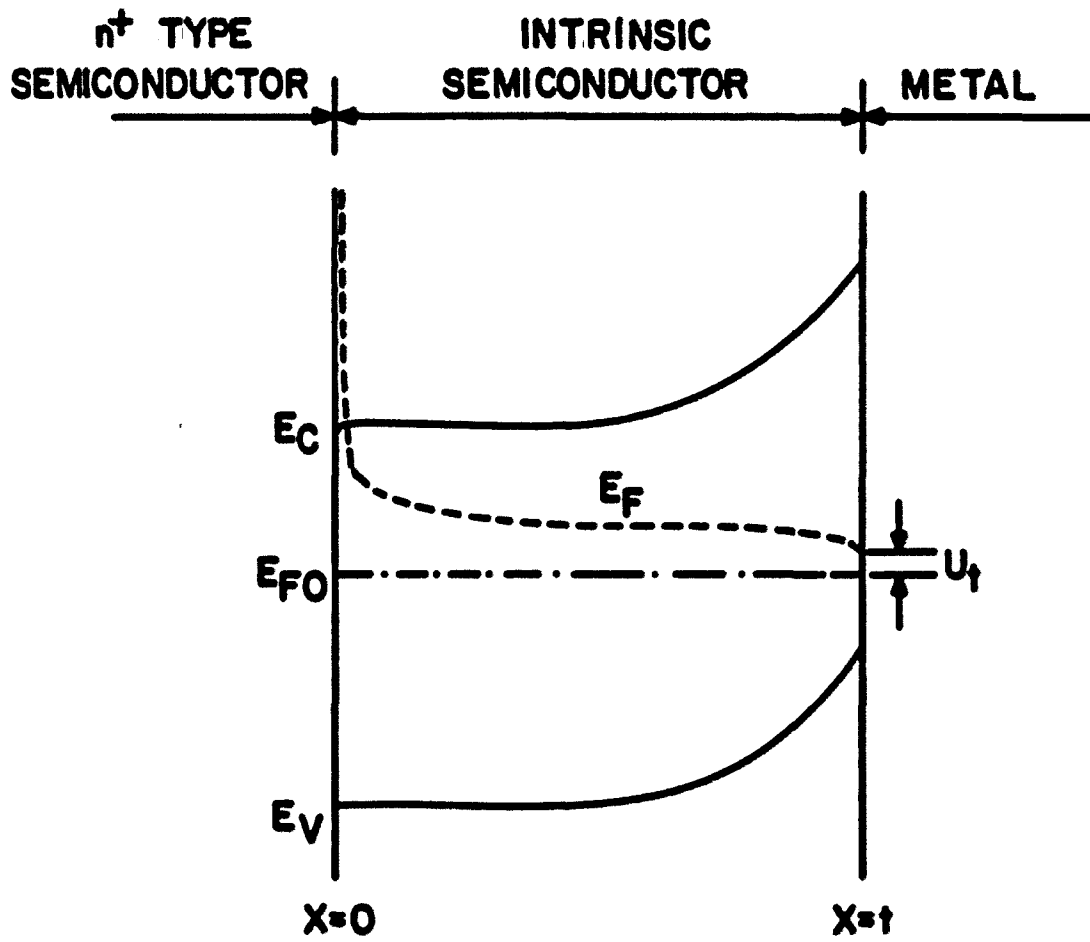


Figure 12. Energy band diagram of a Schottky diode
 -.-.- the equilibrium Fermi level (E_{F0})
 ----- the quasi-Fermi level (E_F)

thermal equilibrium density of free electrons, and $u(x) = \Delta E/kT$, Equation (25) becomes

$$n(x) = n_{c0} \exp. [u(x)] . \quad (26)$$

The following assumptions are used for the SCLC:

(1) Samples are films of uniform thickness t , and the density of states and mobility of majority carriers are spatially uniform and field independent.

(2) The gap state density, $N(E)$, varies continuously and slowly over energies of the order of kT . The charge density, $\rho(x)$, only depends on the local shift in the quasi-Fermi energy, $u(x)$, and can be written as [19];

$$\rho(x) = -q \int_0^{kTu(x)} N(E_{F0}+E)dE = \rho(u) . \quad (27)$$

(3) For SCLC measurements diffusion current is neglected. The current density, J , is uniform and represented by

$$J = q\mu n(x) \epsilon(x) , \quad (28)$$

where μ is the electron mobility, and $\epsilon(x)$ is the local electric field.

(4) The injecting contact, molybdenum/ n^+ contact, works as a reservoir of free electrons, i.e.,

$$u(x=0) = \infty, \rho(x=0) = -\infty, \text{ and } \epsilon(x=0) = 0 . \quad (29)$$

Poisson's equation satisfied at all points in the semiconductor can be written as

$$\frac{d\epsilon}{dx} = - \frac{\rho(u)}{\epsilon_s}, \quad (30)$$

where ϵ_s is the dielectric permittivity of the semiconductor, and the applied voltage is

$$V = - \int_0^t \epsilon(x) dx. \quad (31)$$

Based on the Equations (27), (28), and (30), Weisfield [19] solved the equation for recovering the density of states in the band gap, $N(E)$, from the experimental I-V characteristic. As shown in the Appendix, the density of states in the band gap can be expressed in the form

$$N(E_{FO} + \Delta E_F) = \frac{sV}{qkTt^2} \left[a(2-a) + \frac{c-b(3-2a)}{(1-a) + b/(2-a)} \right] \quad (32)$$

and

$$\Delta E_F = kT \ln \left[\frac{J}{J\Omega(2-a)} \right] \quad (33)$$

where a , b , and c are the first, second, and third derivatives of $\ln V$ with respect to $\ln J$, respectively, and

$$J\Omega = \frac{\sigma V}{t} \quad (34)$$

where $\sigma = q\mu n_{CO}$ is the thermal equilibrium conductivity.

From the I-V relation obtained from the measurements, one

can calculate $\ln V$ vs $\ln J$, and using a least squares approximation, the data are fit with a polynomial function of degree 8. Essentially, the same result is obtained for both 7 and 8th degree polynomials. The data match very well with the function as shown for the typical curve for the samples in Figure 13.

$$\text{Calculating } \frac{d \ln V}{d \ln J}, \frac{d^2 \ln V}{d \ln J^2}, \text{ and } \frac{d^3 \ln V}{d \ln J^3}, \text{ and}$$

inserting the results in Equations (32) and (33), one can obtain $N(E_{F0} + \Delta E_F)$ at every point around E_{F0} .

Further discussion is required to clarify the reasons that the current is dominated by drift alone. Under the assumptions that the electric field is zero and the density of the free electron is infinite at the injecting contact, the current mechanism is entirely dominated by diffusion. In addition, with a Schottky barrier as the counter electrode, diffusion currents dominate for applied voltages less than the built in potential (~ 0.2 V). With all these limitations, however, one could expect that for thick enough sample, i.e., at distances far enough from the injecting contact and for sufficiently large applied voltage (~ 1.0 V), the diffusion current can be neglected compared to the drift current. To determine the extent of this problem, some measurements for I-V relations have been done for several samples which have different thicknesses varying from $0.60 \mu\text{m}$ to $3.0 \mu\text{m}$. The

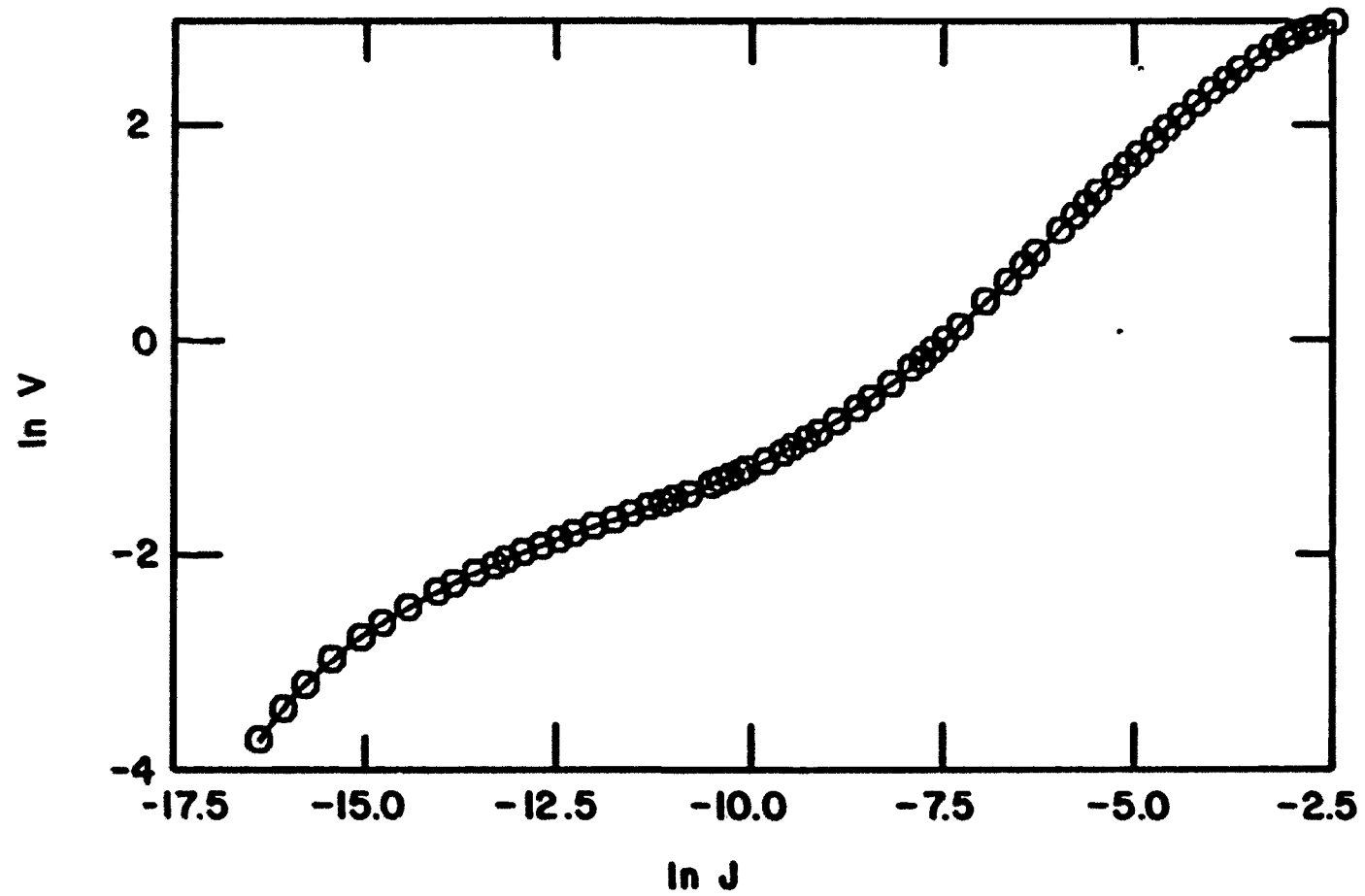


Figure 13. $\ln V$ vs $\ln J$ plot for sample S81

○ is for the data

— is the polynomial function degree 8

samples were made under the same nominal deposition parameters.

4. RESULTS AND DISCUSSION

4.1. Vibrational Spectra of a-Si:H

The IR vibrational absorption spectrum of a-Si:H has been extensively used to investigate local bonding configuration of hydrogen in the disordered matrix of a-Si. At least three possible bonding configurations are expected from the vibration spectra, those which are associated with SiH, SiH₂, and SiH₃. Considering the fact that the mass ratio of the hydrogen to silicon is very small (1.0079 to 28.0855), there are, consequently, normal modes involving essentially pure hydrogen atom displacements. The schematic representation of the possible vibrational modes involving the H motions is displayed in Figure 14 reproduced from Brodsky et al. [10], and the related frequencies are written under the indicated modes.

Figures 15a-15h show the absorption spectra between 2500 cm⁻¹ and 400 cm⁻¹ for the a-Si:H films with various hydrogen atomic concentration. The absolute concentrations of hydrogen in the films have been estimated from the integrated strength of the wagging-rocking band vibration at about 640 cm⁻¹, as described in Chapter 3. All of the spectra for the films with hydrogen content \leq 20 at. % show bands with peaks at 2000 cm⁻¹ and 640 cm⁻¹, while the one with 24.6 % at. H has peaks at 2100 cm⁻¹ and 640 cm⁻¹. An addition, bending mode occurring at 890 cm⁻¹ starts to appear for samples with hydrogen content

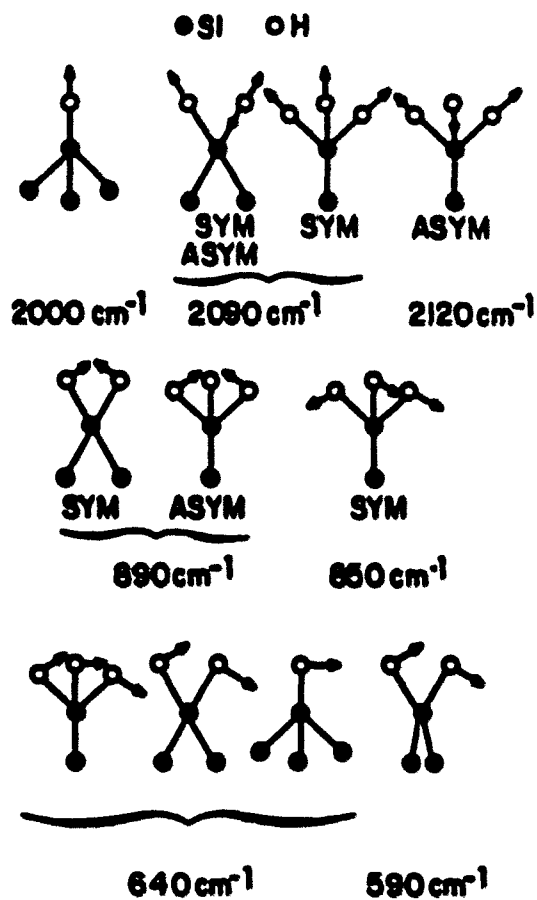


Figure 14. Schematic illustration of the vibration spectra of silicon-hydrogen bonds. From top to the bottom, stretching, bending, and wagging, and rocking models of Si:H , Si:H_2 , and Si:H_3 . SYM or ASYM indicate symmetric and asymmetric modes. The solid circles represent Si atoms and the hollow circle represent H atoms (after Brodsky et al., [10])

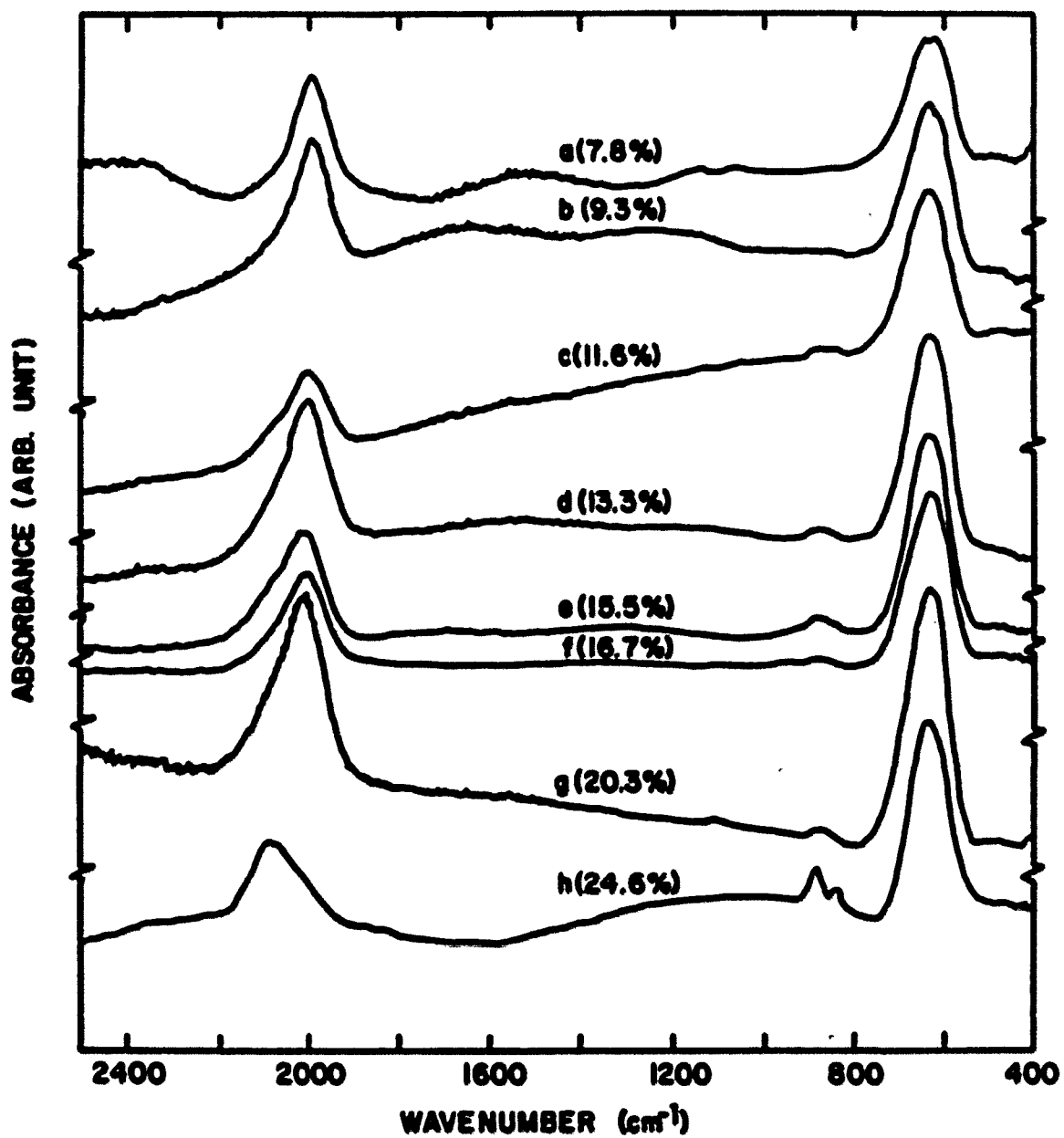


Figure 15. Infrared vibrational spectra of samples deposited with different atomic percentage of hydrogen content (indicated in the parentheses)

≥ 10 at. %, and for the sample with 24.6 % at. H a doublet of the bending modes start to show peaks at 890 and 850 cm^{-1} . The strength and the occurrence of this doublet is critically dependent on the hydrogen content of the films. All of these results are in agreement with the observation by Lucovsky [34] that samples with low hydrogen content ($\sim 3-5$ at. %) are dominated by absorption bands about 2000 cm^{-1} and 640 cm^{-1} , while samples containing much more hydrogen ($\sim 15-25$ at. %) contain additional spectral features near 850-900 cm^{-1} . These latter have been interpreted as being a signature of more than one hydrogen atom being bonded to a given silicon atom, as for example in SiH_2 and SiH_3 groups. Shanks et al. [1] reported that the 2000 cm^{-1} band of Si is due mainly to isolated SiH bonds (distributed phase), while 2090 cm^{-1} band was related to clusters of four SiH bonds (clustered phase) as shown in Figure 16. In addition, modes at 2090 cm^{-1} and the bond bending bands at 890 and 840 cm^{-1} are associated with the presence of SiH_2 bonds.

It is likely that the strength of the distributed phase increased with increasing hydrogen concentration up to about 10 at. % where it saturates. On the other hand, the strength of the clustered phase continues to increase with increasing hydrogen content such that at about 24 % at. H it dominates the distributed phase and shifts the absorption peak from 2000 cm^{-1} (Figures 15a-15g) to 2090 cm^{-1} (Figure 15h). The emergence of peaks at 840 and 890 cm^{-1} indicate SiH_2 bonds

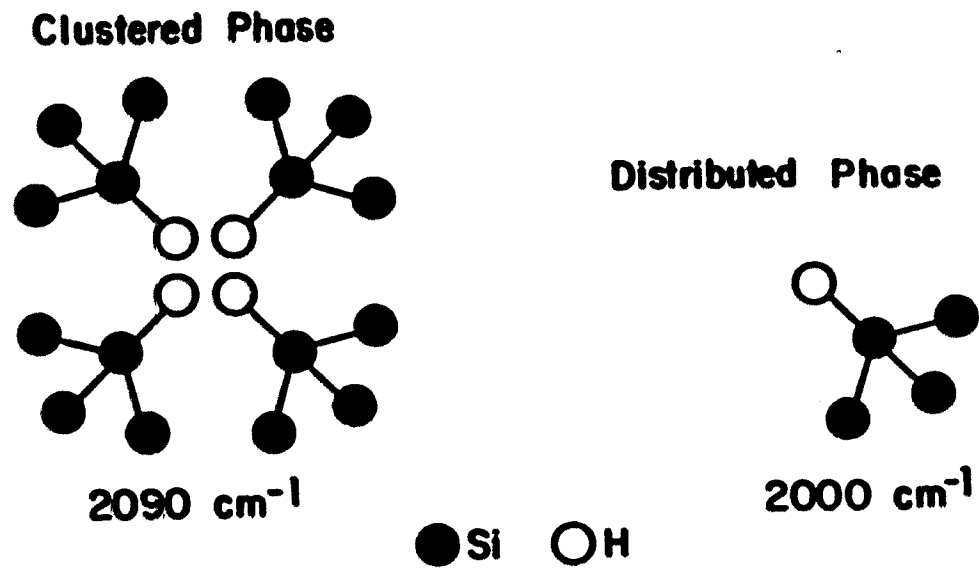


Figure 16. Schematic diagram of the clustered and distribution forms of Si:H bonds. The Si atoms are denoted by solid circles, and H atoms by hollow circles (after Shanks et al. [1])

which also contribute near 2090 cm^{-1} . No doublet absorption peaks at about 2100 cm^{-1} as reported by Moustakas [35] were observed for these samples even for hydrogen content as high as 24.6 at. %. Figure 17 shows the Si-H stretching vibrations for a number of films produced in this laboratory under negative bias conditions as contrasted with Moustakas' results shown in Figure 18. Moustakas' films were produced at negative bias, with deposition temperature = 275° C , power = 200 W, argon pressure = 15 m torr, and the target-substrate distance = 5 cm. From Figure 18 it is shown that the doublet peaks start to appear even for 8 at. % H. Brodsky et al. [10] in their study to control the bonding of hydrogen in the silicon network also reported that at about 2000 cm^{-1} the stretching vibration was found to be always a doublet. The difference between these two reports and the results observed in this laboratory is in the preparation conditions of the samples. Jeffrey et al. [36] demonstrated that sputtered $\alpha\text{-SiH}_x$ films having only the 2000 cm^{-1} Si-H stretching mode can be made, if the substrates are inserted inside the plasma below the edge of the dark space. At higher H concentrations, a contribution is observed at 2090 cm^{-1} due to SiH clusters but no contributions at 840 and 890 cm^{-1} are seen.

For completeness, it is reported also that there is no evidence of the presence of oxygen. The SiO vibrational absorption band appears at 1050 cm^{-1} when oxygen is incorporated into the film [34]. For all samples, there is no

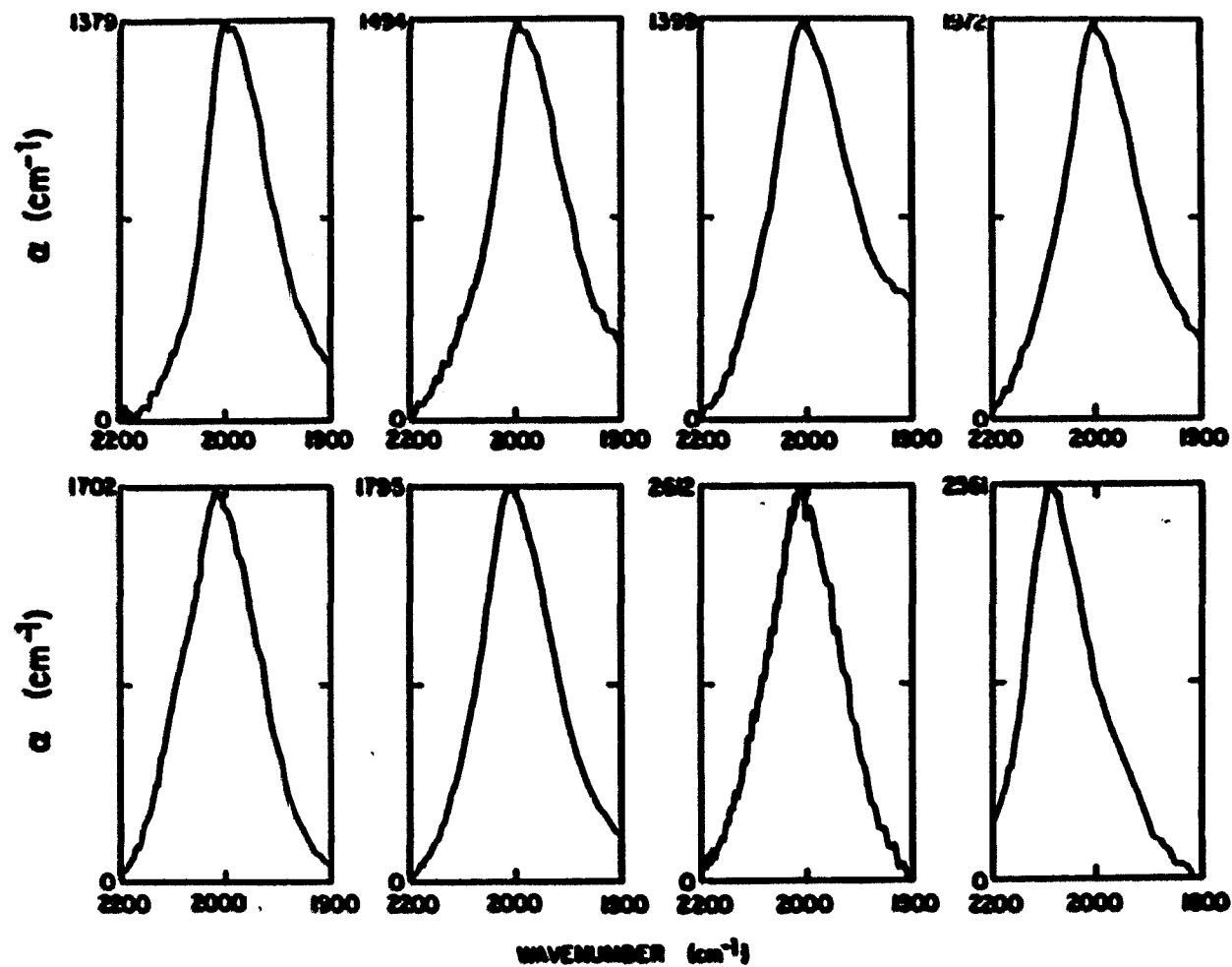


Figure 17. The Si:H stretching vibrations for a number of a-Si:H films. Indicated next to the samples spectra are the hydrogen content in the films

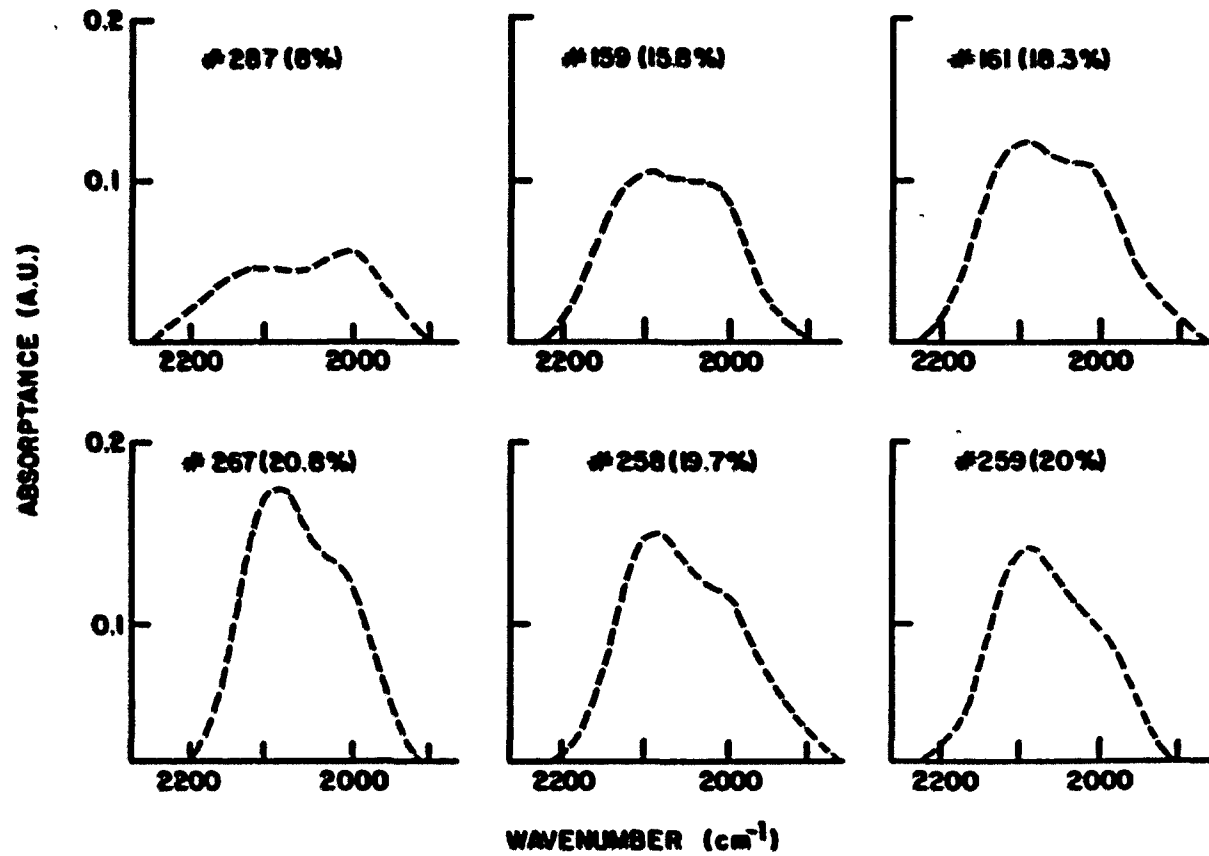


Figure 18. The Si:H stretching modes for samples produced under negative bias conditions (deposition temperature = 275°C, r.f. power = 200 watts, and $P_{Ar} = 15$ mt). Indicated next to the sample number is the hydrogen content in the films (after Moustakas [35])

sign of a background absorption with a broad shape near 1050 cm^{-1} which could be associated with oxygen. The result above is confirmed by the result of the Auger depth profile measurements as will be discussed in Section 4.5.

4.2. Optical Properties

In amorphous semiconductors, the optical absorption coefficient vs. photon energy plot has a shape as shown in Figure 19. There appears to be three regions, A, B, and C [37]. Region A is a power-law region ($\alpha \geq 10^4 \text{ cm}^{-1}$) where the absorption coefficient, α , is proportional to $(E - E_g^{\text{opt}})^r$. Region B, the exponential part, is called the Urbach edge ($1 \text{ cm}^{-1} < \alpha < 10^4 \text{ cm}^{-1}$), and region C, the weak absorption tail ($\alpha < 1 \text{ cm}^{-1}$), is ascribed to optical excitation from defect states deep in the gap. There is no sharp delineation between these three overlapping regions. The weak absorption tail is not detected in Figure 20 which shows the absorption coefficients as a function of energy for four a-Si:H samples. The absorption measurements for this C region are difficult to make, even using the photoconductivity method. The a-Si:H films are thin and partly reflecting, and their micro-roughness produces a background of scattered light which creates noise comparable to the signals. The data in Figure 20 show that the absorption edge shifts toward higher energy with increasing hydrogen content. For high hydrogen concentrations, the optical absorption coefficient falls off

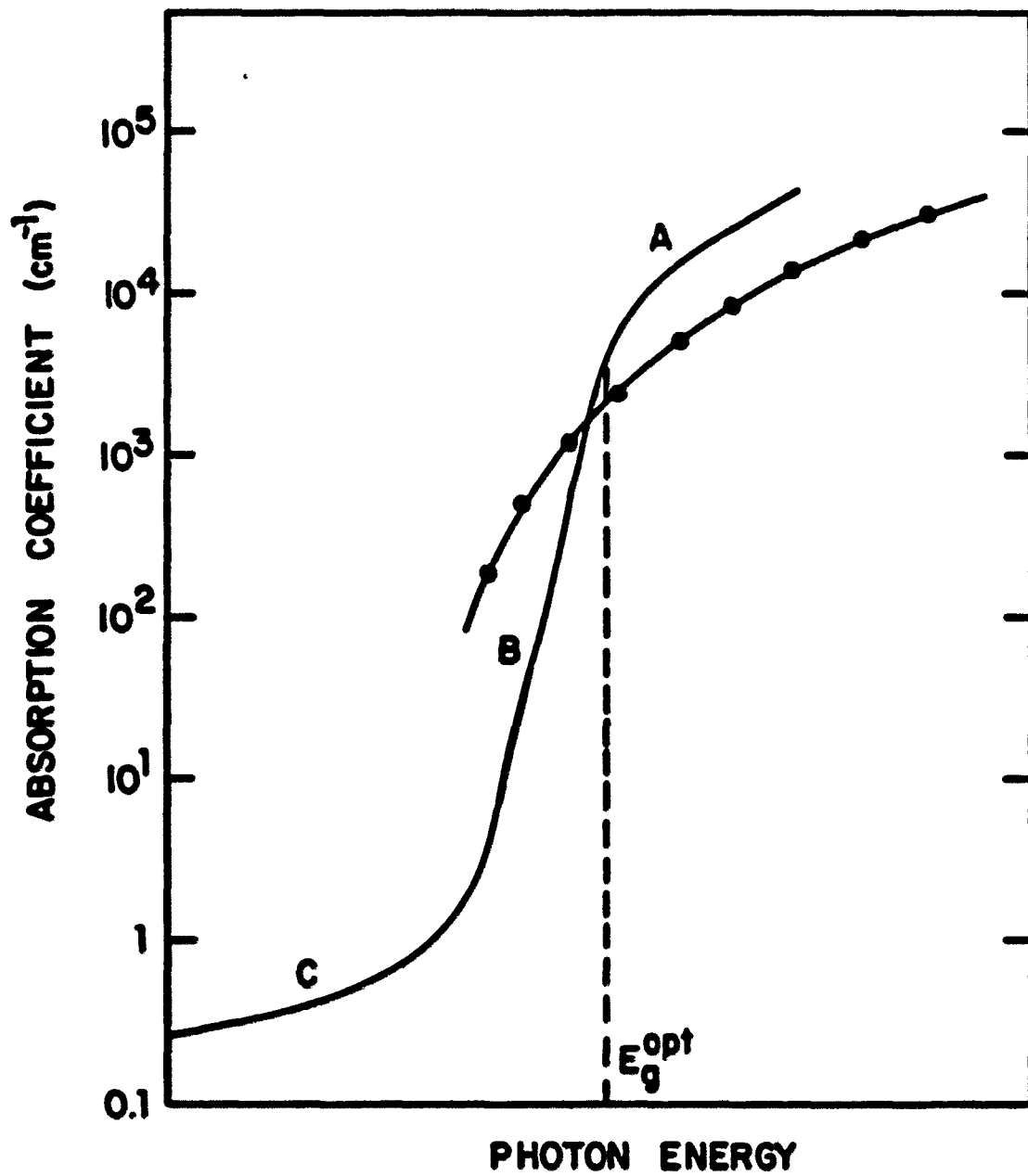


Figure 19. The absorption edge of an amorphous semiconductor which has three region the power laws (A), the exponential (B), and the weak absorption tail (C).
 ●—● for crystal Si

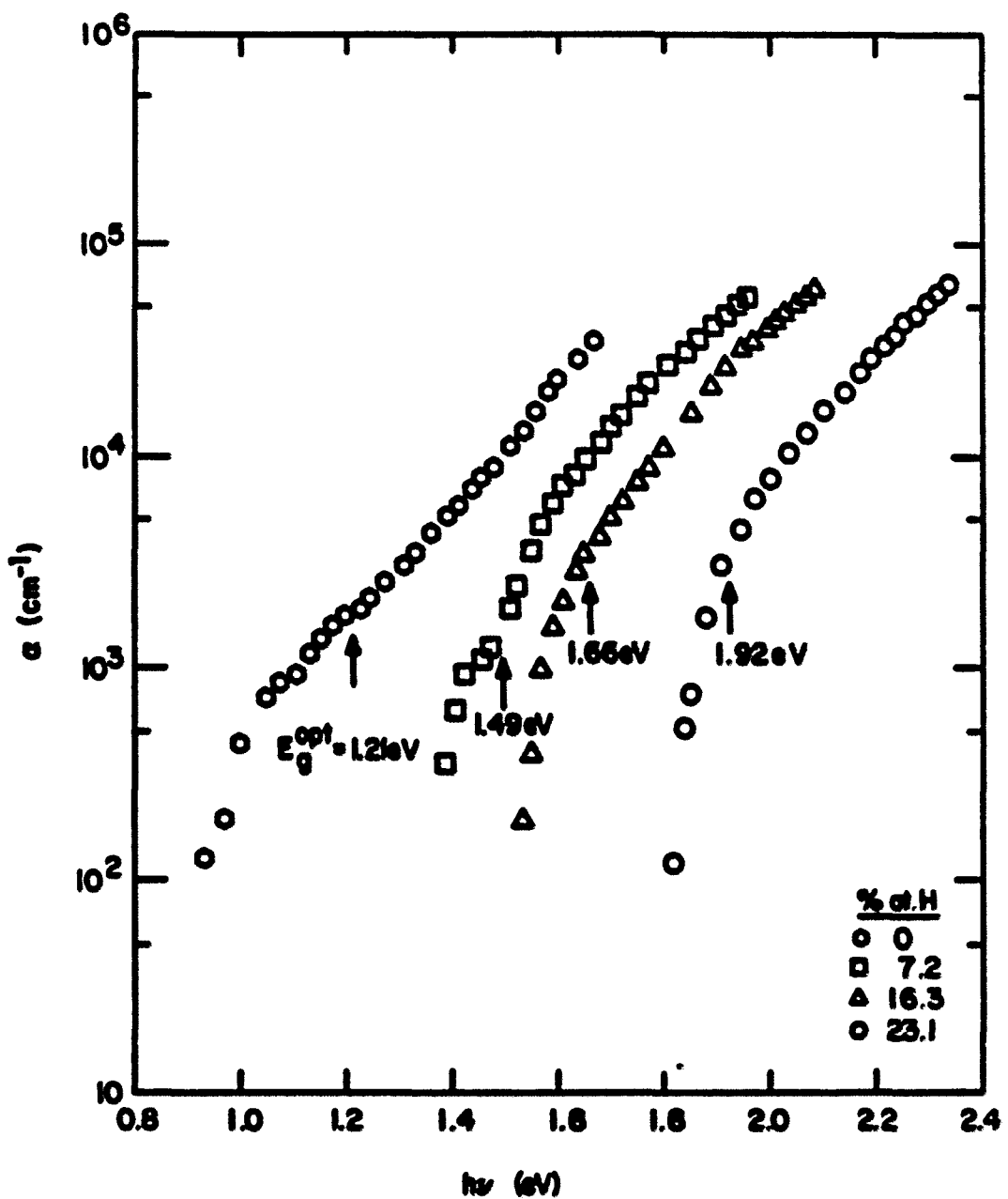


Figure 20. Optical absorption coefficient versus photon energy for a number of a-Si:H films with different hydrogen content. Indicated with the arrows are the band gaps (E_g^{opt}) of the samples

rapidly with decreasing photon energy as the band edge is reached. The shift of the optical absorption edge is the effect of removal of localized states at the top of the valance band by hydrogen saturation of dangling bounds [5].

The optical band gap is derived from the high absorption region (region A), and the approach used here is based on the work of Davis [38]. With the assumption that k is not a meaningful quantum number for amorphous semiconductors and that the k -conservation selection rule which operates in crystals is relaxed, the absorption coefficient is expected to be proportional to the convolution of state densities integrated over all energies,

$$\alpha = C \int N_i(E) N_f(h\nu + E) |p|^2 dE/h \quad (35)$$

where C is a constant, the optical matrix element p associated with the transitions are assumed independent of energy and N_i and N_f are the initial and final states. For initial and final states well below the top of the valence band [E_v] and above the bottom of the conduction band [E_c], respectively, the density of states can be represented by power laws of the form,

$$N_i = N_v \sim [E_v - E]^{\epsilon_1} \quad (36)$$

and

$$N_f = N_c \sim [E - E_c]^{\epsilon_2} \quad (37)$$

Equation 35, then, becomes

$$\alpha = C' \int_{E_c-h}^{E_v} (E_v-E)^{r_1} (E+h\nu-E_c)^{r_2} dE/h\nu . \quad (38)$$

Making the substitution $y = [E_c-h\nu-E]/[E_c-h\nu-E_v]$ and denoting the optical band gap by $E_g^{opt} = E_c-E_v$:

$$\alpha = C'' \left[\int_0^1 (1-y)^{r_1} y^{r_2} dy \right] (h\nu-E_g^{opt})^{r_1+r_2+1} / h\nu , \quad (39)$$

where $\int_0^1 (1-y)^{r_1} y^{r_2} dy$ is a known integral. Thus,

$$h\nu\alpha = B^2 (h\nu-E_g^{opt})^{r_1+r_2+1} , \quad (40)$$

where B is a constant which contains the optical matrix element. When the band edges are both parabolic as in the crystal, $r_1 = r_2 = 1/2$, and Equation (40) becomes

$$\sqrt{h\nu\alpha} = B(h\nu-E_g^{opt}) . \quad (41)$$

When plotted in this form the linear extrapolation of $\sqrt{h\nu\alpha}$ versus $h\nu$ yields E_g^{opt} as shown in Figures 21 and 22. The results from the figures are listed in Table 3.

The constant B of the Equation (41) which represented the slope of the linear portions of the plot $\sqrt{h\nu\alpha}$ versus $h\nu$ increases with increased hydrogen concentration in the films as shown in Figure 23. This means that the matrix element p increases with the additional H content, and the absorption edge is narrowed. The narrowing of the absorption edge is due to decrease in band tailing caused by reducing dangling bonds

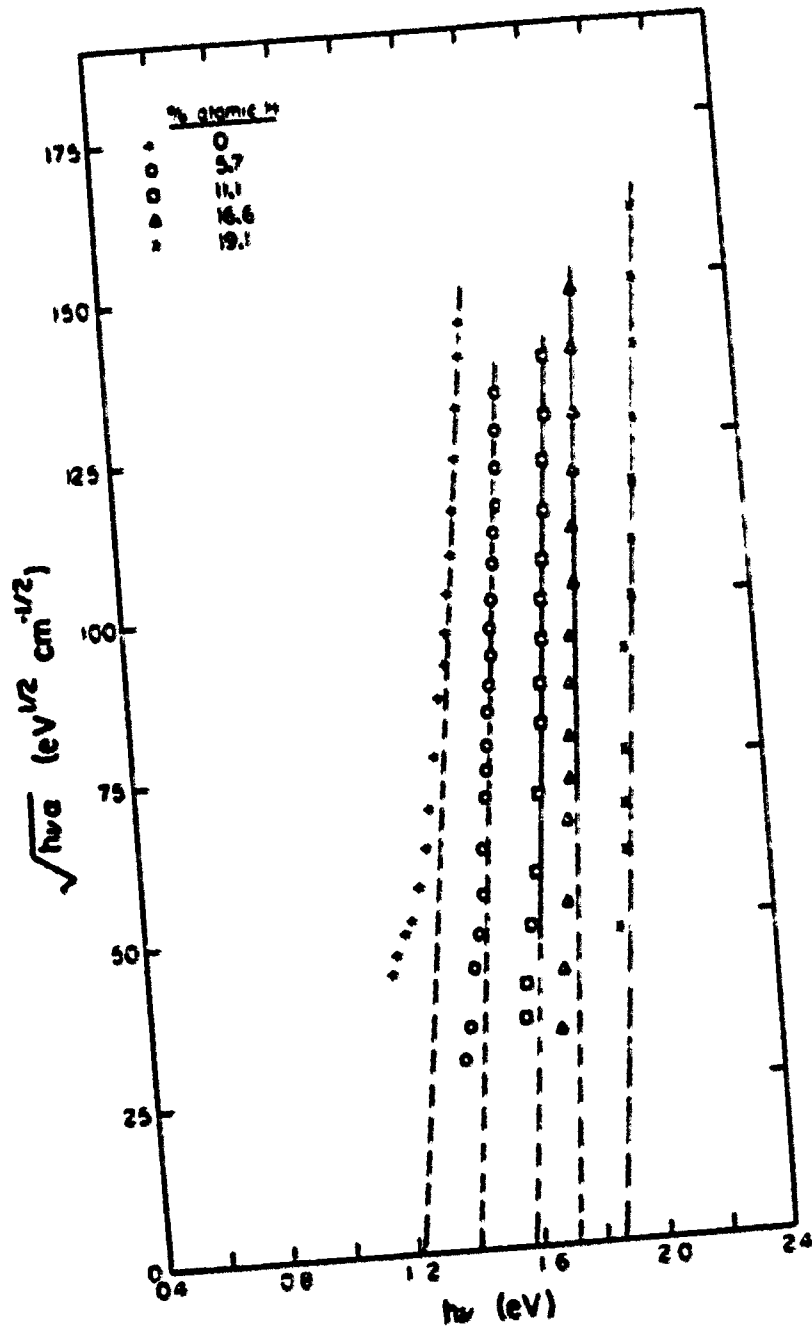


Figure 21. $\sqrt{h\nu_a}$ versus $h\nu$ for thick samples (from 2.50 to 3.30 μm). Linear portions of the plots shift to higher energy as the hydrogen content in the films increase

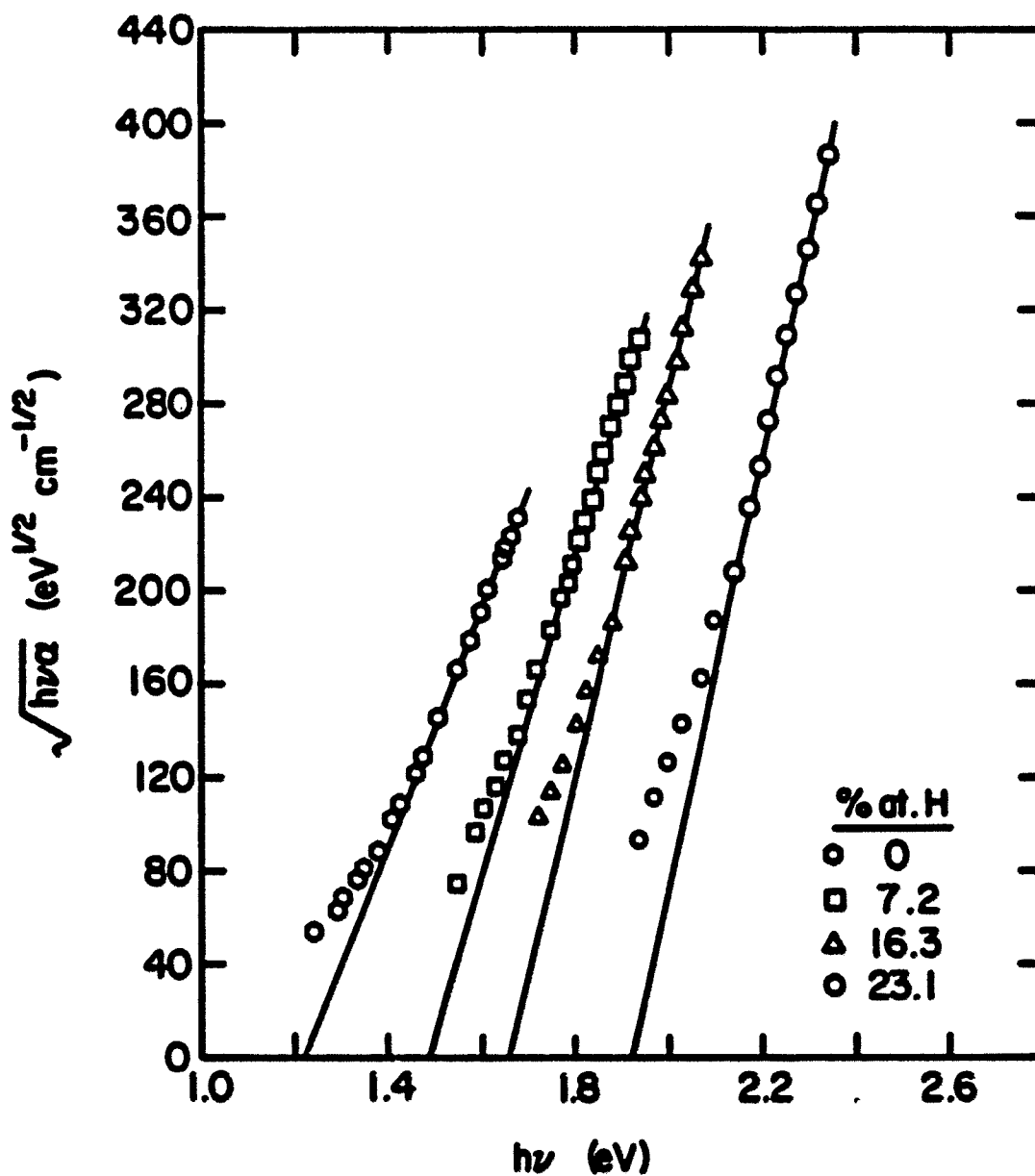


Figure 22. $\sqrt{h\nu\alpha}$ versus $h\nu$ for samples with thickness from 0.58 to 1.95 μm . The optical band gap increases with increasing hydrogen content

Table 3. Properties of 2 series of samples shown in Figures 21 and 22

Sample	Thickness (μm)	Atomic H (%)	E_g^{opt} (eV)
S107	2.75	0	1.22
S 87	3.30	5.7	1.39
S 82	3.20	11.1	1.58
S 83	2.85	16.6	1.71
S 91	2.50	19.1	1.85
S110	1.95	0	1.22
S105	0.72	7.2	1.49
S102	0.70	16.3	1.66
S104	0.58	23.1	1.92

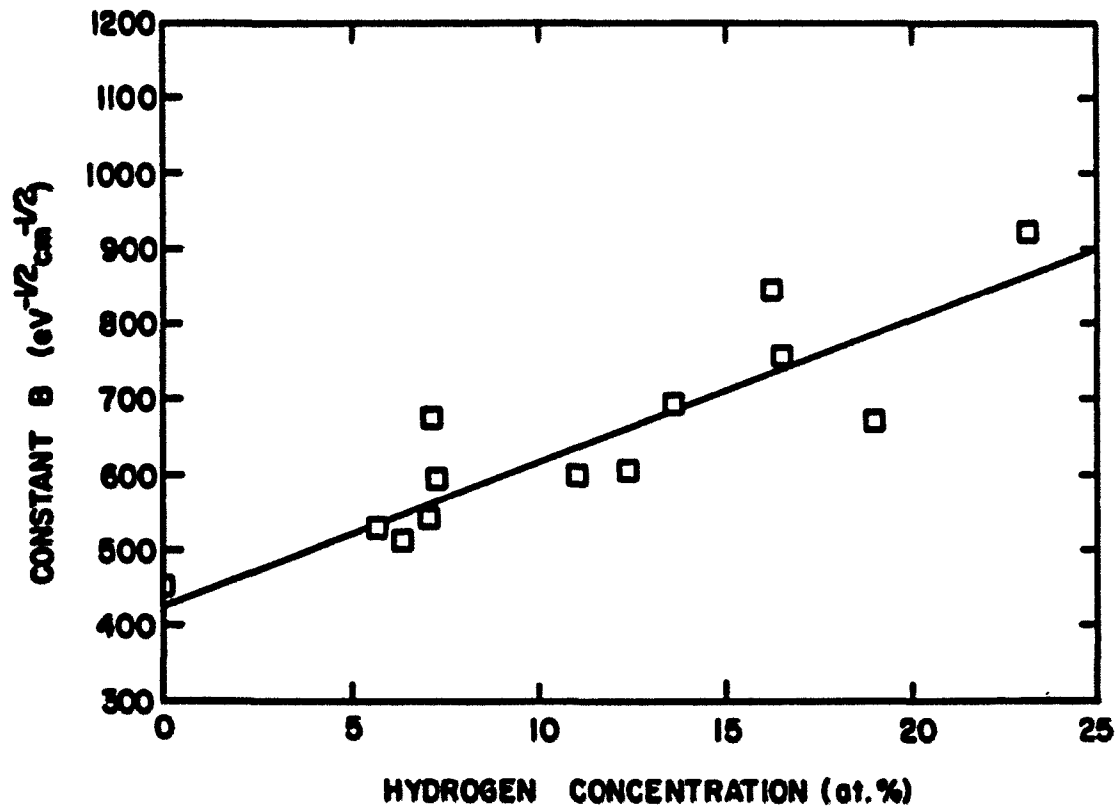


Figure 23. The dependence of the constant B on hydrogen concentration for a-Si:H films

formation as hydrogen passivates them. The passivating of the dangling bonds is shown also in Figure 24 where the optical density at 10,000 Å occurs in the low optical absorption region (region C in Figure 19), and is therefore caused mainly by defect states deep in the gap, the fast decreased of the minimum optical density from 0.58 at 0% atomic H to about 0.20 at 10% atomic H means a considerable decreased also of the dangling bonds. But the decreasing of the optical density becomes slower (almost constant) after the hydrogen content reaches 10 at. %. Under the general assumption that all of the dangling bonds were already passivated by 7 % of hydrogen content, the addition of the hydrogen was likely used to release the strain in the atomic structure of the a-Si:H and reduce the absorption at low energy while the optical band gap increases linearly.

Figure 25 shows a plot of the optical band gap, E_g^{opt} , versus hydrogen concentration for a series of a-Si:H films. The a-Si:H specimens prepared by r.f. sputtering in this laboratory yields a linear relationship between the band gap and hydrogen concentration as

$$E_g^{opt} = 1.23 + 0.030 \cdot C_H , \quad (42)$$

where E_g^{opt} is measured in eV and C_H in atomic %. Matsuda et al. [39] obtained

$$E_g^{opt} = 1.48 + 0.019 \cdot C_H \quad (43)$$

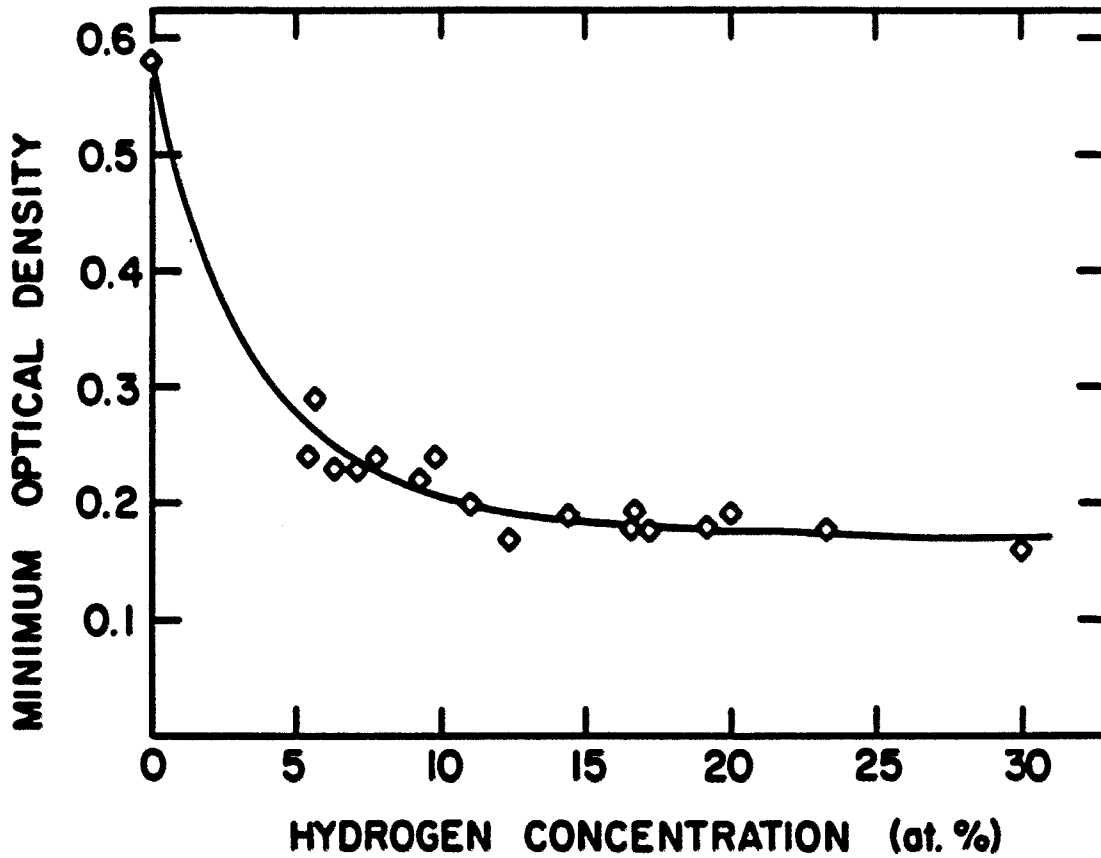


Figure 24. Hydrogen concentration dependence of the minimum optical density. The minimum optical density is almost constant for hydrogen concentration greater than 10 at. %

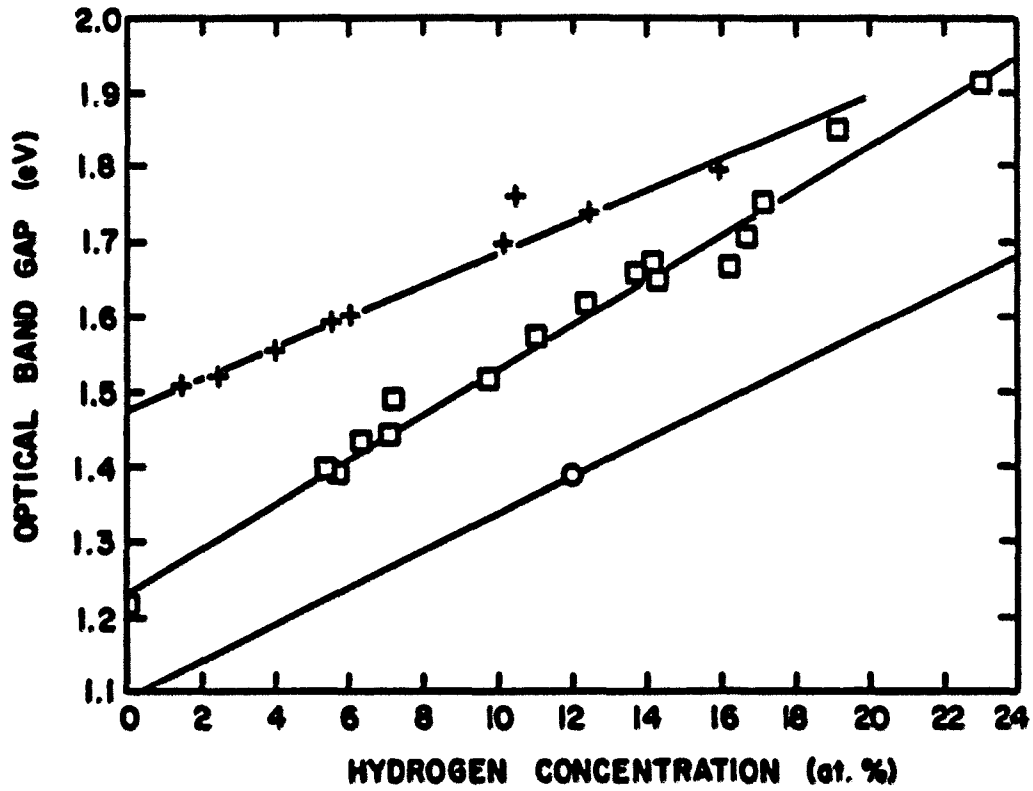


Figure 25. The optical gap E_g^{opt} versus hydrogen content of a-Si:H samples

+ data from Matsuda et al. [39];

□ from this research;

o results from Zhao and Hunklinger [40]

for a variety of films prepared by reactive sputtering and glow discharge, while Zhao and Hunklinger [40] report

$$E_g^{\text{opt}} = 1.09 + 0.025 \cdot C_H \quad (44)$$

for $0 \leq C_H \leq 35\%$. The proportionality between E_g^{opt} and C_H as expressed in Equations 42, 43, and 44 are slightly different. The difference is probably due to the preparation of the samples such as the r.f. power used, pumping speed, the proportion of the hydrogen content in the sputter gas, and the deposition temperature which are known to change the ratio of SiH to SiH₂ bonds in the materials.

4.3. Photoconductivity

Steady state d.c. photoconductivity measurements were carried out on coplanar configuration samples (Figure 5) under AM 1 (xenon) solar simulator light. Spectral dependent photoconductivity was measured using a monochromator on the light source, while the light was focused so as to produce a uniform illumination at the gap between the electrodes. The intensity of the light was about 10^{15} photon/cm² sec and the photon energy was adjusted from 1.5 to 3.0 eV. The voltage applied to the samples was held constant (100 volt) across the 0.12 mm electrode spacing for all measurements. The difference between the current measured with and without illumination is defined as the photocurrent, i_p , and can be expressed as follows [41]

$$i_p = qN_0(1-R)[1 - \exp(-\alpha t)] \eta \tau / t_T \quad (45)$$

where N_0 is the number of incident photons per second, R the reflectance, α the absorption coefficient, t the film thickness, η the quantum efficiency - defined as the number of electron-hole pairs produced per absorbed photon, τ the recombination lifetime, and t_T the carrier transit time for electrons in states above E_c .

Figure 26 shows the steady state photoresponse, $i_p/qN_0(1-R)$, representing the number of electrons flowing around the circuit for each photon entering the film, as a function of photon energy. For samples with hydrogen concentrations from 7.8 to 20 at. %, the curves show a peak between 1.65 and 1.90 eV, and the one with highest hydrogen concentration (24.6 at. %) has a peak at 2.2 eV. For the sample with 15.5% at. H, the photoresponse approaches unity for the applied voltage used. The photoconductivity increases with increasing hydrogen content for samples with hydrogen concentration less than 10 at. % (group I), then tends to be constant for hydrogen between 10 at. % to 20 at. % (group II), and starts decreasing for hydrogen contents greater than 20 at. % (group III). Moustakas et al. [42] suggested that the addition of more hydrogen gives a gradual transition of the structural short range order from essentially pure amorphous silicon at one extreme to an a-Si:H ordered alloy at the other. The argument that the Si-H antibonding state energies

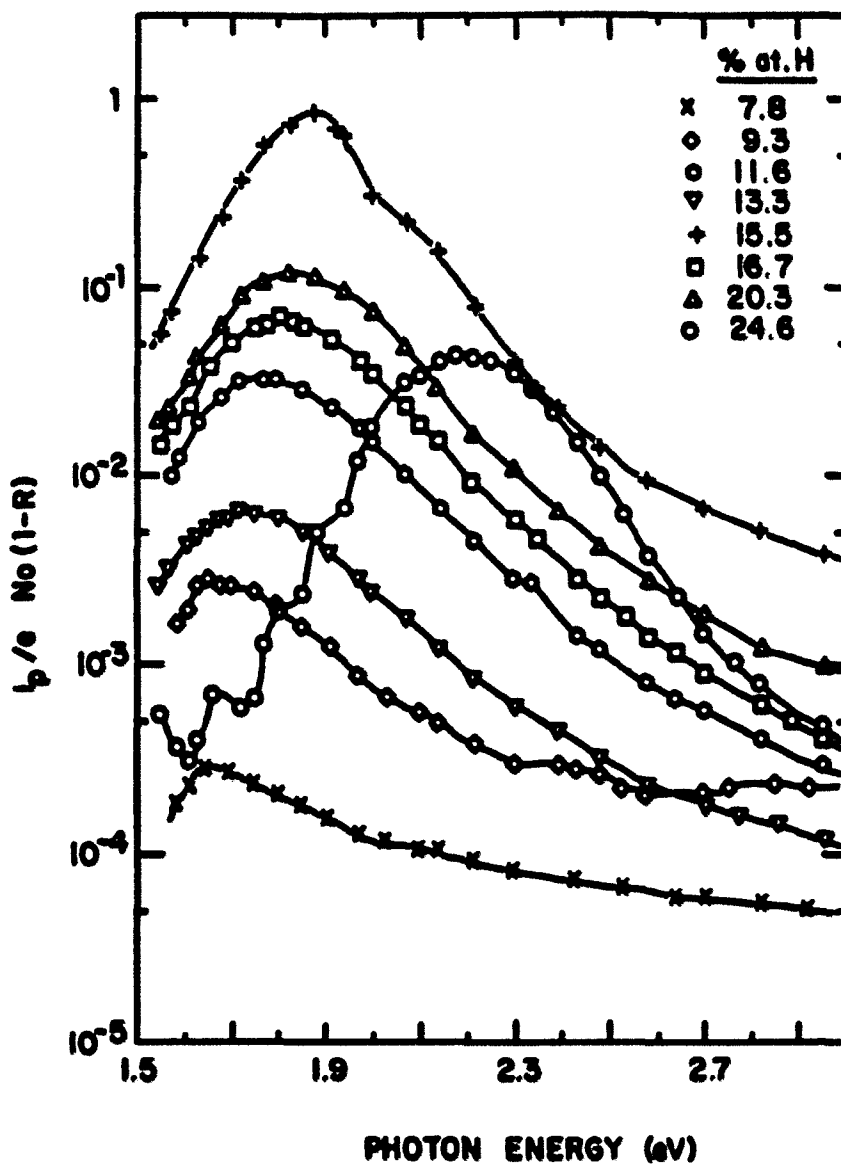


Figure 26. Spectral dependence of photo-response in a-Si:H samples with different hydrogen content. The ordinate represents the number of electrons flowing around the circuit per photon entering the films. The 7.7% at. H sample had been annealed at 250°C for 1 hour

lie near the bottom of the a-Si conduction band therefore has increasing significance at high hydrogen concentrations. If these states are the initial states for recombination, there will be an increased probability of radiationless recombination with thermalization of the high energy phonon. This may be the explanation for the decrease in the photoresponse for samples group III, i.e., with greater than 20 % at. H.

To determine the nature of the recombination centers present in the gap, it is useful to know the relation between the photocurrents and light intensity. In all room temperature experiments, it was found that the photocurrent exhibits a dependence on the photon intensity as [26]

$$i_p = kP^\delta \quad (46)$$

where k and δ are constants, while P , the photon intensity, is determined using a calibrated photomultiplier. δ is calculated from the slope of $\ln i_p$ vs $\ln P$ plot shown in Figure 27. Over the range of intensities studied, all these samples exhibit regions where δ varies from 0.70 for the film with 20 % atomic hydrogen to 1.16 for the film with 7.8 % atomic hydrogen which has been annealed at 250° C for one hour. The sample with the highest photoresponse shows $\delta = 0.9$. This reflects a monomolecular type of recombination where the electron lifetime τ varies only slightly with illumination and indicates that there is no direct

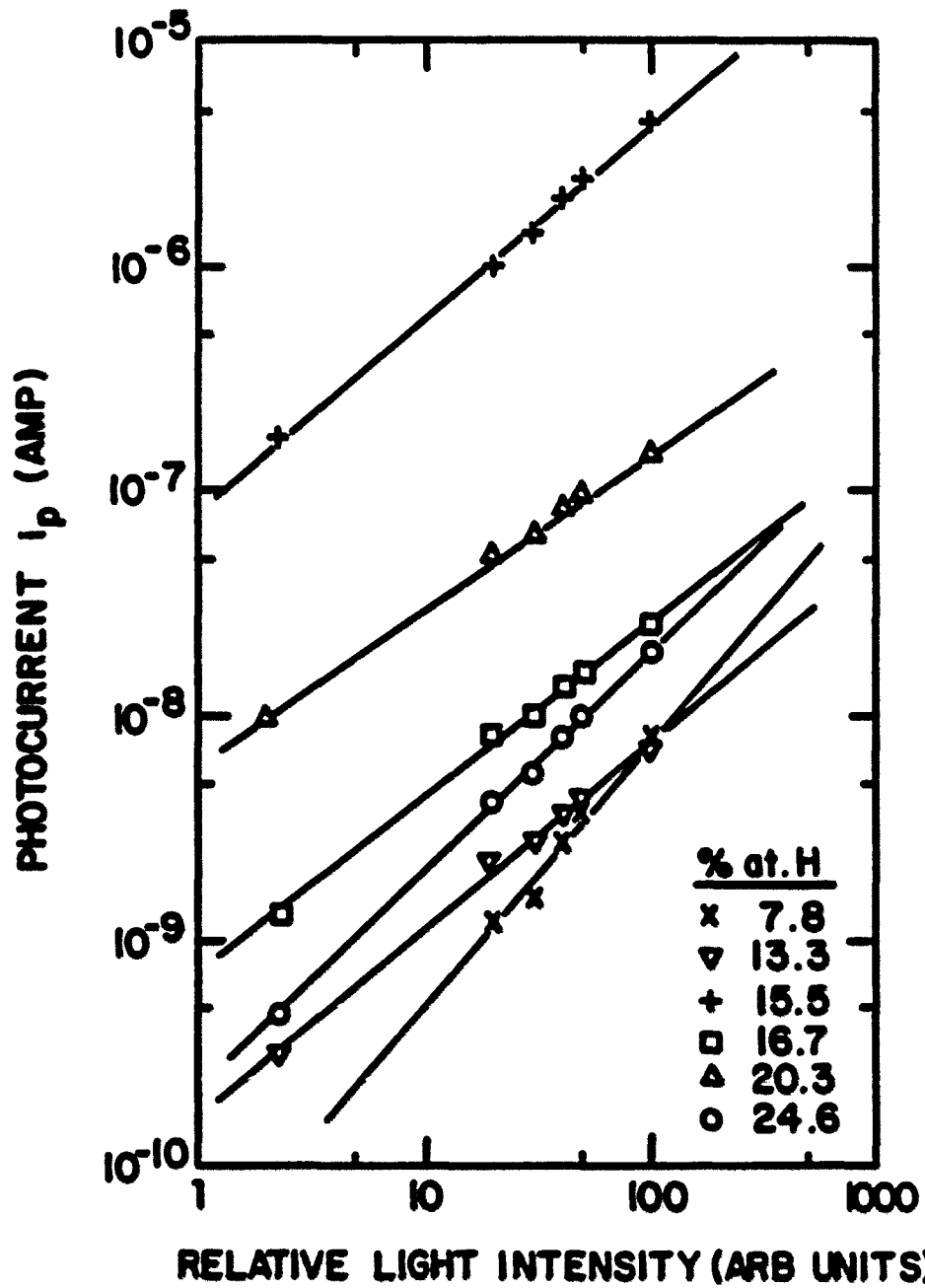


Figure 27. Photo current i_p generated by volume absorbed light as a function of light intensity for a-Si:H samples with different concentration of hydrogen x was annealed at 250°C for 1 hour

recombination [26].

The increase in photocurrent with increasing hydrogen suggests the increase of the electron lifetime τ . Changes in η or μ_n (inversely proportional to t_T) also are possible, in principle, but their effects are probably quite small. This is because a change in η would be expected to change the shape of the photoresponse spectrum [43]. Furthermore a change in μ_n is ruled out by the results of Figure 27, the photocurrent versus light intensity plot which shows that the constants δ are not the same. If only μ_n changed, then the plot would show parallel lines. For energies above band gap, η is expected to be unity, and for $\mu_n = 1 \text{ cm}^2/\text{V sec}$, the electron lifetimes for the sample with 15.5 % atomic hydrogen content are estimated to be about 10^{-5} sec.

4.4. Activation Energy

Figure 28 shows the temperature dependence of the conductivity for samples with hydrogen contents varying from 7.79 at. % to 20.30 at. %. The linearity of all plots provide well-defined activation energies, E_a , which are determined from the slope of the curves, and indicates that the electrical conduction mechanism in the samples is thermally activated. That is, transport arises from carriers excited beyond the mobility edges into nonlocalized (extended) states at the conduction band edge (E_c) [32]. The room temperature conductivity for the sample with a hydrogen content of 7.79

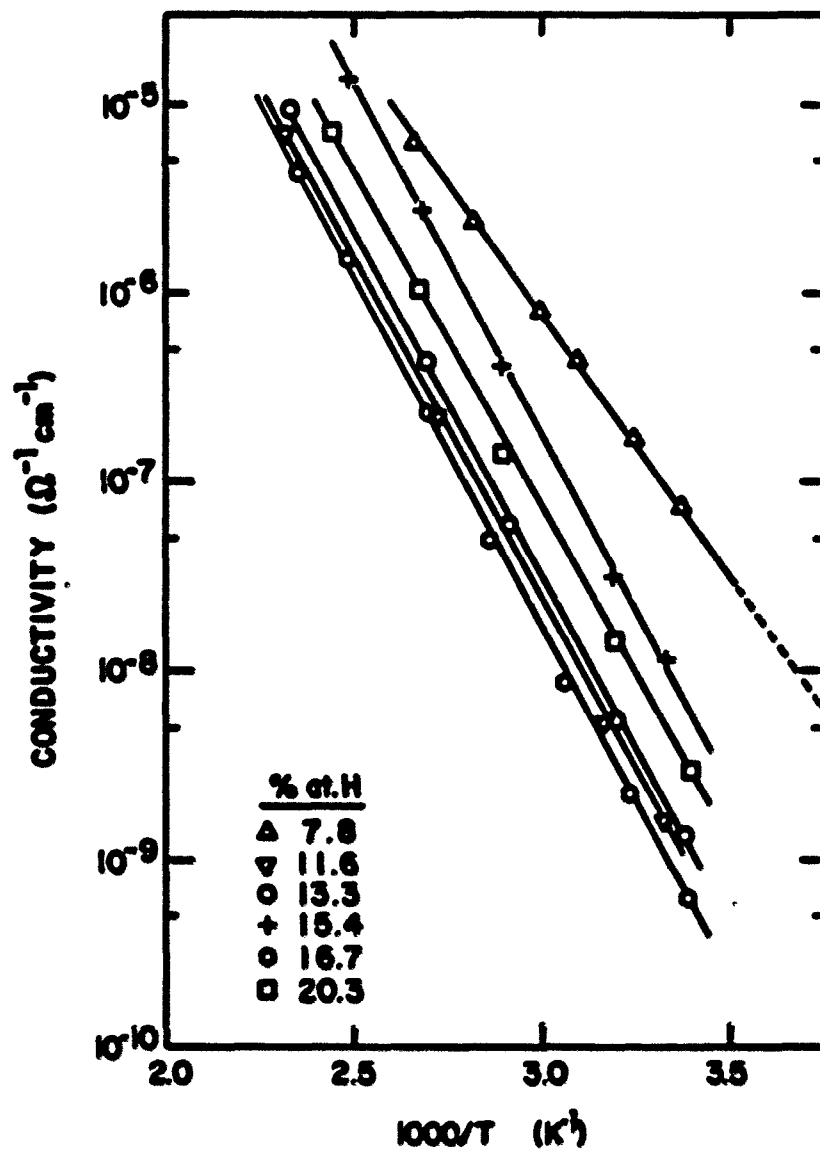


Figure 28. Temperature dependence of the conductivity for samples with hydrogen content vary from 7.8 at. % to 20.3 at. %

at. %, is the highest ($\sim 9.2 \times 10^{-8} \Omega^{-1}\text{cm}^{-1}$), while for samples with hydrogen content between 10 at. % and 20 at. % the conductivity does not scale with hydrogen content.

Figure 29 shows the variation of the conduction band edge (E_c), the Fermi energy (E_f), and the valence band edge (E_v) with hydrogen concentration (C_H). The conduction band edge is used as a reference, while the position of the valence band edge, defined as $E_c - E_g^{\text{opt}}$, is obtained from the previous section (Figure 25). The Fermi energy position, defined as $E_c - E_a$, is determined from the calculation of the activation energy in Figure 28. For the samples with C_H bigger than 10 at. %, the activation energy is practically constant (~ 0.71 eV) and drops gradually for samples with C_H less than 10%. Choosing the bottom of the conduction band as a reference is reasonable since the conduction band is not influenced by introduction of hydrogen into the amorphous silicon matrix as reported by von Roedern et al. [44]. This is in agreement with data reported by Johnson et al. [45] which indicate that the change of band gap with hydrogen content appears to be more affected by the hydrogen-induced hybridization of the Si(3p) - Si(3p) bonding levels at the top of the valence band than by any hydrogen-induced hybridization of the Si-Si antibonding levels at the bottom of the conduction band or by the presence of H-Si anti-bonding levels within the conduction band. Papaconstantopoulos and Economou [46] argue that the conduction band edge is essentially constant when introducing

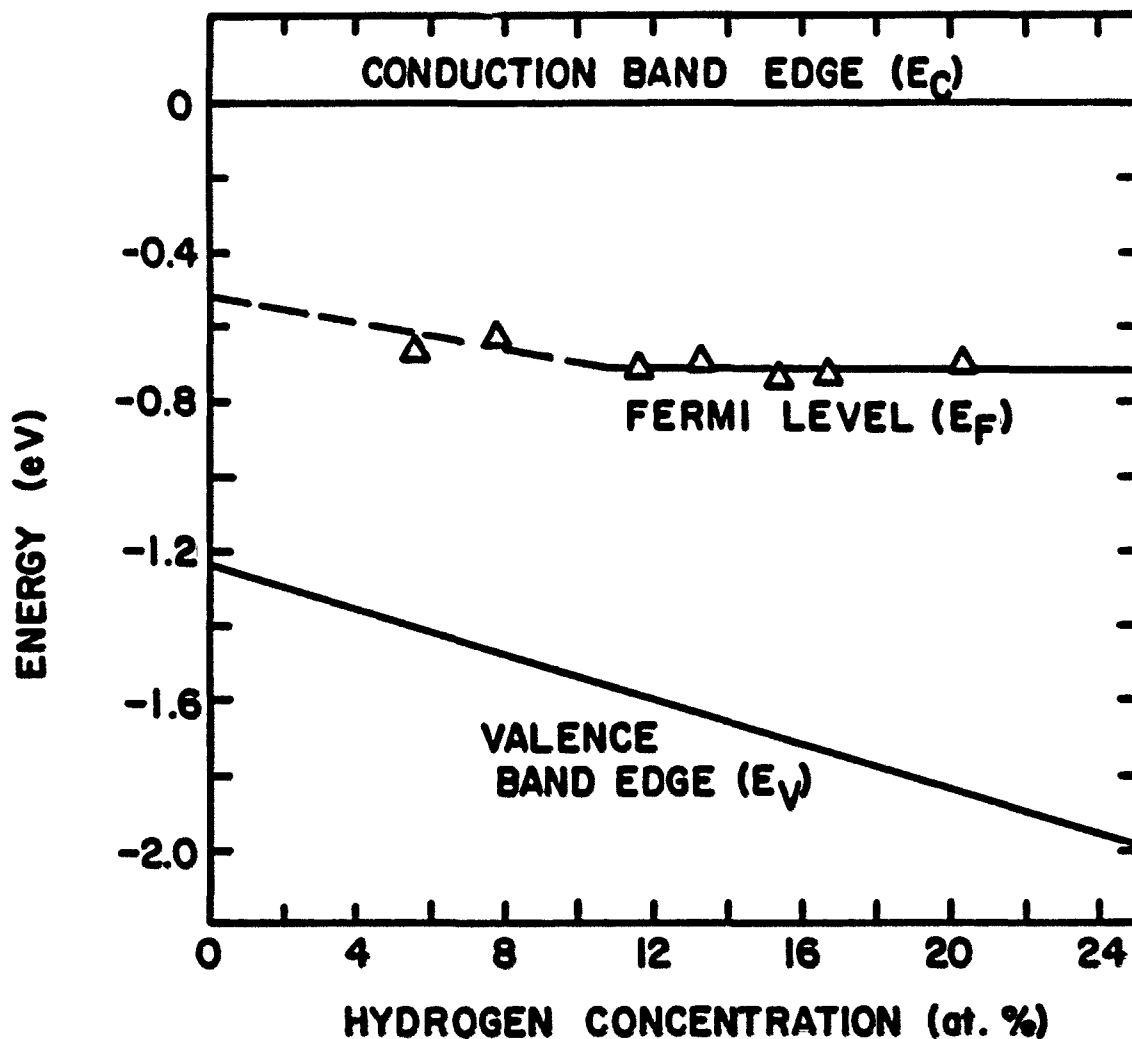


Figure 29. Variation of the conduction band edge (E_C), the Fermi level (E_F), and the valence band edge (E_V) with hydrogen concentration. The conduction band edge is used as a reference (Energy = 0). The position of the valence band edge relative to the conduction band edge is obtained from Figure 25

H into the a-Si matrix since the effect of disorder which tends to push E_c down is cancelled by the effect of a stronger Si-H bond which tends to push E_c up. All of these reports conclude that the introduction of H into a-Si network does not influence the conduction band, but reduces the valence band density of states near the band edge, and effectively widens the optical band gap. The Fermi level is rather unaffected by addition of hydrogen at higher concentration (> 10 at. %) but moves slightly closer to the conduction band edge for samples with less than 10 % at. H. Projection of the Fermi level to 0 % at. H intercepts the energy axis at ~ 0.5 eV below the conduction band edge.

The conductivity prefactor, σ_0 , in $\sigma = \sigma_0 \exp\left(-\frac{E_a}{kT}\right)$ for samples varied from 1.65×10^3 to $4.61 \times 10^4 \Omega^{-1}\text{cm}^{-1}$. The increases of σ_0 suggested the greater mobility of the electrons. These results are consistent with the values reported by Paul and Anderson for their sputtered samples [47].

4.5. Schottky Diode

Current transport mechanisms in Schottky diodes have been interpreted by two distinct theories, the diffusion theory (DT) by Schottky and the thermionic emission theory (TET) by Bethe. The DT assumes that the current flowing in a metal-semiconductor barrier is determined by drift diffusion within the space-charge region of the semiconductor, and that an

electron quasi-Fermi-level is continuous at the junction, i.e., electrons coming from the semiconductor are supposed to be in equilibrium with metal electrons. The TET, instead, assumes the current is limited by the emission of electrons over the barrier itself and that the electron quasi-Fermi-level is spatially uniform within the semiconductor space-charge region and, therefore, discontinuous at the junction. Wronski et al. [48] adopted the DT for an a-Si:H/metal diode because of the low mobility of the charge carriers in the semiconductor. In contrast, the TET was assumed by Deneuille and Brodsky in their study about influence of preparation condition on amorphous silicon Schottky diodes [49]. They argued that the current levels used were too low to allow the use of sufficiently low temperature range measurements to distinguish between the DT and the TET for the transport mechanism in these diodes. They concluded that, in their study of metal base transistor operation for a structure a-Si:H/metal/a-Si:H a TET, is more favorable [49]. Considering the above difficulties, a thermionic diffusion theory (TDT) proposed by Sze [33] which includes a drift-diffusion process taking place within the semiconductor space-charge region in series with the thermionic emission over the barrier, has been chosen as a more realistic approximation.

The room temperature forward and reverse current-voltage characteristics of two Schottky barrier diodes incorporating a-Si prepared with different hydrogen contents is shown in

Figure 30. The currents increase exponentially with forward applied bias up to a point where the bulk resistance and contact resistance begins to be comparable with the junction resistance and the currents become series-resistance limited. No saturation is observed in the reverse currents. Under reverse bias, localized states introduce a generation-recombination current component which contributes to the lack of saturation of current with increasing reverse-bias voltage [49]. Chen and Lee reported theoretical results that the lower the density of localized states, the more important the recombination currents becomes [50]. Near ideal a-Si:H Schottky diode behavior has been obtained for samples with hydrogen content near 16 at. % which have an ideality factor $\eta = 1.05$ and a rectification ratio $> 10^4$. The sample with hydrogen content of ~ 13 at. % shows a rectification ratio $> 10^3$ and an ideality factor $\eta = 1.15$. Both samples have Schottky barrier heights of about 0.9 eV. The nearly ideal diode behavior of the a-Si:H/Au Schottky diode indicates that the sample has a low density of defect centers [48]. For samples with hydrogen contents less than 6 at. % no rectification is observed. This can be largely attributed to large numbers of gap states and consequently, a thin depletion region [51]. Neglecting the effect of an oxide layer at the interface (McGill and Wilson [52] reported a 170 mV increase in going from an intimate contact to a 13 Å thick oxide) the barrier heights of some Schottky diodes with various hydrogen

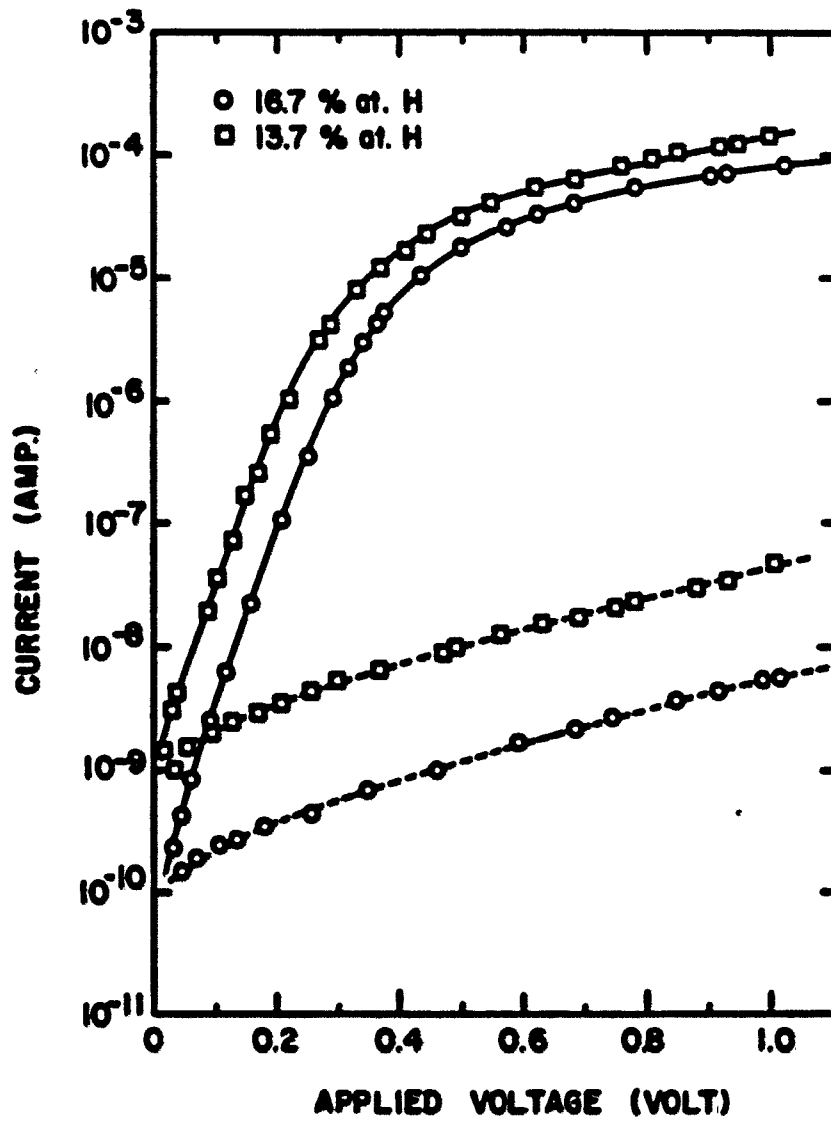


Figure 30. Current-voltage characteristics of Au/a-Si:H Schottky barriers with different hydrogen concentration

———— for forward bias

----- for reverse bias

contents are plotted against the hydrogen concentration in Figure 31. The barrier height for the sample with 7.1 % at. hydrogen is 0.79 eV, while for samples with hydrogen contents > 10 at. % it is constant at about 0.9 eV. There is a systematic relation between the changes of the barrier height, the activation energy, the density states in the band gap, and the diode quality factor. It is clear that the samples with hydrogen concentration greater than 10 at. % have a larger depletion layer and consequently, have lower densities of states as compared with the sample with hydrogen concentrations less than 8% [51]. This condition will be discussed further in Section 4.6.

To determine the extent of the oxide layer at the interface, an Auger depth profile was done using a 0.75 keV argon ion beam to sputter-etch the surface of a sample which was plated with gold. The compositional profile obtained by AES is shown in Figure 32. The profile revealed a very low oxygen concentration at the interface (less than one monolayer) proving that the assumption above is reasonable. The interdiffusion of the gold and silicon shown in the figure can be attributed to ion beam mixing of this thin gold (~ 60Å), the roughness of the sample surface, the interdiffusion really occurs as reported by many workers [8,9] or a combination of these three conditions.

A depth profile was done on a sample which had been plated with 60 Å gold and stored in the open air for 3 months.

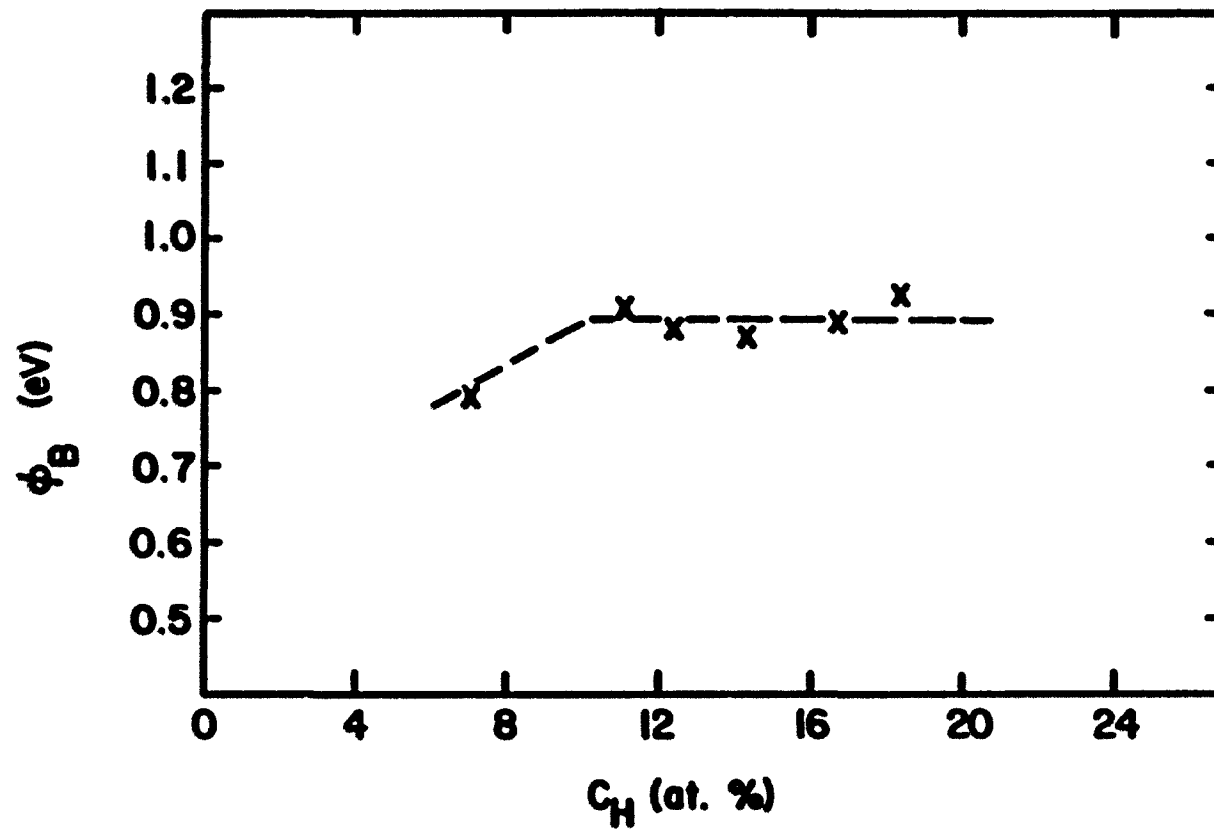


Figure 31. Schottky barrier height dependence on the hydrogen concentration

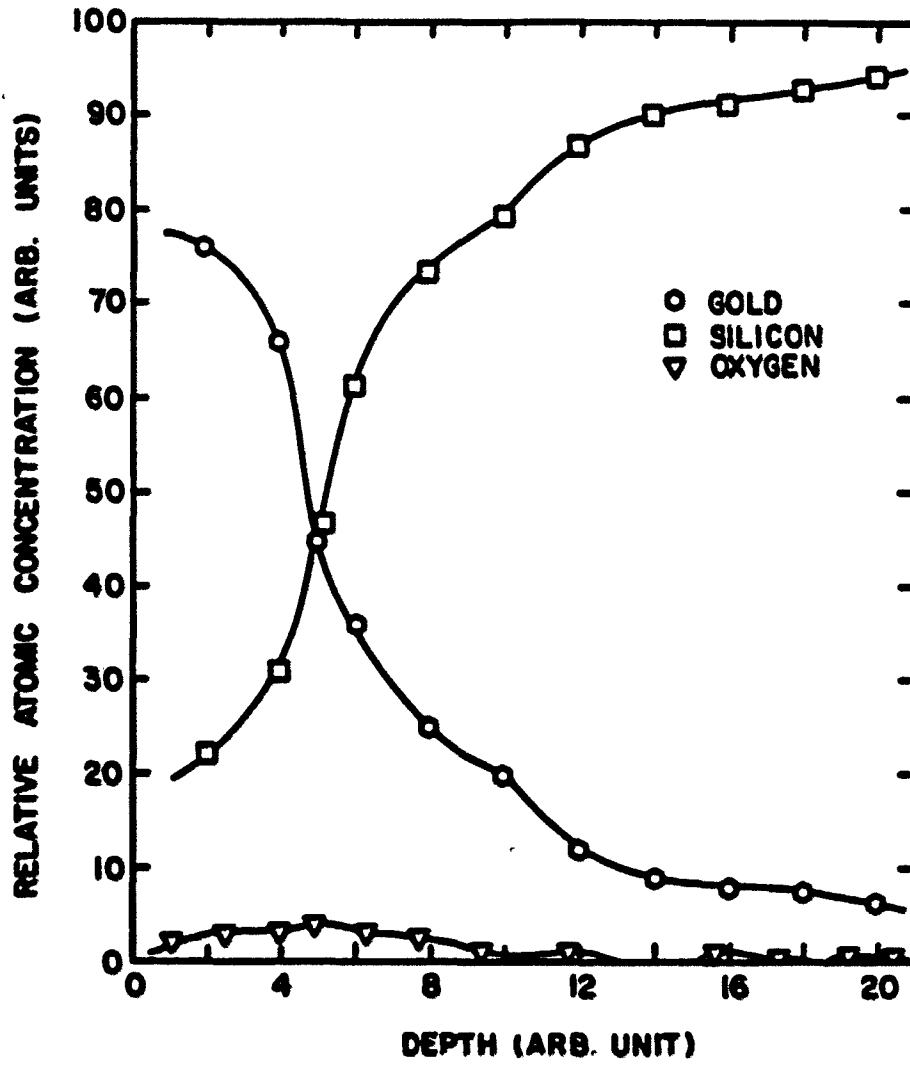


Figure 32. Auger depth profile of Au/a-Si:H Schottky diode with 0.75 keV Ar⁺ ion beam

The color of the dot diode changed from yellow (Au color) to dark brown. Figure 33 shows the Auger depth profile of the Au/a-Si:H Schottky diode. An oxygen peak appears between one Au peak at the surface and the other Au peak inside the silicon. The ratio of Si concentration to Au concentration is almost twice the previous one (see Figure 32). This is possibly the same kind of process observed by Tsai et al. [53] on their study of the aging of Au/a-Si:H diodes by annealing from 150° C to 200° C. That is, the Si diffusion into the Au layer started a nucleation of crystalline Si islands inside the Au which were randomly spaced and separated by a distance much larger than the dimensions of the Au crystallites. The c-Si islands grow into lateral dendritic crystallites which attract oxygen and/or water from the air and form Si-O containing species near the interface. It appears that crystalline Si oxidizes much faster than a-Si:H, since Auger profiles of the surface of the sample which is not covered with gold shows very little oxygen.

4.6. Space Charge Limited Current Measurements

Space Charge Limited Current (SCLC) flow has been investigated as a function of applied potential on Schottky diodes of amorphous silicon films prepared by r.f. sputtering technique. The method has been accepted as useful to study energetic and spatial profiles of traps for current carriers in the semiconductor [21]. The measurements were made on a number of

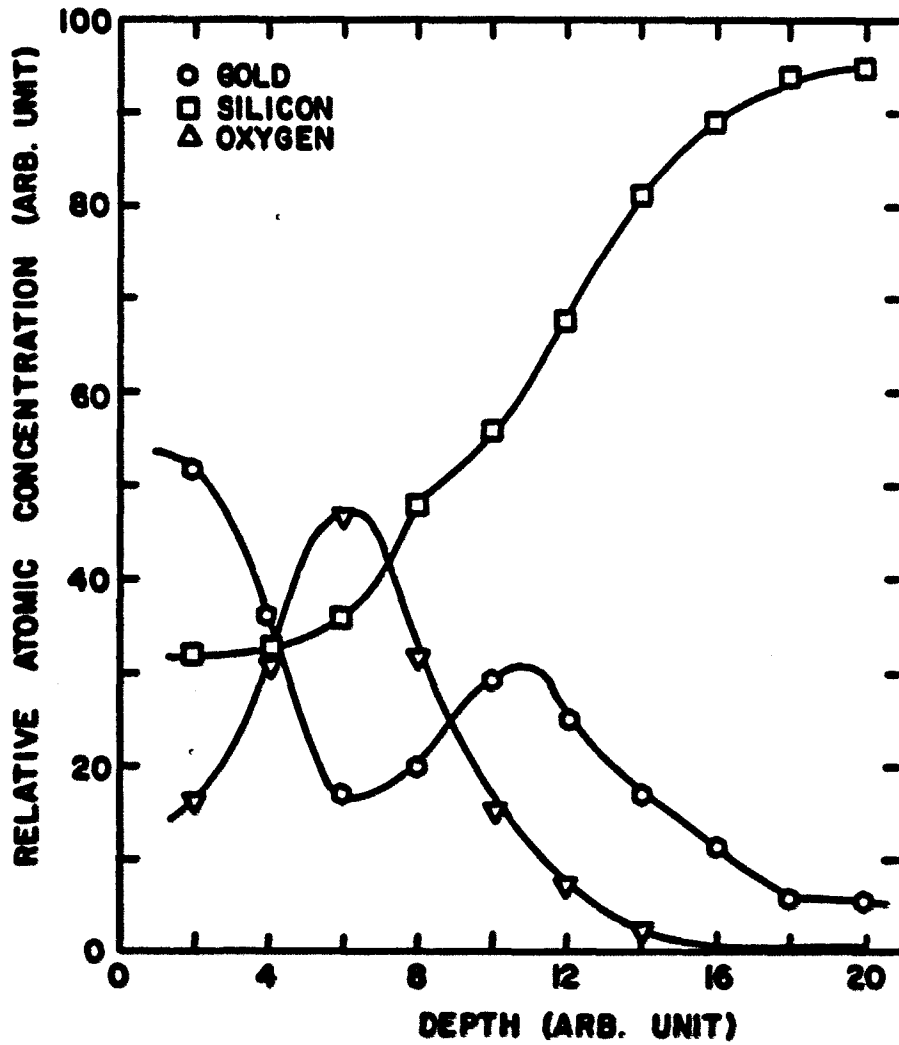


Figure 33. Auger depth profile of Au/a-Si:H Schottky diode with 0.75 keV Ar⁺ ion beam. The diode has been in the open air for 3 months

sputtered samples prepared in this laboratory with varying hydrogen concentrations from 5.7 to 19.1 at. %.

It has been reported theoretically by Rose [20] that the presence of traps in the band gap distorts the shape of the current-voltage curve for a metal-insulator-metal model (at least one of the two electrodes must take ohmic contact to the insulator), from an ideal square law to a much higher power dependence on voltage, and the particular shape can be used to determine the energy distribution of traps. This idea is adopted and theoretically adjusted for the purpose of calculating the density of states in the band gap [19] as discussed in Chapter 3. The assumption that the diffusion current is neglected places some limitation on the sample thickness, especially with the Schottky diode configuration, which has diffusion currents dominate at the barrier and the injecting contact. To solve the problem, four samples were made with the same nominal deposition parameters, but with varying thickness from 0.60 μm to 3.0 μm . They were expected to have the same electrical properties and hydrogen concentration (~ 12.3 at. %), despite minor variations due to the uncontrolled parameters such as cleanliness of the internal surfaces of the sputtering apparatus, target, and substrate surface.

Figure 34 shows the log current density-log voltage ($\log J - \log V$) characteristics of the 4 diodes as a function of thickness. The 1.38 μm thick sample has about the same

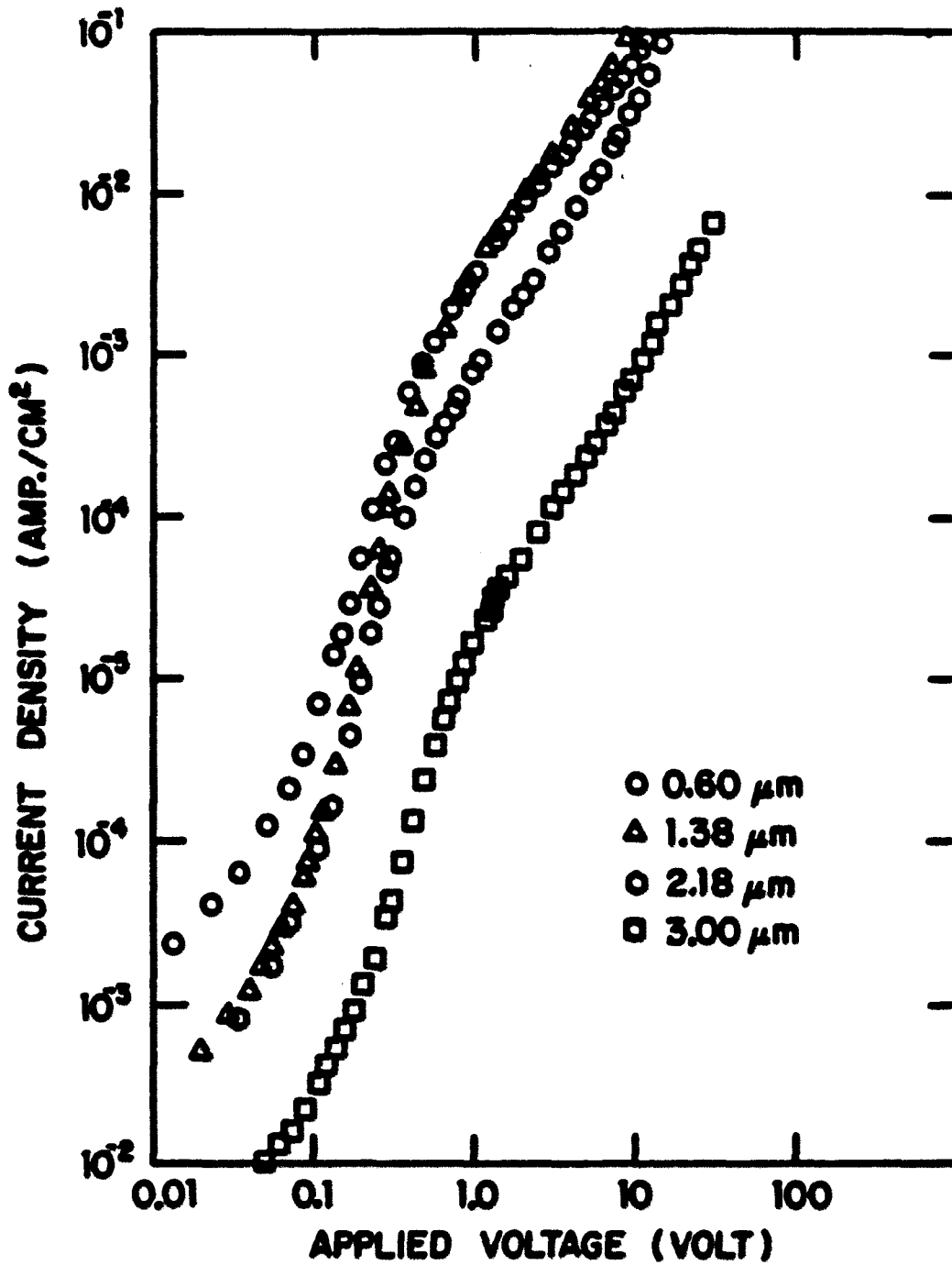


Figure 34. Log J - log V characteristics for samples which were fabricated under nominally the same parameters

current density with the 2.18 μm thick sample at low voltage while at higher voltages it approaches values obtained for the 0.60 μm thick sample. For the 3.0 μm thick sample, the current density is about one order smaller than for the 2.18 μm thick one. No direct conclusion can be obtained from the $\log J - \log V$ behavior of all these samples.

Using Equation 20, the $\log J - \log V$ characteristics were analyzed to derive the density of states distribution $N(E)$ from the Fermi level, E_F , near midgap upward in energy toward the conduction band. The range of energy probed was between 0.73 and 0.51 eV below E_C . Results of the calculations are shown in Figure 35 where the density of states is plotted as a function of energy measured from the bottom the conduction band. The 0.60 μm thick sample shows some fluctuation of the density of states about $7 \times 10^{15} \text{ cm}^{-3} \text{ eV}^{-1}$ at energies near the Fermi level. The thicker sample (1.38 μm) shows a "soft" oscillation and density of states near $1.5 \times 10^{15} \text{ cm}^{-3} \text{ eV}^{-1}$. For the 2.18 and 3.0 μm thick samples the densities of states at the Fermi level are about 5×10^{14} and $6.5 \times 10^{14} \text{ cm}^{-3} \text{ eV}^{-1}$, respectively. The higher density of states for thinner samples may be due to the diffusion currents which cannot be neglected for thin samples [19] or the influence of surface states. It was common thinking in the early work on amorphous semiconductors that the thickness-dependent effects were negligible because the large density of gap states screened the surface effects. However, For a-Si:H with considerably

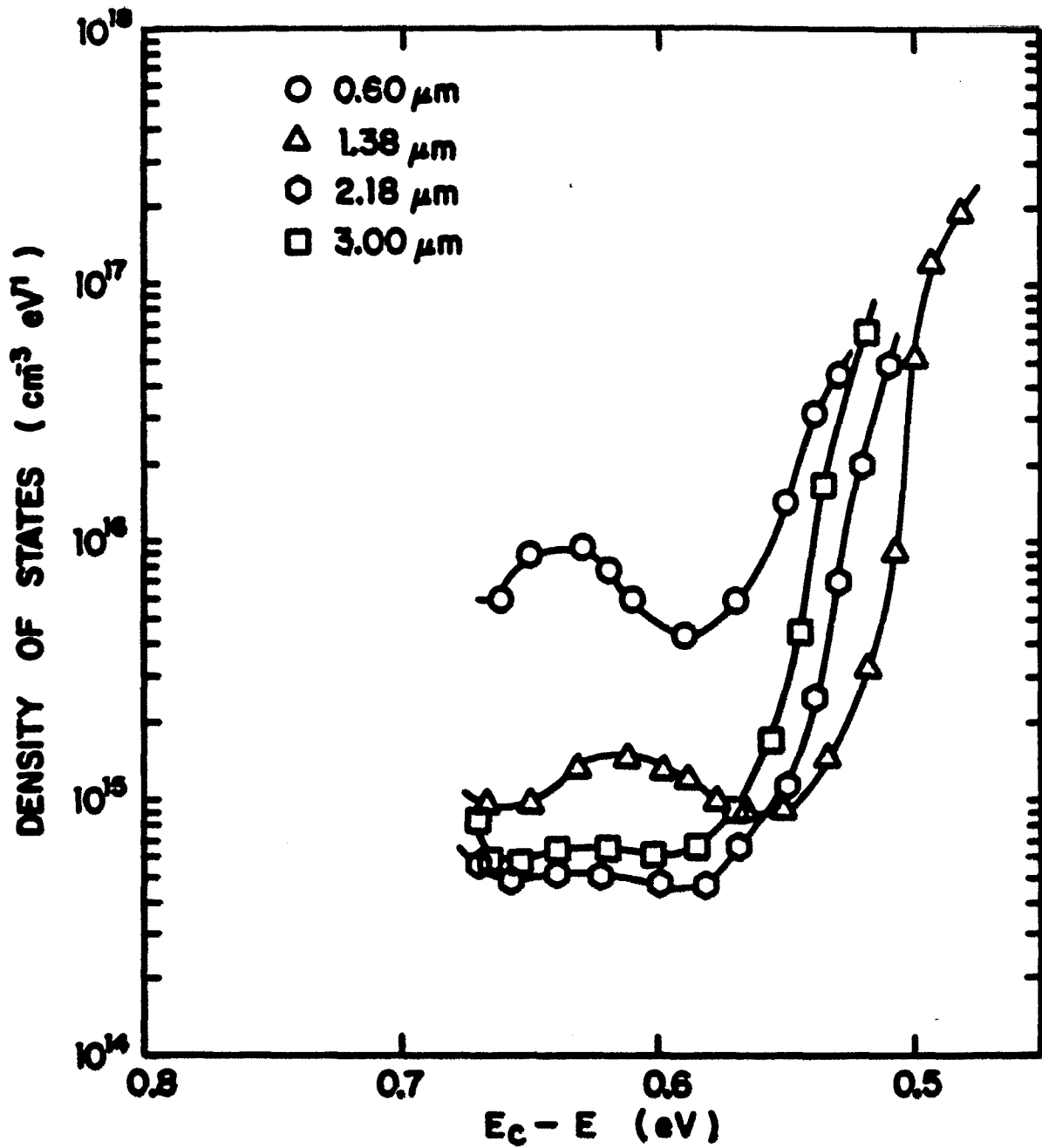


Figure 35. Density of states distribution for samples with hydrogen concentration 12.3 at. %

lower gap state densities (less than $10^{16} \text{ eV}^{-1} \text{ cm}^{-3}$), however, it is not surprising to see surface and thickness effects [54]. In all figures above, it is clear that the Fermi level of the sample is simply the lowest energy cut-off of each data set.

The third derivative of $\log V$ with respect to $\log J$ used in calculation of the density of states (Chapter 3) can often prove overly sensitive to inaccuracies in the data. To test how large the influence of the third derivative is on the whole calculation, the density of states of sample S58 (12.3 at. H) was calculated for the second time with "new third derivative data" which were twice the real values, i.e., $c_{\text{new}} =$

$2 \frac{d^3 \ln V}{d \ln J^3}$. The result of both calculations are shown in Figure

36. There is no significant difference between them, which means the calculation is insensitive to errors in the third derivative.

Figure 37 shows the $\log J$ versus $\log V$ for samples with different hydrogen concentrations. The samples have various thicknesses from 2.5 μm to 3.3 μm and hydrogen concentrations from 5.6 at. % to 19.1 at. %. The samples with hydrogen concentrations of 9.8, 14.3 and 16.7 at. % have almost the same currents under 1.0 volt applied voltage and the sample with 9.8 at. % becomes more resistive for applied voltage greater than 1.0 volt. The samples with hydrogen concentrations of 12.3 and 19.1 at. % are much less conductive

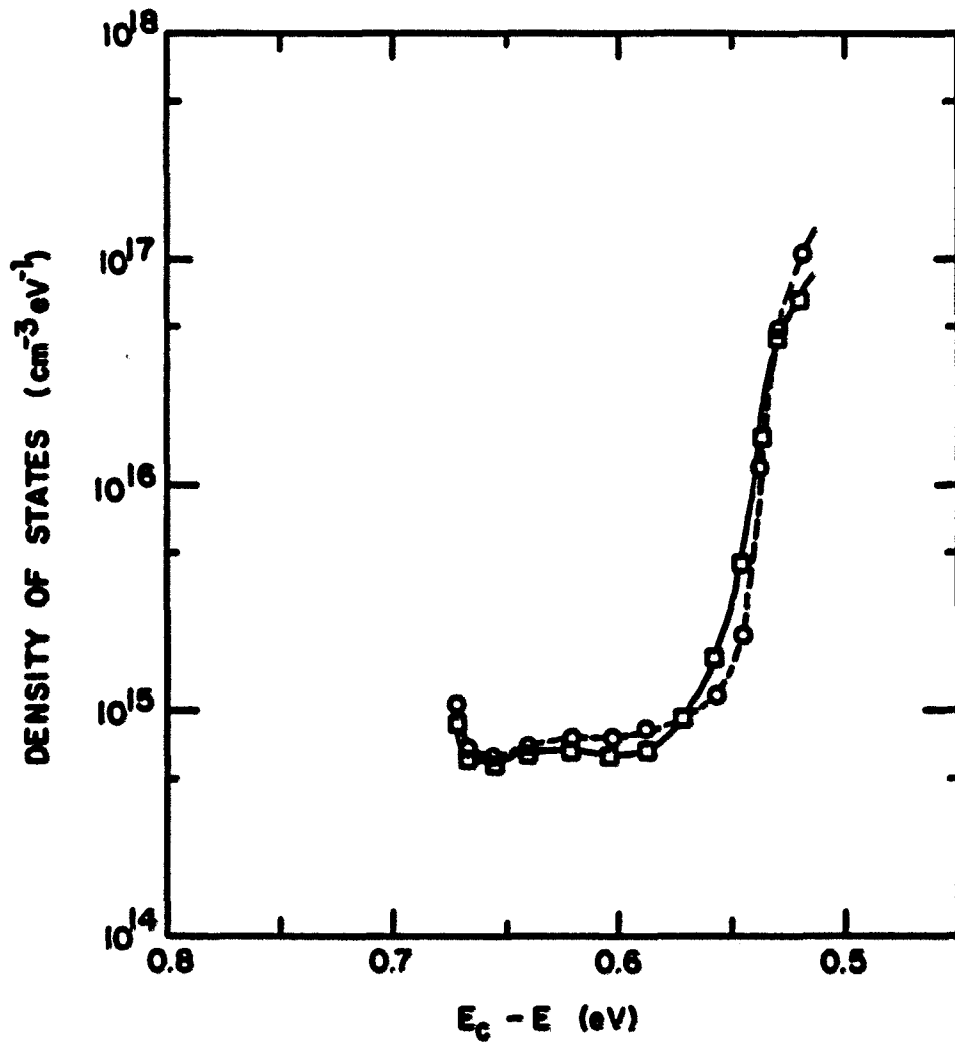


Figure 36. The density of states distribution for sample S 58

— for DOS with the calculated $\frac{d^3 \ln v}{d \ln J^3}$

--- for DOS with $c_{\text{new}} = 2 \times \frac{d^3 \ln v}{d \ln J^3}$

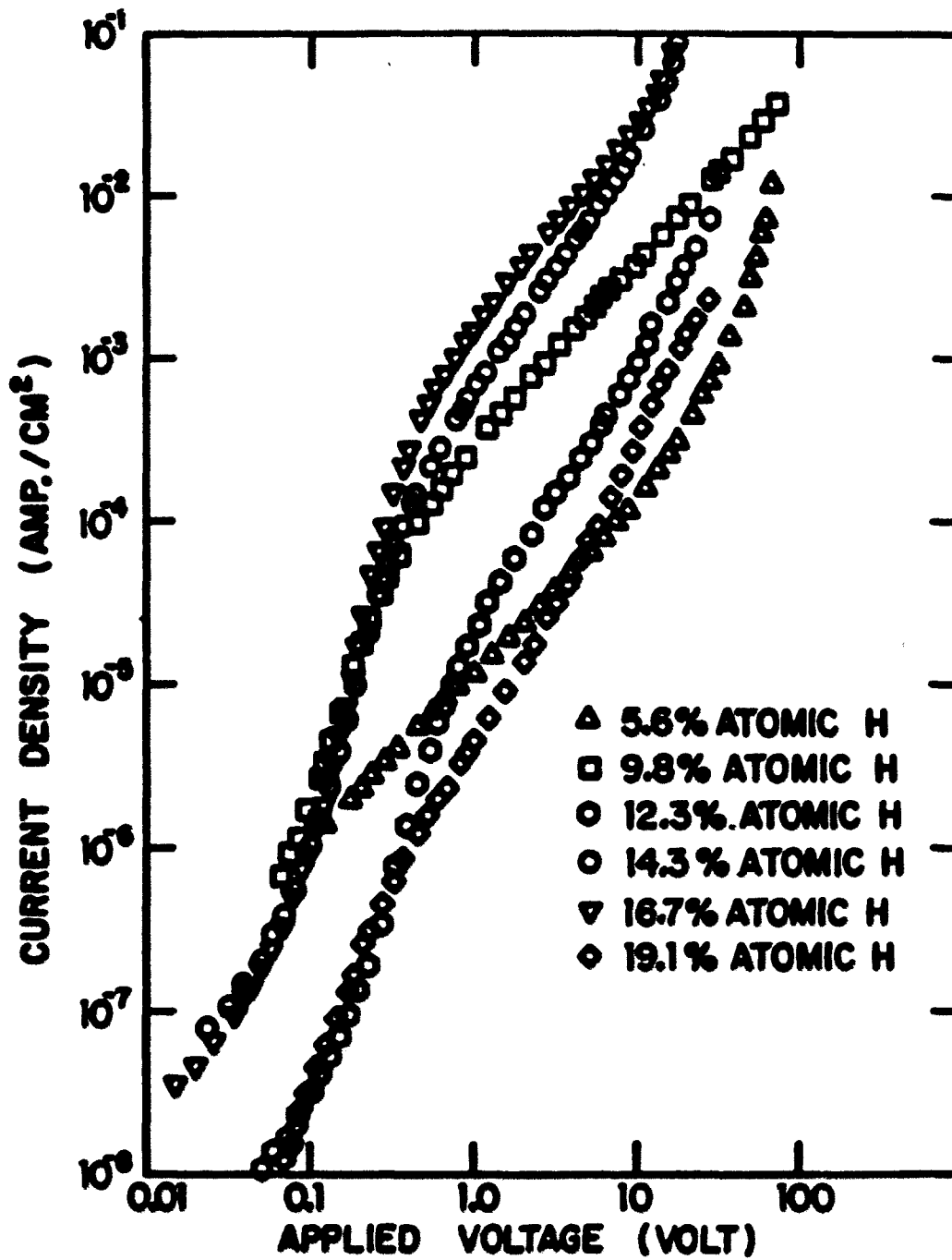


Figure 37. Log J - log V characteristics for samples with hydrogen content vary from 5.6 at. % to 19.1 at. %

than the previous three. For samples with 5.6 % at. H, the current increase as fast as the sample with 14.3 % at. H, then becomes much more resistive until the voltage reaches 10 volts before the current starts increasing very rapidly. The calculation results of the DOS for the samples with hydrogen content varied from 5.6 to 19.1 at. % are shown in Figure 38. For the sample with 5.6 % at. H the DOS is $1.2 \times 10^{17} \text{ cm}^{-3} \text{ eV}^{-1}$, about 2 order greater than the rest of them. In the figure, the Fermi levels of the samples with $C_H > 10$ at. % are assumed constant at 0.70 eV below E_c , neglecting the fluctuation of ± 0.03 eV around the pinned Fermi level. This is a reasonable assumption considering the discussion in Section 4.4.

The SCLC characteristics collectively display a rather structureless $N(E)$ around Fermi level, nearly constant in energy over most of the energy range probed and increase at a fairly rapid rate about energy 0.60 eV then show tendency to saturate at energy 0.55 eV below E_c , implying a peak in the density of states at this energy. Using the average value of $N(E)$ above E_p as a parameter characterizing the density of states around Fermi level of each sample, one can draw a curve of density of states versus hydrogen concentration as shown in Figure 39. The density of states decrease exponentially with increasing hydrogen content for samples in Group I, almost constant for samples Group II, and same tendency to increase at hydrogen concentration greater than 20 at. % (Group III).

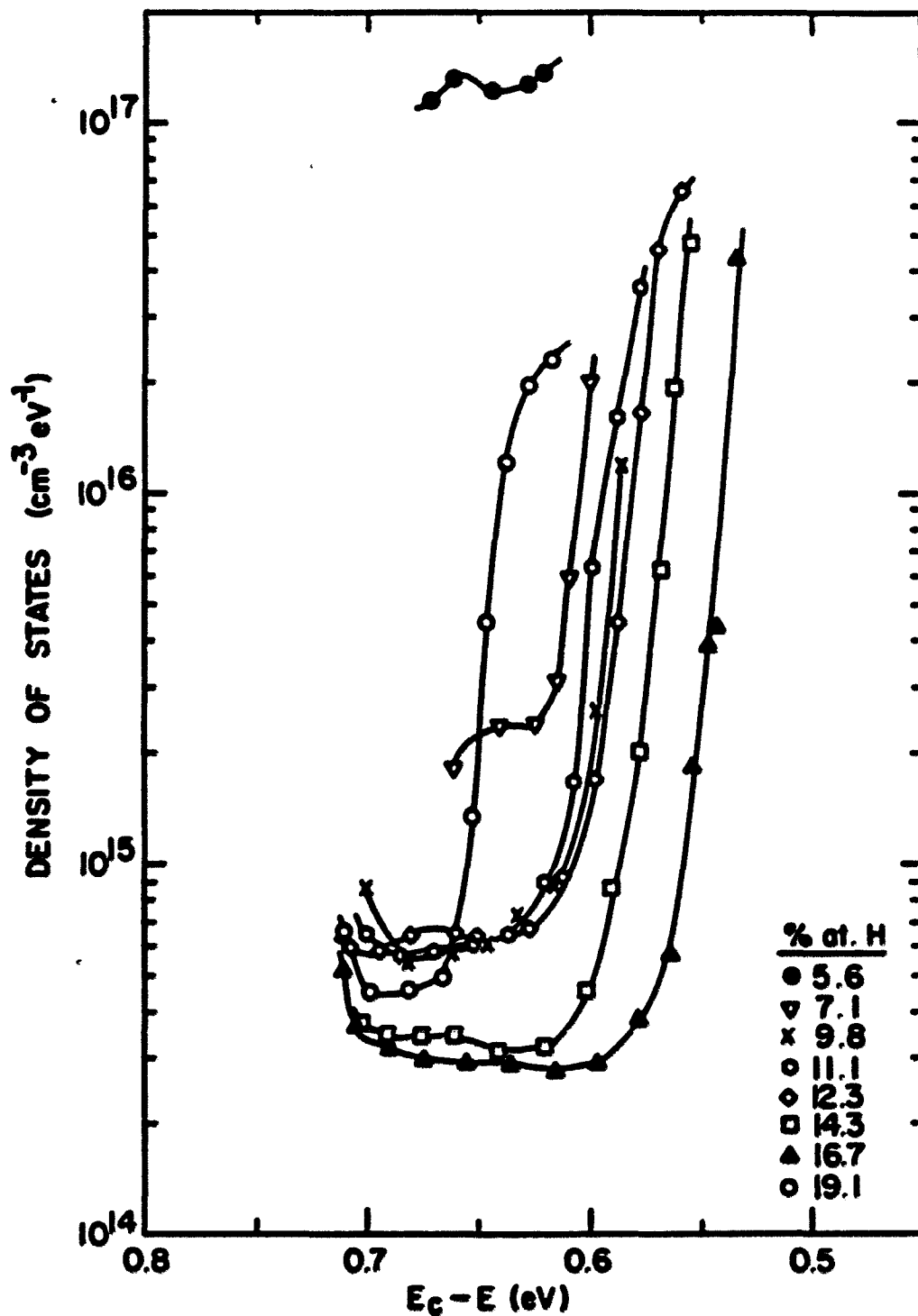


Figure 38. Experimentally determined density of states for samples with hydrogen contents between 5.6 to 19.1 at. % obtained from SCLC

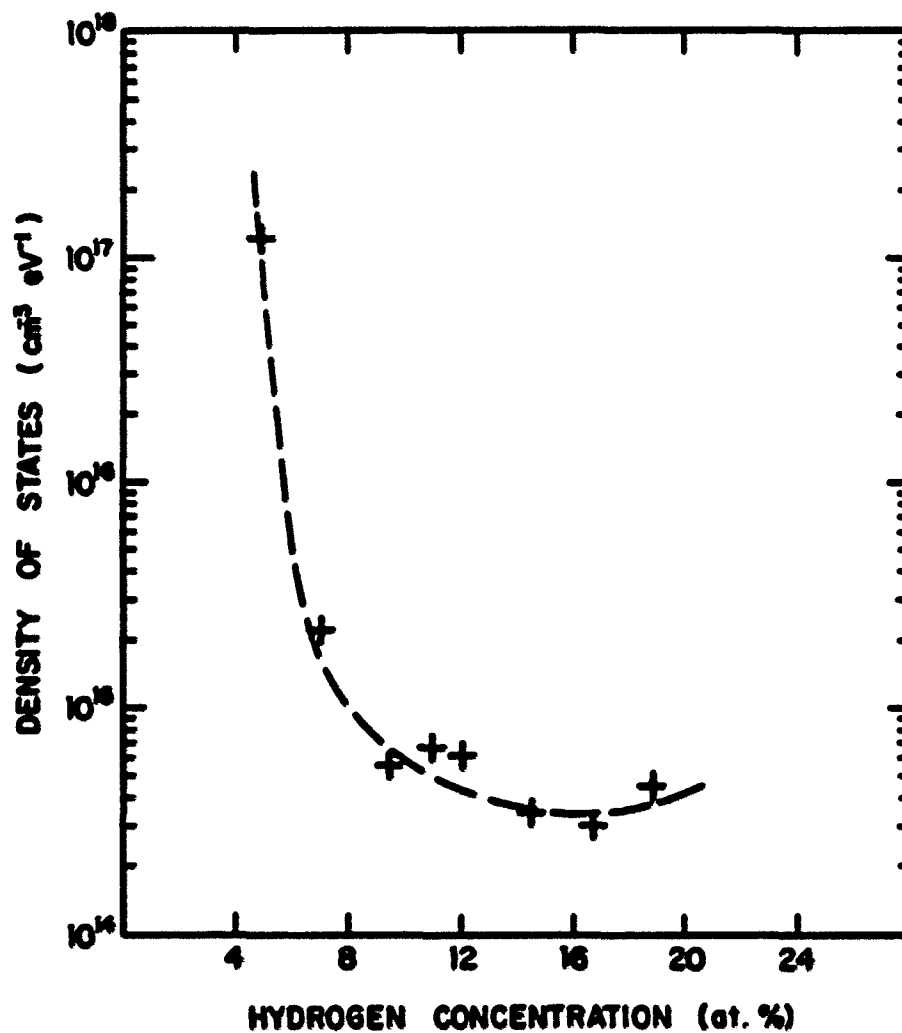


Figure 39. Density of gap states as a function of hydrogen concentration. DOS drops exponentially for C_H less than 10 at. %

Qualitatively, the dependence of the density of state on the hydrogen concentration can be explained as follows [55]. The addition of the hydrogen into the a-Si network consisting of Si-Si bonds will create Si-H bonds which relieve local strain due to the Si atoms being bonded with other Si atoms in accordance with the rigid tetrahedral configuration. Since the Si-H bond (1.48 Å) is shorter than the Si-Si bond (2.35 Å) [45], the various units described above can construct an amorphous (non-crystalline) network without a distortion and/or disruption of the unit which can create defect states in the band gap or dangling bonds. The H-containing tetrahedral units can be packed differently than the $\text{Si}(\text{Si}_4)$ units and the non-crystalline solid can have a high degree of short range order and have a low density of states in the band gap. The lower density states of the samples has been implied also from the previous section where the low conductivity of the sample and the high photoresponse are reported. When not enough hydrogen is present in the a-Si matrix, the flexibility of the non-crystalline network decreased, the SRO is disrupted, and the conductivity increase as discussed in Section 4.4.

Tiedje et al. [56] in their theoretical results indicate that the dangling bonds in the a-Si network are passivated by hydrogen atoms such that the DOS decreases exponentially with increasing H_2 partial pressure during preparation. On the other hand, the hydrogen content of the sample is linearly

dependent on the H_2 pressure, provided the hydrogen partial pressure is low [57]. Thus, the DOS will decrease exponentially also with the increasing hydrogen content for sample with low hydrogen concentration. This is in agreement with the result reported here. Based on the above argument, it is suggested in this thesis that about 7 % atomic hydrogen is needed before all dangling bonds are saturated. The addition of more hydrogen is likely to modify the a-Si network and increase the band gap (predicting a maximum attainable gap of ~ 3.0 eV [58]), or maybe associated with residual impurities whose presence is revealed when most of the dangling bond-related states are compensated by H-incorporation [59]. The trend for DOS to increase for C_H greater than 20 at. % may be assigned to new defect states which are induced by excess hydrogen atoms.

Since the optical band gap, E_g^{opt} , is linearly dependent on the hydrogen concentration (see Section 4.2), it is expected that the density of states versus the optical band gap curve shown in Figure 40 has about the same form as the curve in Figure 39.

X-ray diffraction studies on the samples were done to verify the fact that the films are amorphous. No peak which could be assigned to the crystallization of the samples was observed on the x-ray diffraction pattern.

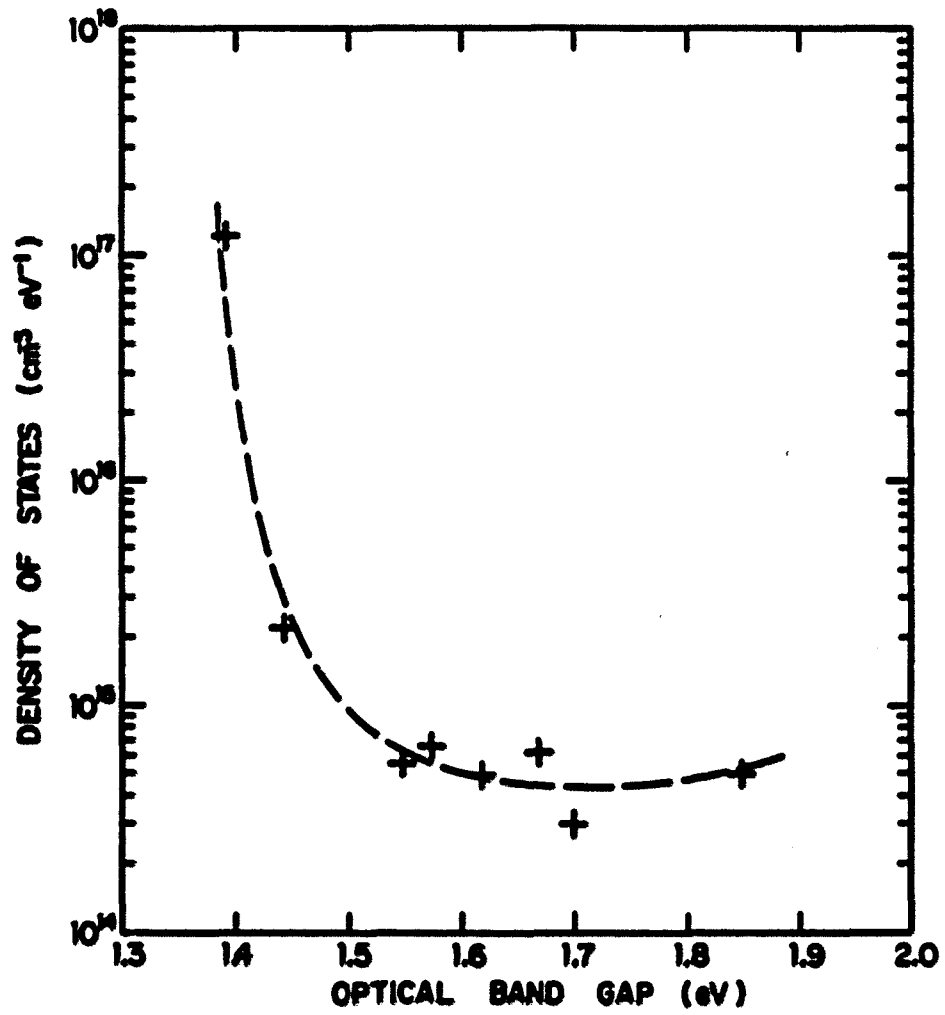


Figure 40. Density of gap states as a function of optical band gap

5. SUMMARY AND CONCLUSION

High quality a-Si:H materials, with properties close to ideal theoretical values (narrowness of the band tail and the lowness of the density of states) [60], has been obtained by r.f. sputter deposition methods in an argon and hydrogen atmosphere. The deposition conditions for the films are the principal factors determining the samples' electrical properties. The main deposition parameters are the partial pressures of the argon and hydrogen, the pumping speed (~ 11 sccm), the substrate temperature ($\sim 200^\circ$ C), the distance between the target and the substrate, and the r.f. generator power used (~ 600 watts). In addition to these rather well-controlled parameters, there are other less well controlled parameters such as cleanliness of the internal surfaces of the sputtering apparatus, target, and substrate as well as the substrate cleaning procedure, which have considerable influence on the detailed electronic properties of the sputtered films. Use of molybdenum deposited on glass as a back contact, periodically cleaning the sputtering apparatus, and careful set up of the controllable parameters make it possible to fabricate samples with reproducible properties. The hydrogen concentration in the a-Si films, the main variable for producing a good sample, is easily controlled with accuracy less than 2 at. % by adjusting the H_2 partial pressure while sputtering.

The IR vibrational absorption spectra of a-Si:H films with hydrogen content less than 20 at. % display only a single peak at 2000 cm^{-1} , attributed to SiH stretch vibrations (distributed phase). This peak shifts to 2090 cm^{-1} for samples with hydrogen content greater than 20 at. %, which is assigned to other conditions of SiH stretch vibration (cluster phase). The samples do not show the inferior electric properties reported by Oguz et al. [61]. The optimum values obtained for the samples are comparable to the results for glow discharge produced samples. Hydrogen concentrations of the samples were determined from the integrated infrared absorption near 640 cm^{-1} band.

The optical band gaps of the a-Si:H samples depend linearly on the hydrogen concentration in the range of 0 to 30 at. %. The a-Si samples without hydrogen has optical band gaps of about 1.23 eV. The E_g^{opt} versus C_H plot has a slope of about 0.03 eV/at. % H.

The samples with hydrogen concentrations greater than 10 at. % show good photoconductivity comparable with glow discharge produced films. For samples with hydrogen concentrations near 15.5 at. %, the photoresponse is almost one electron-hole pair for an electric field $\sim 8\text{ kV/cm}$.

The room temperature conductivity increases with decreasing C_H for low hydrogen content samples but becomes insensitive to composition at higher concentrations. Increasing the hydrogen concentration in a-Si:H does not

change the position of the conduction band but lowers the position of the valence band edge. The thermal activation energy is constant for $C_H > 10$ at. % and decreases slightly for lower C_H .

Nearly ideal Au/a-Si:H Schottky diodes have been obtained by improving the quality of the a-Si:H film and ohmic back contact. Plating a glass with molybdenum as a substrate and depositing ~ 300 Å of highly phosphorous doped a-Si:H before deposition of the undoped a-Si:H layer provides a very good ohmic contact at the back side of the Schottky diode. The rectification ratio ($\frac{I_{1V}}{I_{-1V}}$) is greater than 10^4 at room temperature. Molybdenum gives a better ohmic contact than stainless steel. Auger depth profiles on the gold surface of the Schottky diodes indicate very little trace of oxygen (less than one monolayer). The Au/a-Si:H Schottky diode barrier height is ~ 0.9 eV and the diode quality factor is 1.05 for samples produced under optimum conditions.

Undoubtedly, the hydrogen role is one of the most important in an electronic description of sputtered a-Si:H. A concomitant increase of the optical gap, steepening of the absorption edge, the onset of significant photoconductivity, a changeover of the transport mechanism from gap state hopping into activated transport in the conduction band all occur with the introduction of hydrogen into amorphous silicon. Therefore, it would be expected that the SCLC measurements would

reflect a reduction in the gap state densities with hydrogen incorporation.

The SCLC measurements depend on the sample thicknesses not only because carrier diffusion requires a thick sample, but also because of the low density of gap states, surface states also contribute. The optimum thickness for $N(E)$ measurements is about 2 μm or more for samples with density states of the order of $10^{14} \text{ cm}^{-3} \text{ eV}^{-1}$ around the Fermi level.

For samples with thicknesses greater than 2 μm , the DOS decreases exponentially with increasing hydrogen content and becomes almost constant for $C_{\text{H}} > 10$ at. %. There is the tendency for the DOS to increase at hydrogen concentrations greater than 20 at. %. The results in this thesis suggest that the best a-Si:H is obtained with $C_{\text{H}} \sim 15$ at. %. This value is very close to the hydrogen concentration (13 at. %) where the amount of clustered phase is the same as the distributed phase [62]. A hydrogen content of about 15 at. % is typically reported for device-quality material. It is suggested here that all dangling bonds are passivated with about 7 % at. H, and that the number is very much the same for the distributed phase (6.8 at. %), regardless of the overall H content of the film as reported by Jeffrey and Lowry [62].

The overall conclusion of the work is that films of a-Si:H, carefully prepared by r.f. sputtering, have very low density of gap states ($\sim 3 \times 10^{14} \text{ cm}^{-3} \text{ eV}^{-1}$) and for hydrogen

concentrations near 15 at. % have the lowest densities reported for an amorphous material.

6. REFERENCES

1. H. R. Shanks, F. R. Jeffrey, and M. E. Lowry, the 9th International Conference on Liquid and Amorphous Semiconductors, Grenoble, France, July 1981.
2. F. R. Jeffrey, The Effect of Hydrogen Content on Reactively Sputtered Amorphous Silicon Film, Ph.D. dissertation, Iowa State University, Ames, Iowa, 1979.
3. M. H. Brodsky and D. Kaplan, J. Non-Crystalline Solids 32, 431 (1979).
4. T. D. Moustakas, D. A. Anderson, and W. Paul, Solid State Commun. 23, 155 (1977).
5. T. D. Moustakas, J. Electron. Mater. 8, 391 (1979).
6. W. E. Spear, Adv. Phys. 26, 811 (1977).
7. W. T. Pawlewicz, J. Appl. Phys. 49, 5595 (1978).
8. T. D. Moustakas and R. Friedman, Appl. Phys. Lett. 49, 515 (1982).
9. E. C. Freeman and W. Paul, Phys. Rev. B 18, 4288, (1978).
10. M. H. Brodsky, M. Cardona, and J. J. Cuomo, Phys. Rev. B 16, 3556 (1977).
11. J. C. Knights, G. Lucovsky, and R. J. Nemanich, Phil. Mag. 37, 467 (1978).
12. W. Paul, Solid State Commun. 34, 283 (1980).
13. K. D. Mackenzie, P. G. Le Comber, and W. E. Spear, Phil. Mag. 46, 377 (1982).
14. A. Madan and P. G. Le Comber, Proceeding of Seventh International Conference on Liquid and Amorphous Semiconductors, edited by W. E. Spear (Edinburg, 1977) p. 377.
15. W. E. Spear, P. G. Le Comber and A. J. Snell, Phil. Mag. 38, 303 (1978).
16. D. V. Lang, J. D. Cohen, J. P. Harbison, Phys. Rev. B 25, 5285 (1982).

17. G. H. Döhler and Hirose, *Proceeding of the Seventh International Conference of Liquid and Amorphous Semiconductors*, edited by W. E. Spear (Edinburg, 1977) p. 372.
18. P. Viktorovitch and D. Jousse, *J. Non-Crystalline Solids* 35/36, 569 (1980).
19. R. L. Weisfield, *J. Appl. Phys.* 54, 6401 (1983).
20. A. Rose, *Phys. Rev. Phys.* 54, 6401 (1983).
21. W. den Boer, *J. de Physique* 42, C4-451 (1981).
22. E. Bhattacharja, S. Guha, K. V. Krishna, and D. R. Bapat, *J. Appl. Phys.* 53, 6285 (1982).
23. B. Chapman, *Glow Discharge Processes* (John Wiley & Sons, New York, 1980).
24. J. I. Pankove, *Optical Processes in Semiconductors* (Dover Publications, New York, 1975).
25. J. E. Stewart, *Infrared Spectroscopy* (Marcel Dekker, New York, 1970).
26. P. J. Zanzucchi, C. R. Wronski, and D. E. Carlson, *J. Appl. Phys.* 48, 5227 (1977).
27. *IR/90 Series FTIR Spectrometer User's Manual* (IBM Instruments Inc., Danbury, Connecticut, 1983).
28. M. H. Brodsky and A. Lurio, *Phys. Rev. B* 9, 1646 (1974).
29. H. R. Shanks, C. J. Fang, L. Ley, M. Cardona, F. T. Demond, and S. Kalbitzer, *Phys. Status Solidi (b)*100, 43 (1980).
30. G. A. N. Connel and R. A. Street, in *Handbook on Semiconductor*, edited by S. P. Keller (North-Holland Publishing, Amsterdam, 1980), Vol. 3.
31. P. Nagels, in *Topics in Applied Physics*, edited by M. H. Brodsky (Springer-Verlag, Berlin, 1979), Vol. 36.
32. N. F. Mott and E. A. Davis, *Electronic Processes in Non-Crystalline Materials*, Second ed. (Clarendon Press, Oxford, 1979).
33. S. M. Sze, *Physics of Semiconductor Devices*, Second ed. (John Wiley & Sons, New York, 1981).

34. G. Lucovsky, in *Fundamental Physics of Amorphous Semiconductors*, edited by F. Yonezawa (Springer-Verlag, Berlin, 1981), p. 87.
35. T. D. Moustakas, *Solar Energy Mater.* 8, 187 (1982).
36. F. R. Jeffrey, H. R. Shanks, and G. C. Danielson, *J. Appl. Phys.* 50, 7034 (1979).
37. J. Tauc, in *Amorphous and Liquids Semiconductors*, edited by J. Tauc (Plenum Press, London, 1974), p. 159.
38. E. A. Davis, in *Electronic and Structural Properties of Amorphous Semiconductors*, edited by P. G. Le Comber and J. Mort (Academic Press, New York, 1973), p. 425.
39. A. Matsuda, M. Matsumura, K. Nakagawa, T. Imura, H. Yamamoto, S. Yamasaki, H. Okushi, S. Iizima, and K. Tanaka, in *Tetrahedrally Bonded Amorphous Semiconductors*, edited by R. A. Street, D. K. Bregelsen, J. C. Knights (American Inst. Phys., New York, 1981) p. 192.
40. S. Zhao and S. Hunklinger, *Solar Energy Materials* 6, 233 (1982).
41. W. E. Spear and P. G. Le Comber, in *Photoconductivity and Related Phenomena*, edited by J. Mort and D. M. Pai (Elsevier Scientific Publishing, Amsterdam, 1976), p. 185.
42. T. D. Moustakas, D. A. Anderson, and W. Paul, *Solid State Commun.* 23, 155 (1977).
43. D. L. Staebler and C. R. Wronski, *J. Appl. Phys.* 51, 3262 (1980).
44. B. von Roedern, L. Ley, and M. Cardona, *Phys. Rev. Lett.* 39, 1576 (1977).
45. K. H. Johnson, H. J. Kolari, J. P. de Neufville, and D. L. More, *Phys. Rev. B* 29, 643 (1980).
46. D. A. Papaconstantopoulos, and E. N. Economou, *Phys. Rev. B* 24, 7233 (1981).
47. W. Paul and D. A. Anderson, *Solar Energy Materials*, 5, 229, (1981).
48. C. R. Wronski, D. E. Carlson, and R. E. Daniel, *Appl. Phys. Lett.* 29, 602 (1976).

49. A. Deneuveille and M. H. Brodsky, *J. Appl. Phys.* 50, 1414 (1979); *Thin Solid Films* 55, 137 (1978).
50. I. Chen and S. Lee, *J. Appl. Phys.* 53 1045 (1982).
51. M. J. Thomson, J. Allison, M. M. Al-Kaisi, and I. P. Thomas, *Revue de Physique Applique* 13, 625 (1978).
52. J. McGill and J. Wilson, *J. Appl. Phys.* 53, 1045 (1982).
53. C. C. Tsai, R. J. Nemanich, and M. J. Thompson, *J. Vac. Sci. Technol.* 21, 632 (1982).
54. M. H. Brodsky, F. Evangelisti, R. Fischer, R. W. Johnson, W. Reuter, and I. Solomon, *Solar Cells* 2, 401 (1980).
55. A. G. Revesz, *Thin Solid Films* 50, L29 (1978).
56. T. Tiedje, T. D. Moustakas, and J. M. Cebulka, *Phys. Rev. B* 23, 5634 (1981).
57. T. D. Moustakas, T. Tiedje, and W. A. Lanford, *A. I. P. Conference Procedures* #73, 20 (1981).
58. D. C. Allan and J. D. Joannopoulos, *Phys. Rev. Lett.* 44, 43 (1980).
59. P. Viktorovitch, G. Moddel, J. Blake, S. Oguz, R. L. Weisfield, and W. Paul, *Journal de Physique* 42, C4-455 (1981).
60. M. H. Cohen, J. Singh, and F. Yonezawa, *J. Non-Cryst. Solids* 35/36, 55 (1980).
61. S. Oguz, D. K. Paul, J. Blake, R. W. Collins, A. Lachter, B. G. Yacobi, and W. Paul, *Journal de Physique* 42, C4-679 (1981).
62. F. R. Jeffrey and M. E. Lowry, *J. Appl. Phys.* 52, 5529 (1981).

7. ACKNOWLEDGEMENTS

Praise the Lord God. "For the Lord gives wisdom; from His mouth comes knowledge and understanding" (Proverbs 2:6).

I would like to express my sincere gratitude to my advisor Professor D. K. Finnemore and my group leader Senior Physicist H. R. Shanks for their continued aid and guidance in this project. I would also like to thank Senior Research Technician O. M. Sevde for his technical assistance, Dr. A. J. Bevolo for performing the Auger analyses, and Mr. R. Esen for the photoconductivity measurements and helpful discussions. Thanks are also due to Mr. R. Dougherty for his valuable help in computer programming, and to Dr. B. Harmon for his help in my theoretical understanding of the problem.

I also want to express my utmost appreciation to my wife, Dian, to whom this thesis is dedicated. Through her patience and encouragement, she has contributed immeasurably to this work. The presence of my daughters, Melissa and Melinda, also provided me with much needed motivation.

Finally, the expert and timely typing services of Rebecca Shivers are gratefully acknowledged.

**8. APPENDIX: CALCULATION OF THE DENSITY OF STATES FROM
THE I-V CHARACTERISTICS OF SCHOTTKY DIODES**

In this appendix, the density of gap states from the Fermi energy E_F upward towards the conduction band will be derived using the I-V characteristics of the Schottky diode devices from the a-Si:H samples (see Ref. 19).

With all assumptions and Eqs. (25) to (31) mentioned in the text, one can use Eq. (26) in Eq. (28) and obtain

$$J = q \mu n_{CO} \epsilon(x) \exp. [u(x)] , \quad (A-1)$$

or

$$J = \sigma \epsilon(x) \exp. [u(x)] , \quad (A-2)$$

where $\sigma = q \mu n_{CO}$ is the thermal equilibrium conductivity, which is assumed to be a constant. Then differentiating Eq. (33) with respect to x ,

$$\frac{dJ}{dx} = \sigma \frac{d \epsilon(x)}{dx} \exp. [u(x)] + \sigma \epsilon(x) \exp. [u(x)] \frac{du}{dx}$$

since $dJ/dx = 0$, then

$$\frac{d\epsilon(x)}{dx} = - \frac{J}{\sigma} \exp. [-u(x)] \frac{du}{dx} . \quad (A-3)$$

Using Eq. (30):

$$\frac{\rho(x)}{\epsilon_s} = \frac{J}{\sigma} \exp. [-u(x)] \frac{du}{dx}$$

$$\frac{du}{dx} = \frac{\sigma}{\epsilon_s J} \exp. [u(x)] \rho(u) . \quad (\text{A-4})$$

Since u is a single value of x , one can write Eq. (A-4) as

$$dx = \frac{\epsilon_s J}{\sigma} \frac{\exp. [-u]}{\rho(u)} du$$

Integrating both sides with x from 0 to t , and u from ∞ to u_t ,

$$t = \frac{\epsilon_s J}{\sigma} \int_{u_t}^{\infty} \frac{\exp. [-u] du}{-\rho(u)} . \quad (\text{A-5})$$

This gives an implicit relation between the current density and the Fermi-level shift at the counter electrode.

Changing variables in Eq. (31) from x to u ,

$$V = - \int_0^t \epsilon(x) dx$$

$$V = - \int_{u_t}^{\infty} \epsilon(x) |j| du, \quad \text{where } |j| = \frac{1}{du/dx}$$

$$V = \int_{u_t}^{\infty} \frac{J}{\sigma} \exp. [-u] \cdot \frac{\epsilon_s J}{\sigma} \frac{\exp. [-u]}{-\rho(u)} du .$$

$$\text{Thus } V = \epsilon_s \frac{J^2}{\sigma^2} \int_{u_t}^{\infty} \frac{\exp. [-2u]}{-\rho(u)} du . \quad (\text{A-6})$$

Now differentiating Eqs. (A-5) and (A-6) w.r.t. u_t , one obtained the two derivatives:

$$0 = \frac{\epsilon_s}{\sigma} \frac{dJ}{du_t} \int_{u_t}^{\infty} \frac{\exp. [-u] du}{\rho(u)} + \frac{\epsilon_s J}{\sigma} \frac{\exp. [-u_t]}{\rho(u_t)}$$

or

$$0 = \frac{t}{J} \frac{dJ}{du_t} + \frac{\epsilon_s J}{\sigma} \frac{\exp. [-u_t]}{\rho(u_t)}$$

or

$$\frac{d \ln J}{d u_t} = \frac{\epsilon_s J}{\sigma t} \frac{\exp. [-u_t]}{\rho(u_t)}, \quad (\text{A-7})$$

and

$$\begin{aligned} \frac{dV}{du_t} &= \frac{2 \epsilon_s J}{\sigma^2} \frac{dJ}{du_t} \int_{u_t}^{\infty} \frac{\exp. (-2u)}{\rho(u)} du + \\ &\quad \frac{\epsilon_s J^2}{\sigma^2} \frac{\exp. (-2u_t)}{\rho(u_t)} \end{aligned}$$

or

$$\frac{dV}{du_t} = \frac{2V}{J} \frac{dJ}{du_t} + \frac{\epsilon_s J^2}{\sigma^2} \frac{\exp. [-2u_t]}{\rho(u_t)}$$

or

$$\frac{d \ln V}{d u_t} = 2 \frac{d \ln J}{d u_t} - \frac{\epsilon_s J^2}{\sigma^2 V} \frac{\exp. (-2 u_t)}{\rho(u_t)}. \quad (\text{A-8})$$

For convenience define:

$$a = \frac{d \ln V}{d \ln J} = \frac{J}{V} \frac{dV}{dJ},$$

$$b = \frac{d^2 \ln v}{d \ln J^2},$$

and

$$c = \frac{d^3 \ln v}{d \ln J^3},$$

and

$$J_{\Omega} = \frac{\sigma v}{t}.$$

Dividing Eq. (A-8) by (A-7), one obtain

$$a = \frac{(d \ln v / d u_t)}{(d \ln J / d u_t)}$$

$$a = 2 - \frac{Jt}{\sigma v} \exp. (-u_t) \quad (A-9)$$

$$a = 2 - \frac{J}{J_{\Omega}} \exp. (-u_t) \quad (A-10)$$

or

$$u_t = \ln \left[\frac{J}{J_{\Omega} (2-a)} \right]. \quad (A-11)$$

Differentiating Eq. (41) w.r.t. log. J,

$$\frac{d u_t}{d \ln J} = 1 - \frac{d \ln v}{d \ln J} - \left(\frac{1}{2-a} \right) \left(- \frac{d \ln a}{d \ln J} \right)$$

$$\frac{d u_t}{d \ln J} = 1 - a + \frac{b}{2-a} \quad (\text{A-12})$$

Inserting Eq. (A-12) in (A-7) ,

$$\frac{\epsilon_s J \exp. [-u_t]}{\sigma t - \rho(u_t)} = \frac{1}{(1 - a + \frac{b}{2-a})}$$

then the charge density at $x = t$ is

$$\rho_t = - \frac{\epsilon_s J}{\sigma t} (1 - a + \frac{b}{2-a}) \exp. [-u_t]$$

Use Eq. (40a) to substitute u_t ,

$$\rho_t = - \frac{\epsilon_s J}{\sigma t} (1 - a + \frac{b}{2-a}) \cdot (2-a) \cdot \frac{\sigma V}{J t}$$

or

$$\rho_t = - \frac{\epsilon_s V}{t^2} [(1-a)(2-a) + b] \quad (\text{A-13})$$

Differentiating Eq. (39) w.r.t. u_t ,

$$\frac{d \rho_t}{d u_t} = \left(\frac{d \rho_t}{d \ln J} \right) \left(\frac{d \ln J}{d u_t} \right)$$

$$= \left[- \frac{\epsilon_s}{t^2} \frac{dV}{d \ln J} \{ (1-a)(2-a) + b \} - \right.$$

$$\left. \frac{\epsilon_s V}{t^2} \{ -b(2-a) - b(1-a) + c \} \right] \cdot$$

$$\left[\frac{(2-a)}{(1-a)(2-a) + b} \right]$$

$$\frac{d \rho_t}{d u_t} = \left[- \frac{\epsilon_s V}{t^2} a \{ (1-a)(2-a) + b \} - \frac{\epsilon_s V}{t^2} \{ c - b(3-2a) \} \right]$$

$$\cdot \left[\frac{2-a}{(1-a)(2-a) + b} \right]$$

or

$$\frac{d \rho_t}{d u_t} = - \frac{\epsilon_s V}{t^2} \left[a(2-a) + \frac{c - b(3-2a)}{(1-a) + b/(2-a)} \right] \quad (A-14)$$

Assuming zero-temperature statistics, the gap state density is

$$N(E_{F0} + E) = - \frac{1}{q} \frac{d \rho (/kT)}{d E} .$$

So using Eqs. (A-11) and (A-14), one obtain for the gap state density

$$N(E_{F0} + \Delta E_F) = \frac{\epsilon_s V}{qkT t^2} \left[a(2-a) + \frac{c - b(3-2a)}{(1-a) + b/(2-a)} \right] \quad (A-15)$$

where

$$\Delta E_F = kT \ln \left[\frac{J}{J_\Omega (2-a)} \right] \quad (A-16)$$